Master Thesis

Probing Skyrmion Black Holes

Author:
Georgios Lioutas

Supervisor:
Prof. Dr Georgi Dvali

A thesis submitted in partial fulfillment of the requirements
for the degree of Master of Science

Ludwig-Maximilians-Universität München

Master thesis completed in the course of the program

TMP **Elite Master Course**
Theoretical and Mathematical Physics

---

carried out at the

Arnold Sommerfeld Center for Theoretical Physics

by

Georgios Lioutas

Acknowledgments

First I want to express my gratitude to my supervisor Prof. Georgi Dvali for his support and helpful advices. Being part of his group was invaluable, as it helped me better understand how research is done.

I am grateful to my two office mates. Alex for discussing various aspects of this project and sharing his knowledge on the topic and Jaba for all the nice discussions we had. Both of them made time spent in the office pleasant.

Thanks are also extended to all the friends I made during my years in Munich for making those last years so much nicer. Special thanks go to Pantelis, Alex and Vangelis for proofreading this thesis.

Last but not least, let me thank my family for their unconditional love and support and especially Eleftheria for being there for me, listening to my concerns and guiding me in ways that I never would have thought of.

Abstract

The Einstein-Skyrme system admits black hole solutions. These black holes with classical Skyrme hair were the first stable black hole solutions that could pose as counterexamples to the no-hair conjecture. We reproduce these solutions numerically, focusing on the static and spherically symmetric case. Then two different probes are used in order to further study them, photons and scalar fields. Initially we examine their photon spheres as a measure of how the near horizon geometry is affected due to the presence of the skyrmion hair. We find out that they remain practically unaffected. We then turn our attention towards gravitational lensing phenomena, so as to investigate if they could be used in order to distinguish between a Skyrme and a Schwarzschild black hole of the same ADM mass. As it turns out, they cannot be considered prominent for a physical scenario. Finally, we study classical scattering and absorption cross sections of a minimally coupled massless probe scalar field and compare our results with those obtained for a Schwarzschild black hole. We observe that the characteristic peaks in the differential scattering cross section are moved towards smaller angles, while in the absorption cross section towards higher frequencies. Both scattering and absorption are also investigated for a massive probe scalar field, where we discover that in a certain limit the skyrmion and Schwarzschild black holes are indistinguishable through scattering experiments.

Contents

List of Figures

List of Tables

Conventions and notation

Throughout this thesis we use units in which the speed of light c and the Boltzmann constant k_B are set to be equal to one

$$c = k_B = 1,$$

but at the same time both the Planck constant $\hbar$ and Newton's constant G_N retain their values. Furthermore, we adopt the signature $(+,-,-,-)$ for the metric. We should also note that in our tensor presentation, Greek indices $\alpha, \beta, ...$ run over $(0, 1, 2, 3)$, while Latin indices $i, j, ...$ run over $(1, 2, 3)$.

Chapter 1

Introduction

1.1 General description

In the 1980s and 1990s, it was found out that coupling (non-linear) matter models to gravity can lead to both black hole and particle-like solutions. Characteristic examples are the solutions that emerge from the Einstein-Yang-Mills and the Einstein-Skyrme system. What is rather interesting is that these black hole solutions asymptotically approach the pure gravity solutions of the same symmetry. Thus, they were the first counterexamples to the no-hair conjecture that black holes can be characterized by their mass, their electric charge and their angular momentum.

The question of stability of those solutions was automatically raised. Not all the solutions turned out to be stable, but those who did shared a particular property. The corresponding particle-like solutions were stable due to topological reasons. The particle-like solutions of the Einstein-Skyrme system, also called gravitating skyrmions, indeed exhibit such stability. Thus skyrmion black holes are rather interesting from a physical point of view, as one can very well expect to encounter them in nature.

At the same time, the Skyrme model can be considered as a low energy effective theory of QCD, whose topological Chern-Simons current can be mapped to the baryon number current of QCD. Namely, the winding number in the context of the Skyrme model can be mapped to the baryon number of QCD. Consequently, there is a correspondence between the skyrmion black holes and baryonic black holes. Thus the study of Skyrmion black holes can lead to interesting results regarding what happens to a baryon being swallowed by a black hole. It may well turn that the baryon number is conserved after all.

Based on this mapping it was recently found out [1] that the baryon charge can be written as a surface integral over a boundary surface enclosing the skyrmion. This can be taken to be a two-sphere at infinity. This shows that after all the skyrmion charge can be represented in the form of a boundary surface integral. In that sense, there is a way to distinguish a Schwarzschild black hole from a skyrmion black hole at infinity, which is solely based on topological considerations.

Other probes can also be used in order to distinguish between those two solutions. Especially interesting is to investigate how the hair manifests itself, as the conservation of baryon number could leave an imprint on how the black hole interacts with different probes. The typical candidate for a probe would be fields of different spins. Each one of them admits a different scattering and absorption behaviour from a black hole. As a

result, the way they are scattered and absorbed by skyrmion black holes and how this differs from the behaviour they exhibit in the presence of a Schwarzschild black hole can offer a great deal of information on the existence and nature of the hair. In our work we focus on those questions and try to provide an answer. At the same time, we look into photons and how they behave around skyrmion black holes as well. Let us highlight that we only take gravitational interactions into account.

Note that the hair discussed in this work are different from the quantum baryonic hair suggested in [2]. These ideas are consistent with each other and they could very well turn out to be complementary.

Finally, let us comment that the study of skyrmion black holes is expected to have astrophysical consequences. In an astrophysical scenario a large number of baryons will have been swallowed by the black hole. Yet, in the absence of skyrme black hole solutions for arbitrarily large winding numbers, one is confined to tackle this problem at the small winding number level.

1.2 Outline

Chapter 2 is an introduction to the Skyrme model, its coupling to General Relativity and a discussion on the solution space. In Chapter 3 we focus on photons as probes. Results on how photon spheres are altered due to the presence of the skyrme hair and gravitational lensing phenomena as means of distinguishing skyrmion from Schwarzschild black holes are discussed there. In Chapter 4 we switch to another probe, a minimally coupled scalar field, in order to see how the hair manifests itself. We compute classical differential scattering cross sections and absorption cross sections for a massless and a massive scalar field scattered by a Skyrmion black hole. All results are compared to the respective results obtained for a Schwarzschild black hole of the same ADM mass. The conclusions of our work can be found in Chapter 5. Finally, we devote Appendix A to a proof of the existence of photon spheres in static and spherically symmetric spacetimes.

Chapter 2

Skyrmion Black Holes

In this chapter we present the Skyrme model, which we then couple to Einstein gravity to obtain hairy black hole solutions. We give an exposition of the methodology used to obtain these solutions, as well as describe their main characteristics. A short review of no-hair theorems can also be found here. This is a mere discussion of results that have been obtained during the past decades, where appropriate references are provided in place.

2.1 The Skyrme model

The Skyrme model was proposed by T.H.R. Skyrme [3, 4] as an effective theory of baryons. Its importance is closely related to Quantum Chromodynamics (QCD), the $SU(3)$ gauge theory describing the strong interaction. In order to solve QCD an approximation method is needed. However, the perturbative approach, which proved to be very convenient in the case of Quantum Electrodynamics (QED), is inefficient. The underlying reason for that is that the coupling constant is large at low energy scales. Consequently, it cannot be used as an expansion parameter. This has led people to pursue some effective theory to study the low energy processes of QCD and the Skyrme model can serve as such.

An extensive review of the model can be found in [5].

2.1.1 Lagrangian and stability of static configurations

The Skyrme model is a non-linear meson theory, which proved to be a powerful effective theory of pions in the low energy scale of QCD. The Skyrme Lagrangian reads

$$\mathcal{L}_{\mathcal{S}} = \mathcal{L}_2 + \mathcal{L}_4 + \mathcal{L}_m, \tag{2.1}$$

where

$$\mathcal{L}_2 = \frac{F_\pi^2}{4}\,\mathrm{Tr}(\partial_\mu U \partial^\mu U^\dagger), \tag{2.2}$$

$$\mathcal{L}_4 = \frac{1}{32e^2}\,\mathrm{Tr}\left(\left[U^\dagger\partial_\mu U, U^\dagger \partial_\nu U\right]^2\right), \tag{2.3}$$

$$\mathcal{L}_m = \frac{1}{2}\frac{m_\pi^2}{\hbar^2} F_\pi^2\,\mathrm{Tr}(U-2). \tag{2.4}$$

Here F_π can be interpreted as the pion decay constant, e is a parameter indicative of the magnitude of solitons of the system, m_π is the pion mass and $U \in SU(2)$.

The $\mathcal{L}_2$ term is a non-linear sigma model kinetic term and forms the basis of the model. However, such a term leads to an energy

$$E = \frac{F_\pi^2}{4} \int d^3x \ \mathrm{Tr}(\partial_i U \partial^i U^\dagger) \tag{2.5}$$

for a static configuration. A simple rescaling (e.g. [6, 7]) can however reveal that such configurations are not energetically stable according to Derrick's theorem [8]. Physically, this tests whether the solutions are stable under a uniform stretch. Specifically, let us rescale the space coordinate as

$$U(\mathbf{x}) \to U(\lambda \mathbf{x}) \tag{2.6}$$

and at the same time take the dimension of space to be arbitrary and equal to D. Then, the energy of the static configuration reads

$$\begin{aligned} E(\lambda) &= \frac{F_\pi^2}{4} \int d^D x \ \mathrm{Tr}\left(\partial_i U(\lambda \mathbf{x}) \partial^i U^\dagger(\lambda \mathbf{x})\right) \\ &= \frac{F_\pi^2}{4} \int d^D(\lambda x) \lambda^{2-D} \ \mathrm{Tr}\left(\eta^{ij} \partial_i^\lambda U(\lambda \mathbf{x}) \partial_j^\lambda U^\dagger(\lambda \mathbf{x})\right) \\ &= \lambda^{2-D} E, \end{aligned} \tag{2.7}$$

where $\partial_i^\lambda = \partial / \partial(\lambda x^i)$.

In our case, namely $D = 3$, it is evident that

$$E(\lambda) = \frac{1}{\lambda} E, \tag{2.8}$$

which shows that as we increase the space scale, the energy of the static configuration decreases. We can thus draw the conclusion that in the $D = 3$ case the configuration $U(\mathbf{x})$ is not stable.

The introduction of the $\mathcal{L}_4$ term solves the problem and allows for solitonic configurations, which from now on will be referred to as Skyrmions. Specifically, the new static energy reads

$$\begin{aligned} E^{\mathrm{Skyr}} &= E^{\mathrm{Skyr},\mathcal{L}_2} + E^{\mathrm{Skyr},\mathcal{L}_4} \\ &= -\int d^3x \ \mathrm{Tr}\left(\frac{F_\pi^2}{4} L_i L^i + \frac{1}{32e^2}[L_i, L_j]^2\right) \\ &= -\int d^3x \ \mathrm{Tr}\left(\frac{F_\pi^2}{4} L_i L^i + \frac{1}{16e^2}(\epsilon_{ijk} L_i L_j)^2\right) \\ &= \frac{F_\pi^2}{4} \int d^3x \ \mathrm{Tr}\left(L_i L_i^\dagger + \frac{1}{4e^2 F_\pi^2}(\epsilon_{ijk} L_i L_j)(\epsilon_{ijk} L_i^\dagger L_j^\dagger)\right) \\ &\geq \frac{F_\pi^2}{4} \int d^3x \ \left|\mathrm{Tr}\left(\frac{1}{eF_\pi} \epsilon_{ijk} L_i L_j L_k\right)\right| \\ &\geq 0, \end{aligned} \tag{2.9}$$

proving that the static energy is positive and bounded from below. Here we introduced the notation $L_\mu = U^\dagger \partial_\mu U$, while at the penultimate line we made use of the Cauchy-Schwartz inequality.

Let us now apply the same space rescaling as before in order to verify that in $D = 3$ the soliton is stable. By following the exact same steps we get

$$E^{\text{Skyr}}(\lambda) = \lambda^{2-D} E^{\text{Skyr},\mathcal{L}_2} + \lambda^{4-D} E^{\text{Skyr},\mathcal{L}_4}. \tag{2.10}$$

We wish to check stability against space rescaling so we are after the extrema. It is straightforward to obtain

$$\left.\frac{dE^{\text{Skyr}}(\lambda)}{d\lambda}\right|_{\lambda=1,D=3} = -E^{\text{Skyr},\mathcal{L}_2} + E^{\text{Skyr},\mathcal{L}_4}, \tag{2.11}$$

$$\left.\frac{d^2E^{\text{Skyr}}(\lambda)}{d\lambda^2}\right|_{\lambda=1,D=3} = 2E^{\text{Skyr},\mathcal{L}_2}. \tag{2.12}$$

At the extremum we thus get $E^{\text{Skyr},\mathcal{L}_2} = E^{\text{Skyr},\mathcal{L}_4} = E^{\text{Skyr}}/2 \geq 0$. Taking this result into account we obtain

$$\left.\frac{d^2E^{\text{Skyr}}(\lambda)}{d\lambda^2}\right|_{\lambda=1,D=3} \geq 0, \tag{2.13}$$

which shows that the extremum is a minimum, consequently proving that the static configuration is indeed stable against space scaling.

The addition of the $\mathcal{L}_4$ term does stabilize the static energy as promised. One can now find stable solutions to the equations of motion of our non-linear model. It is precisely those stabilized solutions which are referred to as Skyrme solitons or skyrmions.

Furthermore, let us note that the Lagrangian is chiral before the introduction of the $\mathcal{L}_m$ term. This is easy to check as both terms are invariant under chiral transformation, since U transforms as

$$U(\mathbf{x}) \to g_L U(\mathbf{x}) g_R^\dagger, \tag{2.14}$$

where $g_L \in SU(N)_L$ and $g_R \in SU(N)_R$ respectively.

In order to account for the small, yet non-vanishing, mass of the pion field, one has to add an explicit chiral breaking term in the form of $\mathcal{L}_\pi$.

Finally, we should add that the values of the parameters F_π, e, m_π of the model can be fixed through experiment. To be precise, one of the parameters should be fixed by hand, while the other two are then fixed by fitting to the experimental data. Such a work can be found in [9][1].

2.1.2 Topological properties

Let us now take a step back and have a better look at the formulation of our model and the consequences of topological nature that it bears. At any fixed time, the unitary matrix U defines a map from $\mathbb{R}^3$ to the manifold $SU(2) \cong S^3$. Furthermore, the requirement for the energy to be finite leads to the boundary condition

$$U^\dagger \partial_i U \to 0 \quad \text{as} \quad |\mathbf{x}| \to \infty, \tag{2.15}$$

[1]Note that one should first look at the action as the parameters may differ by some multiplicative factor in different works.

which means that U approaches some constant matrix at infinity. Without loss of generality, this matrix can be taken to be the identity matrix

$$U(|\mathbf{x}| \to \infty) = \mathbb{I}. \tag{2.16}$$

An immediate consequence of this is that the 3-dimensional space is compactified into the 3-sphere S^3. As a result, we have the nontrivial set of maps

$$U(\mathbf{x}) : S^3 \to S^3, \tag{2.17}$$

which are topologically classified by the third homotopy group $\pi_3(S^3) = \mathbb{Z}$. At the same time, allowing for a change in the time coordinate can be seen as a homotopy and thus it cannot move the field configuration between homotopically distinct classes. As a result, the field configurations are classified by the integer number of times that S^3 is covered by $U(\mathbf{x})$, also called the winding number.

The winding number B can be obtained as the integral over the topological charge, namely

$$B = \int d^3x \; J_0, \tag{2.18}$$

where the corresponding topological current is given by

$$J_\mu = -\frac{\epsilon_{\mu\nu\alpha\beta}}{24\pi^2} \operatorname{Tr}(U^{-1}\partial^\nu U U^{-1}\partial^\alpha U U^{-1}\partial^\beta U). \tag{2.19}$$

Note that with respect to B, the lower bound to the static energy as computed for $\mathcal{L} = \mathcal{L}_2 + \mathcal{L}_4$ can be expressed as

$$E^{\text{Skyr}} \geq 6\pi^2 \frac{F_\pi}{e} |B|, \tag{2.20}$$

which is the Bogomol'nyi bound. The inequality is saturated for a self-dual field, namely

$$L_i = \frac{1}{2eF_\pi} \epsilon_{ijk} L_j L_k. \tag{2.21}$$

It can be shown that the soliton solutions do not attain the lower bound of the energy[2], consequently they are not BPS states.

As the Skyrme model is non-linear, it also leads to highly non-linear equations of motion. In order to solve them, Skyrme proposed the use of a hedgehog ansatz

$$U = e^{iF(r) n_\alpha \sigma_\alpha} = \cos F(r)\, \mathbb{I} + i n_\alpha \sigma_\alpha \sin F(r), \tag{2.22}$$

where n_α is the unit vector along the radial direction and σ_α the Pauli matrices.

Boundary conditions should also be obtained for $F(r)$. They can be found through the following considerations:

- The origin of the 3-dimensional space must be mapped to a single point in S^3. Thus, one has to require that $F(0) = B_0\pi$.

[2] One way to see this is that the self-dual soliton does not satisfy the Maurer-Cartan equations.

- The total energy of the system should be finite. We have seen that this is equivalent to requiring $U(\mathbf{x})$ to approach a real constant matrix as $|\mathbf{x}| \to \infty$. As a result, we should impose $F(\infty) = B_\infty \pi$, where $B_\infty \in \mathbb{Z}$.

Since the classification is based on the winding number B, only the difference $B_0 - B_\infty$ matters, as a result one is free to set

$$F(0) = B\pi, \; F(\infty) = 0. \tag{2.23}$$

Of course, the choice of B is directly related to the symmetry of the skyrmion. This symmetry is present in the gravitating model as well.

2.2 Coupling to Einstein gravity

In this work we are interested in solutions of the Skyrme model in the presence of gravity. The Einstein-Skyrme model, along with a number of other models such as e.g. the Einstein-Yang-Mills and the Einstein-Yang-Mills-Higgs models, allows for two types of solutions. The first one is particle-like solutions [10, 11, 12, 13, 14, 15, 16] and the latter black holes (BHs) [17, 18, 19, 20, 21, 22, 23]. Both solutions are of high importance and interest.

In the case of particle-like solutions their existence came as a surprise when first discovered in the case of the Einstein-Yang-Mills model, since neither the Einstein equations nor the Yang-Mills equations have non-trivial static globally regular solutions. As it seems, the attractive nature of gravity and the repulsive nature of the Yang-Mills field are such that they can cancel each other out. Subsequently, the gravitating solitons emerging as solutions to these models, have drawn attention on to them. Their existence, classification and relation to the flat spacetime solitons of the corresponding models were the first questions to be asked about them.

On the other hand, we have BH solutions. What's most important about those solutions is that they are hairy, namely they contradict the no-hair conjecture formulated for BHs. This is rather interesting for quite a few reasons. First of all, questions arise from the existence of hair, as to what kind of information we can obtain about the matter that the BH has swallowed. Also, the spacetime is altered by the presence of hair. It would be rather interesting to find out what kind of observational traces this leaves, especially now that we have scratched the surface of the field of direct BH observation [24]. Many more questions can be asked, but we will mainly worry ourselves about the second one.

2.2.1 No-hair Theorems

The no-hair theorem is actually a conjecture on which parameters of the black hole can be measured by an observer lying on the exterior of a black hole. The initial belief was that all black holes can be characterized by their mass, electric charge and angular momentum. Namely, that those are the only measurable parameters by an external observer, while all other information about matter which lies inside the horizon of the black hole is lost. Currently, this result has been reduced to stationary black hole solutions of the Einstein-Maxwell theory and some types of non-Maxwellian matter. A historical review of how the initial conjecture was proposed, how it evolved and the extent to which it is proven

can be found in [25] by W. Israel or in many other works such as [26, 27, 28]. The first use of the term "hair" can be found in [29].

Let us give a brief exposition of the building blocks of the theorem in the Einstein-Maxwell case. At the very heart of the theorem lies the uniqueness theorem (see e.g. [30]) for the asymptotically flat, stationary black hole solutions of the Einstein-Maxwell equations. Essentially, this is a classification of the solutions into families. Then, by looking at the parameters characterizing those families, one can conclude the no-hair theorem. The uniqueness theorem is a mix of the following results:

1. S. Hawking showed in [31, 32] that a stationary black hole must have a horizon which admits spherical topology. Furthermore, such a black hole can either be static or axisymmetric.

2. In the case of static black holes W. Israel [33, 34] established that any static black hole with event horizon of spherical topology can be uniquely characterized by its mass and electric charge. Furthermore, he identified these static vacuum and electrovac[3] black holes with the Schwarzschild and the Reissner-Nordstrom solutions respectively. [4]

3. The result for stationary and axisymmetric black holes is based on the Ernst formulation of the Einstein(-Maxwell) equations [36]. Based on this formulation, Carter [37, 38] showed that all uncharged, stationary and axisymmetric black holes with event horizon of spherical topology fall into disjoint families, which are not deformable to each other. Those are characterized by their mass and angular momentum, the Kerr family being the prime example. In the case of vacuum solutions it was Robinson [39] that proved that solutions with the same boundary and regularity conditions are identical, thus restricting all possible solutions to the Kerr family. The extension of the above to the electrovac case was carried out at some later point independently by Mazur [40, 41] and Bunting [42].

Combining all the above we get that the most general stationary solution that one can obtain in the context of the Einstein or Einstein-Maxwell theory is the Kerr-Newman solution, characterized by its mass M, electric charge Q and angular momentum S. The obvious sub-families of this solution are the Schwarzschild solution ($Q = 0, S = 0$), the Kerr solution ($Q = 0, S \neq 0$) and the Reissner-Nordstrom solution ($Q \neq 0, S = 0$).

Furthermore, let us note that the following point of view can also be adopted. Let us refer to conserved charges associated with a massless gauge field as global charges. One then notices that mass, angular momentum and electric/magnetic charges are such global charges. Thus, one could state that electrovac solutions are described by global charges. This statement cannot be generalised to all theories[5]. However, it stresses out the connection of the observable quantities to Gauss law.

We should also note that other cases, involving non-Maxwellian matter, in which the no-hair theorem can be extended have been studied [43, 44, 45, 46, 47, 48].

[3] The term refers to vacuum solutions of the Einstein-Maxwell theory.
[4] Note that another proof has been found by Bunting and Masood-ul-Alam [35].
[5] The Einstein-Yang-Mills theory is a counterexample.

Again, let us remind the reader that the no-hair theorem is a theorem under certain assumptions only, e.g. in the context of Einstein-Maxwell theory. It is the conjecture that the theorem can be generalized to all cases that the Skyrmion black holes invalidate.

2.2.2 Einstein-Skyrme model

The Einstein-Skyrme model is defined by the action

$$\mathcal{S} = \int d^4x \sqrt{-g} \left(-\frac{1}{16\pi G} R + \mathcal{L}_{\mathcal{S}} \right), \tag{2.24}$$

where R is the Ricci scalar and g the determinant of the metric tensor $g_{\mu\nu}$.

Varying the action (2.24) with respect to the metric tensor $g^{\mu\nu}$, one gets the Einstein field equations

$$G_{\mu\nu} \equiv R_{\mu\nu} - \frac{1}{2} g_{\mu\nu} R = 8\pi G T^S_{\mu\nu}, \tag{2.25}$$

where $G_{\mu\nu}$ the Einstein tensor, $R_{\mu\nu}, R$ the Ricci tensor and scalar respectively and the energy momentum tensor $T^S_{\mu\nu}$ is present because of the Skyrme Lagrangian and can be computed as

$$T^S_{\mu\nu} = \frac{2}{\sqrt{-g}} \frac{\delta(\sqrt{-g}\mathcal{L}_{\mathcal{S}})}{\delta g^{\mu\nu}}. \tag{2.26}$$

This is precisely the way the Skyrme Lagrangian is coupled to gravity.

In order to obtain the differential equations describing the system, we have to use an ansatz for the metric. In our case, we are interested in static, spherically symmetric solutions, thus we use

$$ds^2 = N^2(r) \left(1 - \frac{2GM(r)}{r} \right) dt^2 - \left(1 - \frac{2GM(r)}{r} \right)^{-1} dr^2 - r^2 d\Omega^2, \tag{2.27}$$

where $d\Omega^2 = d\theta^2 + \sin^2 d\theta d\phi^2$ the standard metric on the 2-sphere.

At the same time, we need an ansatz for the Skyrme field. The hedgehog ansatz described in Eq. (2.22) shall serve as such.

One can now make the following observation. The system contains three unknown functions, namely $N(r), M(r)$ and $F(r)$. Solving for them would enable us to describe the solutions up to the full extent. For this purpose, we wish to find the differential equations involving them. Those shall be the temporal and radial field equations and the equation of motion of the Skyrme field.

The Skyrme Lagrangian contains two parameters, F_π and e whose dimensionality is

$$[F_\pi] = \sqrt{\frac{[\text{Mass}]}{[\text{Length}]}}, \tag{2.28}$$

$$[e] = \frac{1}{\sqrt{[\text{Mass}][\text{Length}]}}, \tag{2.29}$$

in the $c = 1, k_B = 1$ system of units.

They can be used to define better suited variables for our case. From now on, radial dependence will be expressed in terms of $x = eF_\pi r$ and the mass function will be $m(x) = eF_\pi GM(r)$. Furthermore, we introduce the notation

$$h(x) = 1 - \frac{2m(x)}{x}, \tag{2.30}$$

in order for the differential equations to have a simple form. Additionally, this function will be crucial in the classification of the solutions as gravitating skyrmions or skyrmion BHs.

In the same spirit, we introduce two dimensionless parameters

$$\alpha = 4\pi G F_\pi^2, \tag{2.31}$$

$$\beta = \frac{m_\pi}{e\hbar F_\pi}, \tag{2.32}$$

which will prove useful in characterizing the solutions. Specifically, they will be used to label the solutions, as, alongside the event horizon radius, they uniquely characterize all BH solutions. Note that α is the coupling constant between the two models, while β is proportional to the pion mass. Thus they are both indicative of the magnitude of the mass that can be attributed to (self-)interactions and the pion itself.

Keeping this notation in mind and plugging the ansatzes for the metric and the skyrmion field into the Skyrme Lagrangian, its terms obtain the following form

$$\mathcal{L}_2 = -\frac{e^2 F_\pi^4 \left(2\sin^2 F(x) + x(x-2m(x))(\partial_x F(x))^2\right)}{2x^2}, \tag{2.33}$$

$$\mathcal{L}_4 = -\frac{e^2 F_\pi^4 \sin^2 F(x) \left(\sin^2 F(x) + 2x(x-2m(x))(\partial_x F(x))^2\right)}{2x^4}, \tag{2.34}$$

$$\mathcal{L}_m = \frac{1}{2}\beta^2 e^2 F_\pi^4 \left(2\cos F(x) - 2\right). \tag{2.35}$$

By varying the action (2.24) with respect to $F(r)$ we obtain the equation of motion for the Skyrme field $F(x)$, which reads

$$\begin{aligned} &\partial_x \left((x^2 + \sin^2 F(x)) N(x) h(x) \partial_x F(x)\right) \\ &\quad = N(x) \left\{ \sin 2F(x) \left(1 + h(x)(\partial_x F(x))^2 + \frac{\sin^2 F(x)}{x^2}\right) + \beta^2 x^2 \sin F(x) \right\}. \end{aligned} \tag{2.36}$$

At the same time, the temporal and radial component of the field equations (2.25) read

$$\begin{aligned} \partial_x m(x) = \alpha \Bigg\{ &\frac{x^2}{2} h(x)(\partial_x F(x))^2 + \sin^2 F(x) \\ &+ \sin^2 F(x) \left(h(x)(\partial_x F(x))^2 + \frac{\sin^2 F(x)}{2x^2}\right) - \frac{1}{2}\beta^2 x^2 (2\cos F(x) - 2) \Bigg\}, \end{aligned} \tag{2.37}$$

$$\partial_x N(x) = \alpha \left(x + \frac{2}{x}\sin^2 F(x)\right) N(x)(\partial_x F(x))^2, \tag{2.38}$$

respectively.

The boundary conditions used for solving these differential equations are

$$N(\infty) = 1, \tag{2.39a}$$
$$F(\infty) = 0, \tag{2.39b}$$

where the first one follows from the demand that the spacetime is asymptotically Minkowksi, while the second one we discussed when presenting the Skyrme model. In order for the system to be solved two more boundary conditions are required. More details on the matter will be given in the following subsection.

2.2.3 Numerical approach

The problem of finding solutions to the Einstein-Skyrme model, as discussed in the previous subsection is numerical. Skyrmion black hole solutions, alongside their stability and the parameter space of the solutions were discussed in [7, 10, 17, 18, 49]. In these cases, no mass term for the skyrmion was present. Furthermore, most of them employ a slightly different notation, which makes direct comparison of the equations somehow difficult. In [50] they accounted for the mass term as well. We adopt their notation.

We are interested in spherically symmetric and static BHs. The symmetry of the BH is directly related to the symmetry of the corresponding flat skyrmion. Namely, since we are looking for spherically symmetric BHs, the underlying flat space skyrmion should also be spherically symmetric. Such a condition is related to the winding number B. Specifically, we are interested in $B = 1$ skyrmion BHs for the aforementioned reason.

In order to obtain solutions, differential equations (2.36)-(2.38) should be numerically integrated, using (2.39) as boundary conditions. However, we are dealing with two complications now. First of all, we are missing two boundary conditions in order to solve the aforementioned system of differential equations. Secondly, our system is not in the form of an initial value problem, but rather in the form of a boundary value problem. The solution to both problems comes by employing the shooting method. In order however for the shooting method to be applied we need information on the derivative of the function in order to avoid guessing.

To obtain the required information about the derivative, one can expand the fields $F(x), m(x)$ and $N(x)$ around the event horizon x_h up to first order. Taking into account that the mass at the horizon should be that of a Schwarzschild BH we obtain

$$F(x) = F_h + F_1\,(x - x_h) + O((x - x_h)^2), \tag{2.40}$$
$$m(x) = \frac{x_h}{2} + m_1\,(x - x_h) + O((x - x_h)^2), \tag{2.41}$$
$$N(x) = N_h + N_1\,(x - x_h) + O((x - x_h)^2), \tag{2.42}$$

where $F_h = F(x_h), N_h = N(x_h)$ and F_1, m_1, N_1 are parameters to be computed.

Plugging the expansion back into the system of differential equations (2.36)-(2.38), we

obtain the following values for the parameters under investigation

$$F_1 = \frac{\sin 2F_h\,(x_h^2 + \sin^2 F_h) + \beta^2 x_h^4 \sin F_h}{x_h(x_h^2 + 2\sin^2 F_h)(1-2m_1)}, \tag{2.43}$$

$$m_1 = \alpha\left(\sin^2 F_h + \frac{\sin^4 F_h}{2x_h^2} - \beta^2 x_h^2(\cos F_h - 1)\right), \tag{2.44}$$

$$N_1 = \alpha\left(x_h + \frac{2\sin^2 F_h}{x_h}\right) N_h F_1^2. \tag{2.45}$$

The expansions depend on F_h, x_h and N_h. Out of them, F_h and N_h are used as shooting parameters, determined so as to satisfy the boundary conditions (2.39). Of course, for different values of x_h, different values for F_h and N_h have to be picked.[6]

If we were after particle-like solutions, we would have expanded around $x = 0$. In that case, different kind of information would be available. For example, we know that $F(0) = B\pi$. In the case of $B = 1$, which is the one under investigation here, we get $F(0) = \pi$. This indicates that we should expect to find $0 < F_h < \pi$ in our case. Actually, it turns out that solutions can be found when $\pi/2 < F_h < \pi$ [10].

An argument about the topological classification of our solutions is also in place here. We have seen that the flat spacetime skyrmions are subjected to a topological classification due to the fact that $\pi_3(S^3) = \mathbb{Z}$. The same classification can be applied in the case of gravitating skyrmions as well. However, when dealing with BHs the picture is different. In the BH case, we do not have a mapping from $\mathbb{R}^3$ to the manifold S^3 any more, as the ball $B_{x_h}(0)$ is removed from $\mathbb{R}^3$. The condition $F(\infty) = 0$ still holds though, so we have a mapping

$$U(x) : S^3 \setminus B_{x_h}(0) \to S^3. \tag{2.46}$$

However, the first space is now contractible and thus the aforementioned mapping is topologically trivial. If one attempted to glue the hole in S^3 by imposing some physically relevant condition, he would soon find out that then $F(x) = 0 \quad \forall x$, which strips the BH of its hair and simply leads back to the Schwarzschild solution. Therefore all BH solutions of the Einstein-Skyrme model are topologically trivial.

2.2.4 Solution space

As we have stated already, the Einstein-Skyrme model admits two types of solutions, gravitating skyrmions and skyrmion BHs. They are distinguished by the existence of a regular event horizon. This translates to the existence of a value x_h such that

$$h(x_h) = 0, \quad h(x) > 0 \quad \forall x > x_h. \tag{2.47}$$

[6] As a different approach, one could also note that the boundary conditions are to be implemented at infinity. As a numerical workaround, we could set up a new radial variable s as

$$s = \frac{x - x_h}{x + x_h}.$$

Then, $s = 0$ at $x = x_h$ and $s = 1$ when $x \to \infty$. With respect to this new variable, boundary conditions at infinity can be implemented. Of course integration would be performed backwards all the way to $s = 0$, where the horizon lies. It would be interesting to check whether the problem is simplified in this way. Of course, our differential equations should be reformulated in the language of the new variable.

Obviously, the existence of such a horizon indicates that the solution is a BH, while its absence leads to the conclusion that we are dealing with a skyrmion.

First of all, let us provide a physical picture of the skyrmion BH solutions. As stated, such solutions are identified by the existence of a regular event horizon. What is crucial in this case is that the horizon is smaller that the characteristic length scale of the skyrmion L. Namely, the BH lies inside of the skyrmion, but has not managed to swallow it, as the skyrmion is larger. The part of the skyrmion which has not been swallowed constitutes the hair in the sense that it alters the spacetime surrounding the black hole with respect to the corresponding Schwarzschild BH of the same ADM mass.

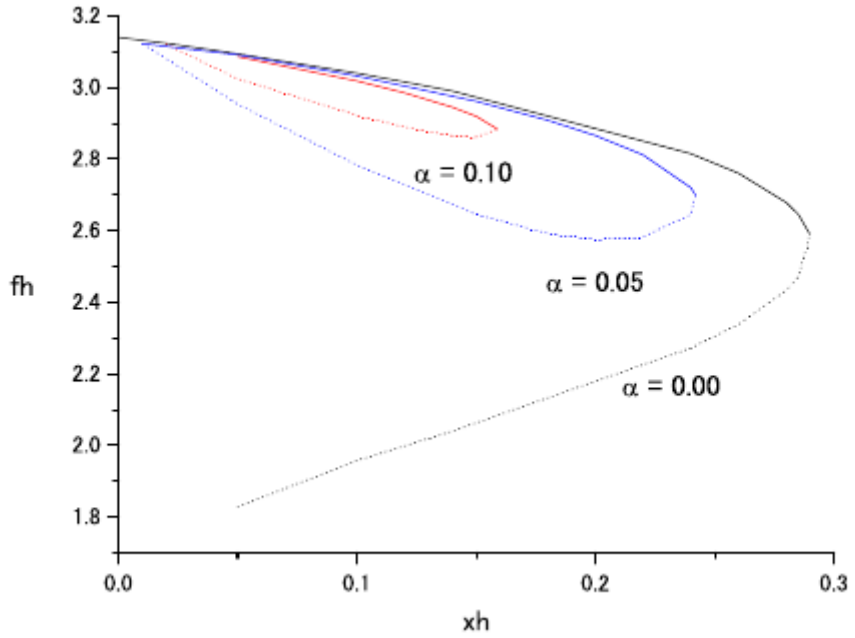

Figure 2.1: F_h vs x_h diagram for $\alpha = 0, 0.05, 0.1$ and $\beta = 0$. Solid lines are used for the upper stable branch, while dotted lines for the lower unstable branch. It is evident that for given (α, β, x_h) one can find two different solutions. At the same time, there exists a maximum value of x_h, different for each combination of (α, β), beyond which there are no solutions. The figure is adopted from [7].

Both solution families, gravitating skyrmions and skyrmion BHs, are characterized by the value of the horizon x_h and the two parameters α and β introduced in (2.31),(2.32). In other words, after choosing the values of those three parameters [7], one can find solutions only for certain values of F_h and N_h. In the case of gravitating skyrmions, a unique solution can be found. On the contrary, there is a degeneracy in the case of skyrmion BHs as one can find two different solutions for the same combination of (α, β, x_h). The two solutions differ in the value of F_h. Consequently, one obtains two separate branches of solutions in a diagram F_h vs x_h as seen in Figure 2.1.

There are some major physical differences between these two branches. First of all, one

[7] Those three parameters cannot be picked arbitrarily, as solutions exist only for a certain range of their values as described in the following paragraphs.

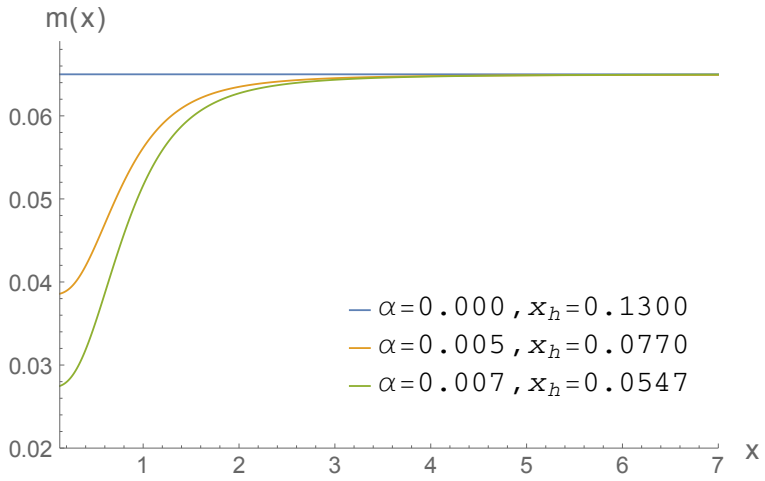

Figure 2.2: $m(x)$ vs x diagram for $\beta = 0$ and α, x_h as they appear in the legend. All three models have $m_{ADM} = 0.065$, thus proving that mass does not single-handedly characterize a static and spherically symmetric Skyrmion black hole solution.

should examine what happens at the limits $x_h \to 0$ and $\alpha \to 0$. One can see that all BH solutions converge to globally regular solutions for $a \neq 0$ as $x_h \to 0$. On the other hand, as $\alpha \to 0$[8] solutions of the upper branch go continuously to the Schwarzschild solutions with chiral hair as seen in Figures 2.2 and 2.3, while solutions of the lower branch converge to the $n = 1$ colored black hole solution [21].

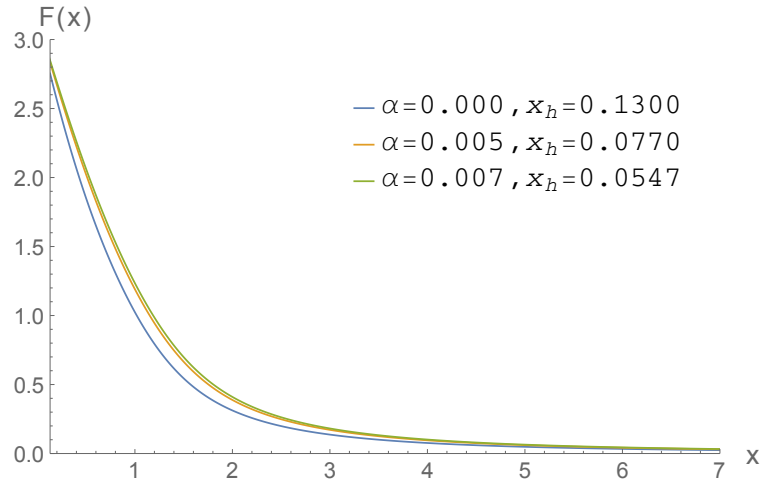

Figure 2.3: $F(x)$ vs x diagram for $\beta = 0$ and α, x_h as they appear in the legend.

At the same time, the issue of stability arises [7, 10, 49]. In order to examine stability at the linear level, one has to consider the time-dependent Skyrme action. Then, the time-dependent versions of Eq. (2.36)-(2.38) have to be produced. Small radial fluctuations around the static classical solutions are considered for both branches. One then

[8]This can be interpreted as the decoupling limit $G \to 0$ or, due to the other interpretation of α in (2.50), as the limit $N_C \to 0$.

looks for negative modes in the spectrum. No negative modes are present for the upper branch solution, thus making them stable against spherically symmetric time-dependent perturbations. At the same time, the same does not hold for the lower branch solutions where a negative mode is present in the spectrum rendering them unstable against such perturbations. All solutions that will be reproduced and investigated in the context of this work belong to the upper branch, thus represent plausible physical configurations.

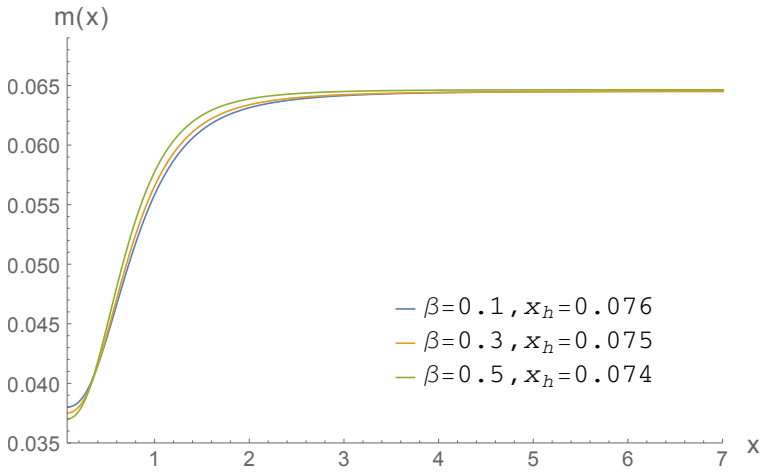

Figure 2.4: $m(x)$ vs x diagram for $\alpha = 0.005$ and β, x_h as they appear in the legend. All three models have $m_{ADM} = 0.065$, aligning with the fact that mass does not single-handedly characterize a static and spherically symmetric Skyrmion black hole solution and showing that β induces more freedom in finding solutions.

We have stated that for a given combination of (α, β, x_h) one can find two black hole solutions. However, there exist solutions only for a specific range of those parameters. Let us elaborate a bit on those ranges and interpret them inside a more physical framework along the lines of [50].

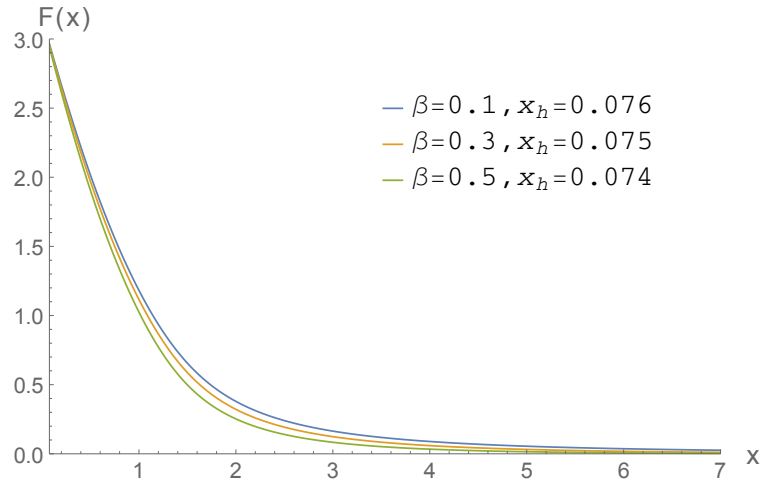

Figure 2.5: $F(x)$ vs x diagram for $\alpha = 0.005$ and β, x_h as they appear in the legend.

We have three different length scales involved in the system. Those are the characteristic length scale of the skyrmion L, the gravitational radius of the skyrmion $L_g \sim 2GM_S$ and the Compton wavelength of a single skyrmion L_C. If one takes a better look at the definition of α and β it becomes evident that they are related to the aforementioned length scales as

$$\alpha \sim \frac{L_g}{L}, \tag{2.48}$$

$$\beta = \frac{L}{L_C}. \tag{2.49}$$

At the same time

$$\alpha \sim N_C \tag{2.50}$$

as evidenced by Witten [51], where N_C is the number of colors. Note that neither L, nor L_C scale with N_C, so β is independent of N_C. Thus, for starters, we fix the value of β and investigate the parameter space of solutions. The following become more evident through Figures 2.1 - 2.3.

When investigating the solution space, one finds out that there exists a maximal value $\alpha_{\max}$ of the coupling constant, for which non-trivial solutions exists. Namely $0 \leq \alpha \leq \alpha_{\max}$. This value is $\alpha_{\max} = 0.126$. The existence of such a maximal value translates to a maximal limit to both the value of L_g/L, as well as N_C. Physically, that means that L cannot become less than L_g, namely the skyrmion is not a black hole itself. At the same time, the number of colors of the theory has also be constrained from above in order to have non-trivial solutions.

Moreover, for each $\alpha \in [0, \alpha_{\max}]$ there exists a maximal value for the event horizon $x_h^{max,\alpha,\beta}$. In particular, as $\alpha \to \alpha_{\max}$, it follows that $x_h^{max,\alpha,\beta} \to 0$. The existence of $x_h^{max,\alpha,\beta}$ is the supporting evidence for the picture that we have provided, of the BH residing inside of the skyrmion. Roughly, this value follows the constraint $x_h^{max,\alpha,\beta} + L_g \sim L$. In other words, the sum of the maximal value of the horizon for each α and the gravitational radius of the skyrmion, cannot become greater than the size of the skyrmion itself.

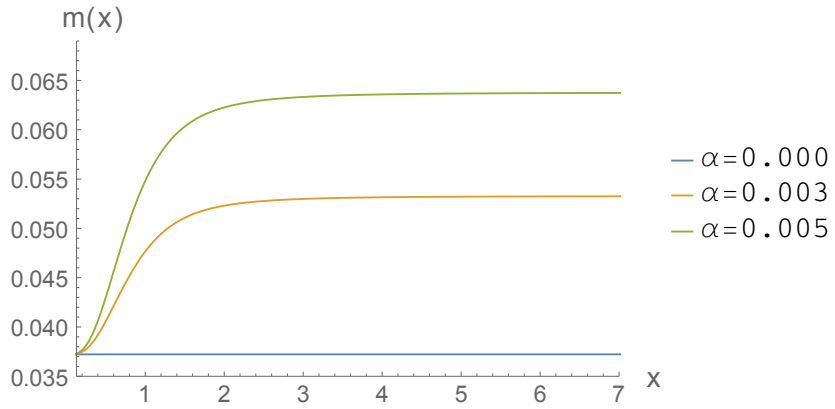

Figure 2.6: $m(x)$ vs x diagram for $\beta = 0, x_h = 0.07445$ and α as they appear in the legend. This highlights that as we increase the coupling constant α, more massive models emerge, as more energy is stored in (self-)interactions.

Taking β into account, we find that the main difference introduced is that $F(x)$ scales differently for large x, depending on β. Specifically, for large values of x, $F(x) \sim 1/x^2$ for $\beta = 0$, while $F(x) \sim e^{-m_\pi x}/x$ for $\beta \neq 0$. This is precisely the same scaling behaviour as in the flat-space case [52]. In Figures 2.4 - 2.5 one can see the effect of the β parameter on the mass and the hair profile function. One can observe that the values of the mass of those models at the horizon are in a decreasing order as β increases, since they are proportional to the horizon radius. However, contrary to the $\beta =$ fixed case, from some point onwards this order is reversed. This can be explained if one thinks of β as the mass of the hair. Models with larger β have more massive hair and so mass accumulates faster.

Chapter 3

Photon orbits

Up to this point we have discussed Skyrmion black holes and focused on the static spherically symmetric case. We have seen that the presence of hair changes the spacetime with respect to the static and spherically symmetric black hole solution of pure Einstein's theory, the Schwarzschild solution. In this chapter, we would like to start exploiting those differences and investigate whether they bear observational manifestations. As per most studies on black holes, we will start by studying null-geodesics and observational phenomena derived from them. We track down the differences and draw a connection between them and our current observational means, thus enabling us to comment on the probability of such an observation.

3.1 General characteristics

Before we start discussing geodesics, let us first have a look at how the spacetime is affected from the presence of hair. We would like to find out the extent to which it is affected, which in turn will motivate the study of geodesics.

In Section 2.2.4, we have presented Figures 2.2 - 2.5. Those were showing models characterized by different values for the set of parameters (α, β, x_h), with the common characteristic that the ADM mass of those models was the same. When comparing different black hole solutions, we should keep in mind that them having the same ADM mass is crucial in the sense that a distant object will get to experience the total gravitational force of all the mass lying inside the sphere centered at the black hole and extending all the way to object. Consequently, configurations with unequal ADM mass will be straightforward to distinguish by their effect on distant objects.

When looking at a Schwarzschild black hole, its mass is constant and specifically it holds that $x_h = 2m_{ADM}$. However, as it is evidenced by Figures 2.2 and 2.4, in the case of hairy BH models mass varies with x as it goes from the value $x_h^{hairy}/2$ at the horizon all the way to m_{ADM} asymptotically. Those models have mass stored in the hair themselves and the interactions. As a result, in the case of hairy BHs it holds that $x_h < 2m_{ADM}$. On can automatically make the following two observations. First of all, different event horizon radii lead to different deflection angles and black hole shadow. Secondly, depending on the model, the masses reach their asymptotic value at a distance which typically is of the order $x \sim (10 - 100)\ x_h$. This calls for more investigation on how the spacetime is affected, as these distances suggest that phenomena such as Einstein rings, which are

widely used in observations, could lead to wrong conclusions when interpreted under the wrong assumptions as to the nature of the black hole.

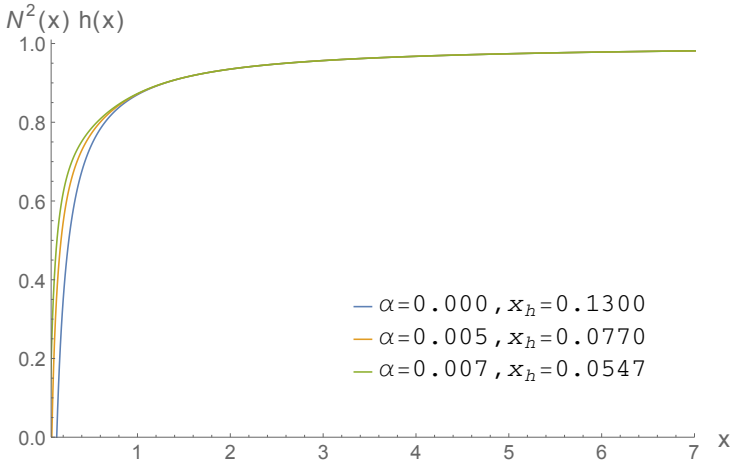

Figure 3.1: $g_{\tilde{t}\tilde{t}}$ vs x diagram for $\beta = 0$ and α, x_h as they appear in the legend. All three models have $m_{ADM} = 0.065$. The deviations from the Schwarzschild solution are evident.

By looking at the ansatz (2.27) for the metric, which in our current notation reads[1]

$$d\tilde{s}^2 = N^2(x)h(x)d\tilde{t}^2 - h(x)^{-1}dx^2 - x^2 d\Omega^2, \tag{3.1}$$

we see that the origin of the dissimilarities between the Schwarzschild and the skyrmion black hole spacetimes is the presence of the $N^2(x)$ term, which is in the Schwarzschild case is equal to 1, and the radial dependence of the mass function $m(x)$, present in both the g_{tt} and the g_{rr} term. Having seen how the mass function $m(x)$ behaves, we now focus on $N^2(x)$ and the metric functions g_{tt}, g_{rr}.

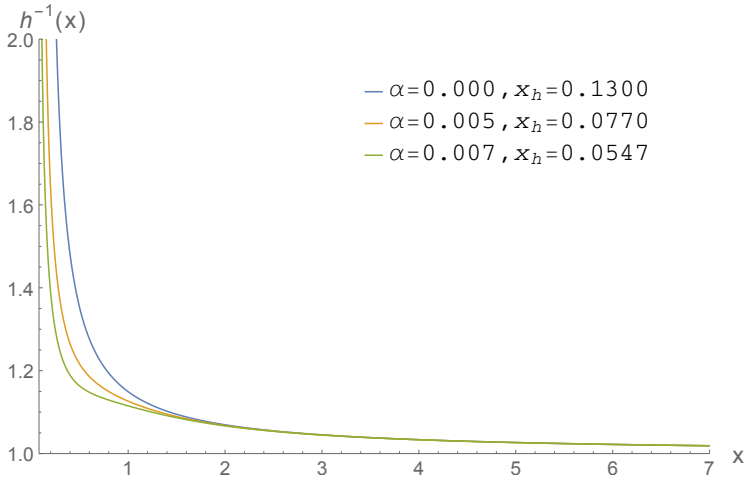

Figure 3.2: g_{xx} vs x diagram for $\beta = 0$ and α, x_h as they appear in the legend.

[1]Note that $\tilde{s}, \tilde{t}$ are the dimensionless versions of s, t. Specifically, $\tilde{s} = eF_\pi s$ and $\tilde{t} = eF_\pi t$.

The metric functions are drawn in Figures 3.1 and 3.2 for the same models as those shown in Figures 2.2 and 2.3. It is evident that the spacetime indeed changes by the presence of hair. The value of g_{tt} tends to be larger for hairy black holes, until it reaches its asymptotic value of 1. The opposite holds for g_{rr}. Note that this automatically means that all the interesting phenomena taking place around the black hole are going to be altered to some extent. For example, geodesics, as well as time dilation are going to be quantitatively different.

Note that in the models under investigation here the spacetimes differ significantly up to $x \sim (10 - 20)\, x_h$. Also, keep in mind that those models are far from extremal, in the sense that they are not characterized by large values for α and β. Finally, it has been examined and proven [53, 54] that the hair are not short, namely their presence and effect extends at least up to some distance outside the horizon. These facts indicate that the study of Einstein rings is rather prominent.

3.2 Geodesics

At this point we discuss geodesics. We start by producing the differential equations for our spacetime. A small recap of the main results in the Schwarzschild case is presented. Then, we move on to apply our results and compute deflection angles and photon sphere radii in order to investigate how they are altered and how much they are affected by the presence of hair. A more extensive exposition of the formulation of the problem can be found in [55].

3.2.1 Formulation

Particles in a generic spacetime move along geodesics. Geodesics from a physical point of view is a way of describing the shortest path between 2 points. As such, they can be found by minimizing the length

$$S = \int ds = \int d\lambda \, \frac{ds}{d\lambda} = \int d\lambda \, \sqrt{g_{\mu\nu} \frac{dx^\mu}{d\lambda} \frac{dx^\nu}{d\lambda}}, \tag{3.2}$$

where we have assumed the existence of a metric tensor $g_{\mu\nu}$ and λ is an affine parameter. By extremizing the aforementioned expression we obtain the geodesic equation[2]

$$\frac{d^2 x^\alpha}{d\lambda^2} + \Gamma^\alpha{}_{\mu\nu} \frac{dx^\mu}{d\lambda} \frac{dx^\nu}{d\lambda} = 0, \tag{3.3}$$

$\Gamma^\alpha{}_{\mu\nu}$ being the Christoffel symbols of the given metric.

One can thus compute the Christoffel symbols and obtain the geodesic equations. However, there is a more illustrative way to compute the geodesic equation in the case

[2]Note that the caveat of this method is that the quantity appearing in the Euler-Lagrange equations is a square root. The problem thus cannot be defined when investigating null-geodesics, since at some point we will be dividing by 0. This can either be treated by getting rid of the square root by introducing an einbein field e, or by looking at the problem from a different perspective and define geodesics as the curves along which parallel transport preserves the tangent vector. Both ways turn out to be equivalent.

of a static and spherically symmetric spacetime, as the one under investigation. Such a spacetime admits 2 Killing vectors, which in our coordinate system can be written out as

$$t^\alpha = (1,0,0,0), \tag{3.4}$$
$$\phi^\alpha = (0,0,0,1). \tag{3.5}$$

As a result, there are 2 related conserved quantities

$$t^\alpha u_\alpha = e, \tag{3.6}$$
$$\phi^\alpha u_\alpha = -l, \tag{3.7}$$

which can be identified with the energy per unit mass and the angular momentum per unit mass if one takes $r \to \infty$.

We can now start from the constant of motion $u^\alpha u_\alpha = \kappa$, where

$$\kappa = \begin{cases} 1 & \text{, timelike geodesics} \\ 0 & \text{, null geodesics} \end{cases}. \tag{3.8}$$

We write everything down in terms of our initial units and in the end we will convert our expressions to the dimensionless units introduced. Since our spacetime is spherically symmetric and the angular momentum of our probe particle is conserved, we can choose a $\theta-$level, which we take to be $\theta = \pi/2$, namely the equator. The canonization then reads

$$\begin{aligned} \kappa &= u^\alpha u_\alpha \\ &= g_{\mu\nu} u^\mu u^\nu \\ &= g_{tt}\left(\frac{e}{g_{tt}}\right)^2 + g_{rr}\left(\frac{dr}{d\lambda}\right)^2 + g_{\phi\phi}\left(\frac{l}{g_{\phi\phi}}\right)^2 \\ &= \frac{e^2}{N^2(r)H(r)} - \frac{1}{H(r)}\left(\frac{dr}{d\lambda}\right)^2 - \frac{l^2}{r^2}, \end{aligned} \tag{3.9}$$

where λ can be taken to be the proper time τ in the case of massive particles and

$$H(r) = 1 - \frac{2GM(r)}{r}. \tag{3.10}$$

We have now obtained the geodesic equation, better written as

$$\left(\frac{dr}{d\lambda}\right)^2 = \frac{e^2}{N^2(r)} - H(r)\left(\frac{l^2}{r^2} + \kappa\right). \tag{3.11}$$

One can now integrate this differential equation. Furthermore, one could perform a change of variables and write the corresponding differential equation relating coordinate time t or ϕ to r. Let us first worry about the orbits and then discuss deflection angles. Thus, we will differentiate once more with respect to λ in order to avoid taking the square root on both sides and get a 2^{nd} order differential equation instead. After taking into account the definition of $H(r)$ and simplifying our expression we get

$$\frac{d^2r}{d\lambda^2} = -\frac{e^2}{N^3(r)}\frac{dN(r)}{dr} + l^2\frac{\left(2r - 6GM(r) + 2rG\frac{dM(r)}{dr}\right)}{2r^4} + \kappa G\frac{\left(r\frac{dM(r)}{dr} - M(r)\right)}{r^2}. \tag{3.12}$$

Thus, in order to find the orbit of a test particle, we can solve the following system of 1^{st}-order differential equations

$$\frac{d\phi}{d\tilde{\lambda}} = \frac{\tilde{l}}{x^2}, \tag{3.13a}$$

$$\frac{dx}{d\tilde{\lambda}} = p, \tag{3.13b}$$

$$\frac{dp}{d\tilde{\lambda}} = -\frac{e^2}{N^3(x)}\frac{dN(x)}{dx} + \tilde{l}^2\frac{\left(x - 3m(x) + x\frac{dm(x)}{dx}\right)}{x^4} + \kappa\frac{\left(x\frac{dm(x)}{dx} - m(x)\right)}{x^2}, \tag{3.13c}$$

where we have reverted back to our newly set dimensionless notation, with $\tilde{l} = eF_\pi l$ and $\tilde{\lambda} = eF_\pi\lambda$.

In order to solve the system of differential equations we have to provide the initial position of our particle as initial conditions for (3.13a)(3.13b) and the component of its initial velocity which lies along the radial direction as initial condition for (3.13c). By specifying its angular momentum per unit mass $\tilde{l}$ and energy per unit mass e, we have completely determined the motion of the particle.

Let us now focus our attention on deflection angles. That is extract a relation between ϕ and x, indicating how the orbit changes as the particle moves through the spacetime. Keeping in mind Eq. (3.7) in our dimensionless units it holds

$$\left(\frac{dx}{d\phi}\right)^2 = \left(\frac{dx}{d\tilde{\lambda}}\right)^2\left(\frac{d\tilde{\lambda}}{d\phi}\right)^2 = \left(\frac{dx}{d\tilde{\lambda}}\right)^2\left(\frac{x^2}{\tilde{l}}\right)^2. \tag{3.14}$$

So, one has

$$\left(\frac{dx}{d\phi}\right)^2 = \left[\frac{e^2}{N^2(x)} - h(x)\left(\frac{\tilde{l}^2}{x^2} + \kappa\right)\right]\left(\frac{x^2}{\tilde{l}}\right)^2, \tag{3.15}$$

which in the case of photons becomes

$$\phi(x_2) - \phi(x_1) = \int_{x_1}^{x_2} \frac{dx}{x\sqrt{h(x)}\sqrt{\frac{x^2}{N^2(x)h(x)}\frac{e^2}{\tilde{l}^2} - 1}}. \tag{3.16}$$

The deflection angle of a particle being initially at a distance x_1 and moving all the way to some distance x_2 is defined through

$$\Delta\phi = \phi(x_2) - \phi(x_1) - \pi. \tag{3.17}$$

This definition is such that in the case of a particle moving far away from the black hole the deflection angle turns out to be 0, while for a particle which is scattered back at the direction from which it originally came from it evaluates to π. This indeed is rather reasonable, as in the first case the particle remains unaffected by the black hole, while in the second case the direction of motion is inverted.

3.2.2 Schwarzschild recap: Null geodesics

We will be focusing on photon orbits, namely null geodesics at later parts of this work. Thus, we present some general results for them in the case of a Schwarzschild black hole carrying no hair. Essentially, we only wish to provide a rough picture of the possible orbits. A more extensive review can be found in [56].

In the case of the Schwarzschild black hole Eq. (3.11) becomes

$$\left(\frac{dr}{d\lambda}\right)^2 = e^2 - H(r)\left(\frac{l^2}{r^2} + \kappa\right), \tag{3.18}$$

where we have set $N^2(r) = 1$. This equation can be rearranged as

$$\tilde{E} = \frac{1}{2}\left(\frac{dr}{d\lambda}\right)^2 + \tilde{V}(r), \tag{3.19}$$

where now we have defined the hypothetical energy and potential as

$$\tilde{E} = \frac{e^2 - \kappa}{2}, \tag{3.20}$$

$$\tilde{V}(r) = \frac{1}{2}\left(\frac{l^2}{r^2} - \frac{2GM}{r}\kappa - \frac{2GMl^2}{r^3}\right) \tag{3.21}$$

respectively. One can easily switch to our dimensionless units by taking at the same time $GM \to m$, $r \to x$, $l \to \tilde{l}$ and $\lambda \to \tilde{\lambda}$.

We can really profit from Eq. (3.19), as it reduces the problem of investigating orbits to studying the motion of a particle carrying energy $\tilde{E}$ in the one-dimensional central potential $\tilde{V}(r)$. Now, if we restrict ourselves to the case of photons, namely take $\kappa = 0$, the following scenarios emerge:

1. **Circular orbits**: Following the formulation of the problem as the motion of a particle in a central potential, we can track down circular orbits, if they exist, as the extrema of the hypothetical potential $\tilde{V}(r)$.

$$\begin{aligned}\frac{d\tilde{V}(r)}{dr} = 0 \Rightarrow \frac{l^2}{2}\left(-\frac{2}{r^3} + \frac{6GM}{r^4}\right) = 0 \\ \Rightarrow r = 3GM\end{aligned} \tag{3.22}$$

   So, there indeed exists a circular orbit at $r = 3GM$, also called the photon sphere, which is unstable since

$$\frac{d^2\tilde{V}(r)}{dr^2} = \frac{3l^2}{r^5}(r - 4GM) \Rightarrow \left.\frac{d^2\tilde{V}(r)}{dr^2}\right|_{r=3GM} < 0. \tag{3.23}$$

2. **Incoming/outcoming photons**: Initially, let us define the impact parameter

$$b = \left|\frac{l}{e}\right|, \tag{3.24}$$

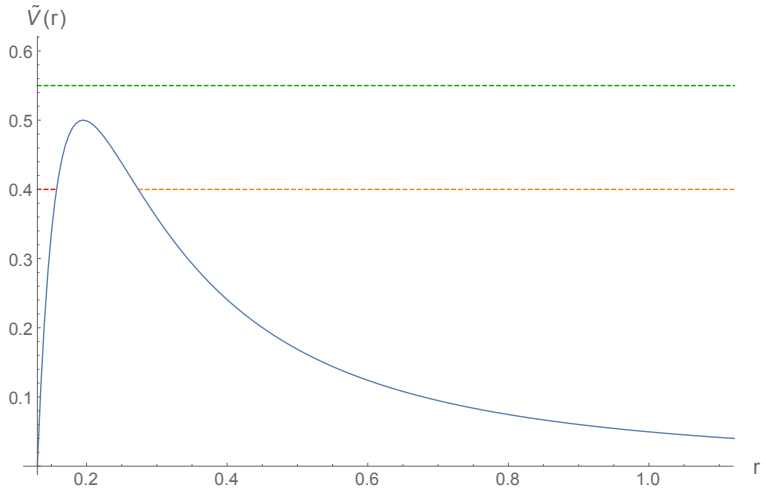

Figure 3.3: The hypothetical potential for the $(\alpha, \beta, x_h) = (0, 0, 0.13)$ case as the blue line. At the maximum of the potential lies the circular orbit. The green dashed line can correspond to either an incoming photon getting swallowed by the black hole, or an outcoming photon which escapes. The orange dashed line is an incoming photon getting scattered back at infinity. Finally, the red dashed line is an outcoming photon captured by the black hole.

which from a geometric point of view is the distance of the photon from the x-axis at infinity, in a coordinate system with the black hole at the origin and the x-axis parallel to the orbit of the photon at infinity.

In the case of the circular orbit, which is at the maximum of the potential $\tilde{V}_{max} = \tilde{V}(3GM)$, it is easy to see from Eq. (3.19) for $r = 3GM$ that $b_c = \sqrt{27}M$. This value is important when identifying the possible scenarios for an incoming/outcoming photons.

- Incoming: There are two possible fates for such photons. Either $\tilde{E}_{ph} < \tilde{V}_{max} \Leftrightarrow b > b_c$ in which case the photon is scattered back at infinity, or $\tilde{E}_{ph} > \tilde{V}_{max} \Leftrightarrow b < b_c$ which means that the photon will fall inside the black hole.
- Outcoming: Again there are two cases, which are opposite than before. When $\tilde{E}_{ph} > \tilde{V}_{max} \Leftrightarrow b < b_c$ then $r > 2GM$ and the photon escapes the black hole, while when $\tilde{E}_{ph} < \tilde{V}_{max} \Leftrightarrow b > b_c$ we get $r < 3GM$ and the photon again is swallowed by the black hole.

3.2.3 Numerical results

As we have already seen, Skyrmion black holes have mass that is enclosed and can be attributed to the black hole and then some more on the exterior of the black hole. Thus, the main difference between a Skyrme black hole and a Schwarzschild black hole of the same total mass is that this mass is distributed differently and they have different horizon radii. One thus expects that photon orbits will be altered.

Qualitatively the orbits for the models under investigation should be the same. Namely,

we expect to find a circular photon orbit, which however will not be exactly at $x = 3x_h/2$ as in the Schwarzschild case. A proof for the existence of at least one such orbit can be found in Appendix A. So, the differences that we expect are of quantitative nature. This can indeed be seen in Figure 3.4, where orbits for the same impact parameters are presented for a Schwarzschild black hole with chiral hair and a Skyrme black hole configuration.

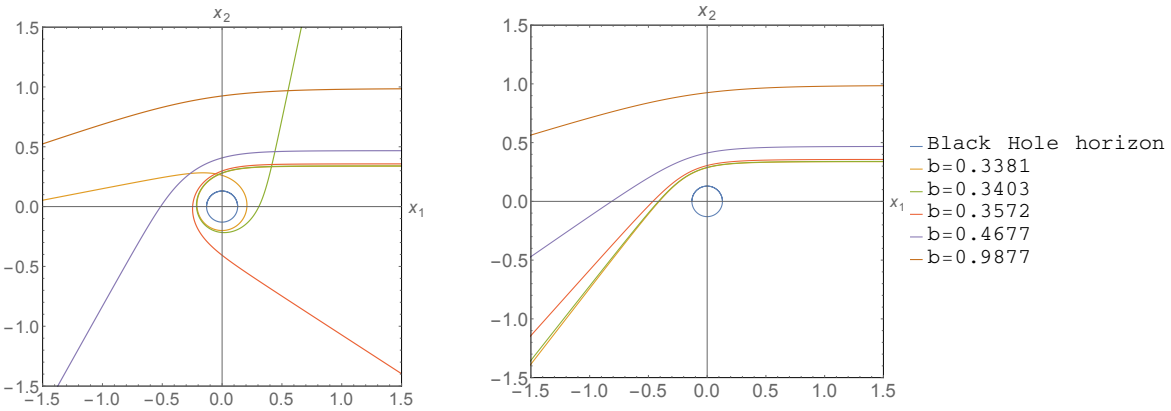

(a) $(\alpha, \beta, x_h) = (0, 0, 0.13)$ (b) $(\alpha, \beta, x_h) = (0.005, 0, 0.077)$

Figure 3.4: Photon orbits with the same impact parameters in the background of (a) a Schwarzschild black hole with chiral hair and (b) a Skyrme black hole. Evidently, the orbits differ. The parameters characterizing these black holes can be found in the respective subcaptions.

A more concrete study of the orbits comes through the study of deflection angles. An investigation of deflection angles for photons can be found in Figure 3.5. There deflection angles for many different impact parameters and models are plotted against the inverse of the closest approach of the photon in each case. The largest value of $1/x_{min}$ is different for each model, since the models have different horizon radii. This results in different radii at which the photon spheres lie as well. For each model, the largest value of $1/x_{min}$, to which they asymptotically tend, is the radius of its photon sphere. At the same time, as we move towards smaller values of $1/x_{min}$, we see that the values of $\Delta\phi$ come closer to each other and from some point onwards they coincide. As stated, all configurations have the same ADM mass. Thus, a photon which moves at a large distance from the black hole cannot resolve whether this mass can be solely attributed to a black hole without hair or if hair are present as well. One can read from the diagram that for the models under investigation this happens at $1/x_{min} \approx 0.5 \Rightarrow x_{min} \approx 2$. Indeed, looking back at Figures 3.1 - 3.2, where the metric functions for some of those models are presented, one can see that this is the distance at which the metrics become identical. As a result, the spacetimes from this point and outwards are identical and are thus expected to host phenomena which admit the same behaviour.

The fact that $\Delta\phi$ for all the models present in Figure 3.5 approach some value at large $1/x_{min}$ indicates the presence of a photon sphere for each one of those models. Instead of looking for this asymptotic value through deflection, one can look into the zeros of

$$G(x) = \frac{h(x)}{N(x)}\frac{dN(x)}{dx} + \frac{1}{2}\frac{dh(x)}{dx} - \frac{h(x)}{x}, \tag{3.25}$$

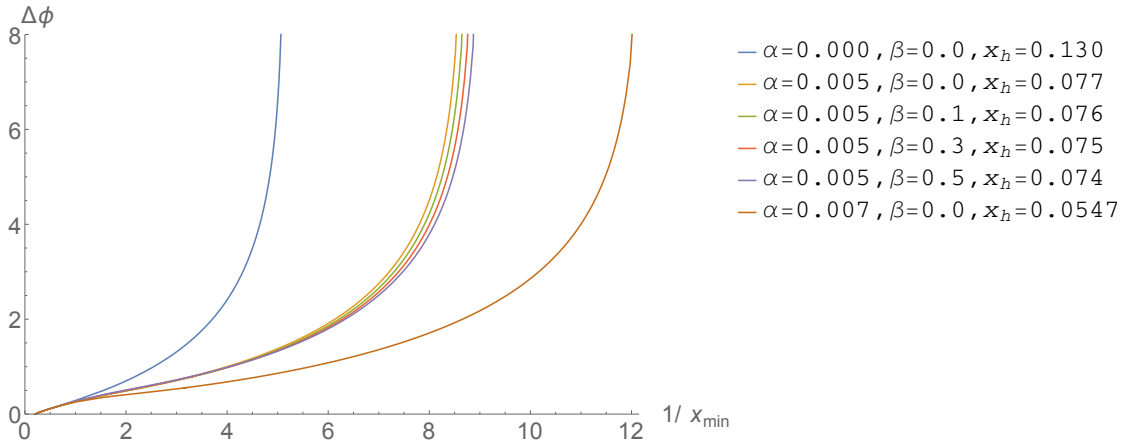

Figure 3.5: Deflection angle $\Delta\phi$(rad) vs closest approach $1/x_{min}$ diagram for many black hole configurations of the same ADM mass. Different horizon radii and the fact that all models have the same total mass determine the behaviour at large and small $1/x_{min}$ respectively.

as argued in Appendix A. If this non-linear equation admits more than one zeros, then we are interested in the smallest one.

In the case of the Schwarzschild black hole, we have found that the photon sphere lies at a distance $x_{phot} = 3m_{BH} = 3x_h/2$. The presence of hair is bound to alter this. An interesting question to pose is by how much the photon sphere is moved. So, we are looking into the radius x_{phot} at which the photon sphere for each model lies and compare it with

$$x_{phot,nh} = \frac{3x_h}{2}, \tag{3.26}$$

which is where the photon sphere would be if it were not for the hair.

Table 3.1 presents the data aspiring to provide us with an answer. Photonspheres are indeed altered and we find them a bit further than in the Schwarzschild case. We can understand this as in the Schwarzschild case the mass inside the photon sphere is that of the black hole. In the case of Skyrmion black holes we have some more mass coming from the presence of the hair. So, the gravitational pull at the radius suggested by the study of Schwarzschild black holes will be greater. Since photon spheres represent the distance at which we find the last circular photon orbit, it should be moved a bit further, since the additional gravitational pull will lead to any photon circling the black hole at a distance $x_{phot,nh}$ to fall inside the black hole.

One cannot conclude directly whether this change is significant or not, since the quantities presented here are dimensionless and they strongly depend on the parameters e, F_π of the model. Depending on the values of those parameters the distances and subsequently the change in the photon sphere radius can be rather small or large in terms of real life units. Thus, we investigate the relative difference defined as

$$\frac{\delta x}{x} = \frac{x_{phot} - x_{phot,nh}}{x_{phot,nh}} \times 100\%, \tag{3.27}$$

which shows us the deviation from the corresponding result in the Schwarzschild case.

The relative differences are really small for the models under investigation here. This means that there is no substantial change in the radius of the photon sphere due to the presence of the hair. We can however make the following observation. For the models which have the same α, the change in the radii of their photon spheres becomes stronger as β is increased. Recall that β is indicative of the mass of the skyrmion hair. One could think of this result in the following way. The more mass that is enclosed between $x_{phot,nh}$ and x_h, the further away the photon sphere should lie. Thus, as part of a rather pedestrian approach, one can look at $m'(x)$ for $x \in [x_h, x_{phot}]$ for an explanation. This follows from the fact that the mass related to the presence of hair enclosed in the photon sphere can be approximated as $\delta m|_{x_h}^{x_{phot}} \approx m'(x_0) \times (x_{phot} - x_h) \approx m'(x_0) \times x_h/2$ for some $x_0 \in [x_h, x_{phot}]$. Indeed, for all the models present in Table 3.1, the derivative of the mass aligns with the relative differences obtained here.

Table 3.1: Photonspheres for many models and their relative difference from $x_{phot,nh}$.

Model (α, β, x_h)	x_{phot}	$x_{phot,nh}$	$\frac{x_{phot}-x_{phot,nh}}{x_{phot,nh}} \times 100\%$	Maximum distance d (in 10^9 m_{ADM})
$(0, 0, 0.13)$	0.195	0.195	0	-
$(0.005, 0, 0.077)$	0.11558	0.1155	0.06755	4.2
$(0.005, 0.1, 0.076)$	0.11408	0.114	0.0702	4.28
$(0.005, 0.3, 0.075)$	0.11259	0.1125	0.08193	4.358
$(0.005, 0.5, 0.074)$	0.11111	0.111	0.10191	4.437
$(0.007, 0, 0.05468)$	0.08205	0.08202	0.04092	5.974

If we denote the mass related to the presence of the hair as m_{hair} and look at the limiting case we can state the following. If $m_{hair} << m_{BH}$ then photon spheres remain practically unaltered, while in any other case there is a change which becomes stronger as m_{hair} increases. However, at the same time models with large m_{hair} could possibly be characterized as not so realistic.

At the same time in Table 3.1 we also provide the maximum distance d at which one could observe the difference in the photon sphere radii between each Skyrme black hole and the Schwarzschild one. In order to compute this we have used the fact that the Event Horizon Telescope has achieved angular resolutions better than 60 μarcsec, which is the value which we used. The distances are expressed in units of 10^9 m_{ADM} and look rather promising for the models under consideration.

In the case of a Schwarzschild black hole, associated to the photon sphere is an impact parameter as we have seen in Section 3.2.2. This impact parameter is $b_c = \sqrt{27} m_{BH}$. In Table 3.2 we present the corresponding impact parameters for all the models investigated here. Since in the case of a Skyrmion black hole the black hole mass and the ADM mass of the system do not coincide, we check how close those impact parameters are to the Schwarzschild value, which we take both with respect to m_{BH} and m_{ADM}. Obviously, since $m_{BH} < m_{ADM}$, the first ratio is expected to be greater.

We see, that the effect of the black hole mass is stronger on impact parameters than

that of the hair, as the ratios we obtain are better normalized with m_{BH} than m_{ADM}. The presence of hair though does bear an effect on the impact parameter which is not insignificant, as it is of the order of $\sim 7\%$ using relative difference as a measure again. This answers the question of what would happen if instead of taking the same impact parameters for the photon orbits in Figure 3.4, we normalized them with respect to the mass attributed solely to the black hole in case (b). The orbits would still be different, though not as much as they are currently shown. Finally, note that the impact parameters, as photon spheres, are increasing with respect to the Schwarzschild value, since they are feeling the pull of the additional mass attributed to the presence of hair.

Table 3.2: Impact parameters corresponding to photon spheres and deviation from the corresponding Schwarzschild result.

Model (α, β, x_h)	impact parameter b	$\frac{b}{\sqrt{27}m_{BH}}$	$\frac{b}{\sqrt{27}m_{ADM}}$
$(0, 0, 0.13)$	0.33775	1	1
$(0.005, 0, 0.077)$	0.21265	1.063	0.63
$(0.005, 0.1, 0.076)$	0.21001	1.064	0.626
$(0.005, 0.3, 0.075)$	0.2083	1.069	0.621
$(0.005, 0.5, 0.074)$	0.20706	1.077	0.616
$(0.007, 0, 0.05468)$	0.15414	1.085	0.456

We notice that impact parameters corresponding to orbits which asymptotically end up on the photon sphere are altered more significantly than photon spheres themselves. There is an explanation for that. Photon spheres capture the behaviour of the spacetime really close to the back hole, but at the same time remain ignorant of what happens at larger distances. However, a photon coming from infinity and passing close by the black hole can resolve this. This of course bears consequences to its impact parameter, which is strongly dependent on its energy and angular momentum.

The underlying reason for studying models with the same ADM mass is that this is the mass seen by an observer lying in the asymptotic region. Black holes with different ADM masses will influence distant objects differently, thus making it relatively simple to distinguish them. However, one could try and tackle the question of how much the mass originating strictly from the presence of hair affects photons in the following way. Consider two or more black holes which have the same horizon radius and thus black holes of the same mass lying at the center of the configuration. Now, the first one should be a Schwarzschild black hole, having no additional mass and the rest of them Skyrmion black holes which have a non-zero mass distribution outside of the horizon as well. This is a non-physical scenario, but it can shed some light on the importance of mass attributed to the hair.

In Figure 3.6 we consider such a case. We worry about two black holes characterized by $(\alpha, \beta, x_h)_1 = (0, 0, 0.07445)$ and $(\alpha, \beta, x_h)_2 = (0.003, 0, 0.07445)$ respectively. We then compute the deflection angles $\Delta\phi_1, \Delta\phi_2$ for many impact parameters for both black holes and compare them through

$$\Delta\phi^{rel} = \Delta\phi_2 - \Delta\phi_1, \tag{3.28}$$

where $\Delta\phi_i$ are defined though (3.17).

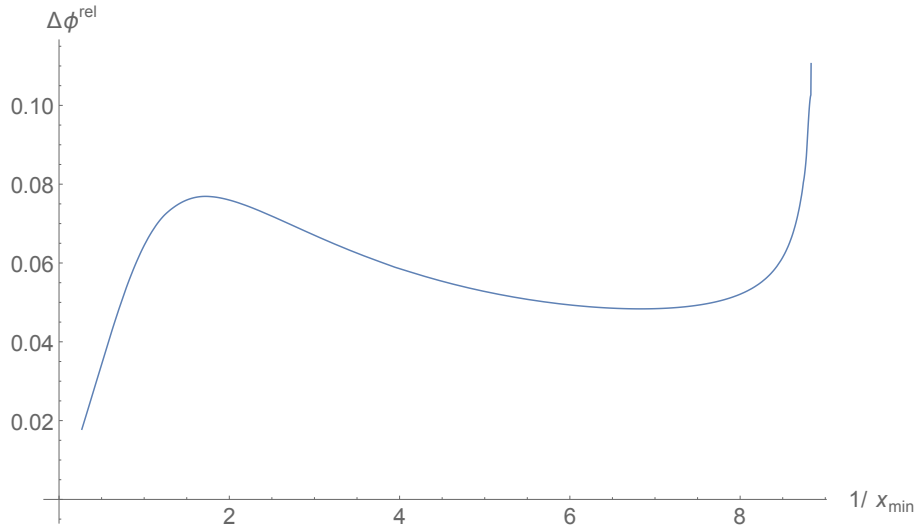

Figure 3.6: Difference in deflection angles $\Delta\phi^{rel}$(rad) between two black holes with $(\alpha, \beta, x_h)_1 = (0, 0, 0.07445)$ and $(\alpha, \beta, x_h)_2 = (0.003, 0, 0.07445)$ vs closest approach $1/x_{min}$ diagram. The models have the same horizon radius and thus black hole mass, but their ADM masses are $m_{ADM,1} = 0.0372$ and $m_{ADM,2} = 0.0533$ respectively.

Let us now examine Figure 3.6, keeping in mind that the mass function for those two black holes can be found as part of Figure 2.6. Since the Skyrmion black hole is the one with a non constant mass function, we examine the motion of a photon starting with a very large impact parameter and then gradually decreasing it, closely following the Skyrmion black hole mass that the photon resolves. For very large distances, the photon remains unaffected by the presence of any of the black holes and thus $\Delta\phi^{rel}$ tends to 0 for very small $1/x_{min}$. Then, as it comes closer to each black hole it starts feeling its presence and thus $\Delta\phi^{rel}$ is increased as $m_{ADM,1} < m_{ADM,2}$. At some point, in the case of the Skyrmion black hole it reaches the region where $m(x)$ varies. From this point onwards it starts spending parts of its orbit in regions where it feels a mass $m(x) < m_{ADM,2}$. So, as it comes closer and closer, $\Delta\phi^{rel}$ is bound to start decreasing. Thus a maximum is encountered at some point. That maximum is in general quite close to the point x_m at which $m'(x_m) = 0$. Finally, when the photon approaches the photon sphere and thus the black hole, $\Delta\phi^{rel}$ is drastically increased. One could say that going by the black hole at such a small distance leads to the black hole dominating its scattering and significantly amplifying any difference in the deflection angles there is.

In general, the differences we observe in this case are about $\Delta\phi^{rel} \approx 0.06$ rad $\approx 3.5°$. They can in no case be considered insignificant. Depending on the additional mass due to the hair this value varies, but in general this result is rather representative. Furthermore, note that even if through some combination of α and β one builds two models which have the same ADM mass and horizon radius at the same time, the mass functions are going to be different and thus their $\Delta\phi^{rel}$ will only agree for very large distances.

Based on all the aforementioned considerations, we can conclude that the presence of hair affects up to some notable extent photon orbits. However, as we have seen, the

photon spheres remain practically unaffected. Even so, if one knows up to some high accuracy the mass of the black hole under observation, he could possibly distinguish the difference in the photon sphere with respect to what he would expect assuming it is a Schwarzschild black hole. This mainly depends on the mass stored in the hair, but for the models under investigation here the numbers are promising. Furthermore, in the case of rotating black holes and for a different family of hairy black holes solutions, the effect of the hair on the shadow of the black hole leads to observationally prominent phenomena [57, 58, 59, 60, 61, 62, 63]. One could test whether this is the case for Skyrmion black holes as well.

3.3 Skyrme black holes as Gravitational lenses

Up to this point we have shown that there are indeed major differences between a Schwarzschild and a Skyrmion black hole of the same ADM mass. We have indeed witnessed that their signature is strong in the spectrum of phenomena related to photon scattering. Furthermore, we have observed that the more time a photon spends inside the region where the spacetimes are differentiated, the better probe it becomes in distinguishing between the two. Even better if the photon spends time moving at large distances and also approaches the black hole as well.

All these facts motivate the study of Skyrme black holes as gravitational lenses. By studying the collinear case, namely Einstein rings, we wish to further investigate the mark that photons travelling through the hair leave. On the other hand, the not collinear case will provide us with a more extremal example, allowing us to investigate if we can make a direct use of the fact that $m_{ADM} \neq m_{BH}$ in the case of Skyrmion black holes. Nice reads on the topic of gravitational lenses are [64, 65, 66, 67, 68].

3.3.1 Description

The idea of a very massive object acting as a gravitational lens is quite old. It is a consequence of the bending of light by some matter distribution and was suggested as an observationally interesting phenomenon quite early in the years of General Relativity, back in the 1920s. As our observational capabilities have increased through the years, with large radio telescopes, the Hubble space telescope and so on, the field has managed to draw a lot of attention, especially in more recent years. It is a prominent candidate to provide answers both to the field of gravity, through testing General Relativity and alternative theories of gravity, as well as to the field of cosmology by observing objects lying at immensely large distances.

Essentially, the idea is that there is a source (S) which emits light. Some rays pass in the vicinity of some mass (L) capable of bending their trajectory. Now depending on the geometry of the problem, some of those rays make it to the observer. Broadly speaking, the observer, based on the data from the affected light rays he receives, can get a wrong perception as to the position of the object on the sky or he could observe multiple images, arcs, rings or just some variation in the amount of light received.

Objects that can act as gravitational lenses are for example stars, black holes, galaxies and galaxy clusters. Their efficiency and detectability varies with their distance from the observer. Depending on how evident the lensing is, it is divided in three main classes:

1. **Strong lensing**: This is the case where the traces of lensing are easily made out as e.g. rings and multiple images.

2. **Weak lensing**: Here the distortion of the source is so small that it cannot be detected for a single source individually. A statistical analysis of many sources has to be performed instead and then the signature of lensing is visible, though weak.

3. **Microlensing**: Here no distortion can be observed. However, the flux received from the source varies with time, which indicates the presence of some object acting as a gravitational lens.

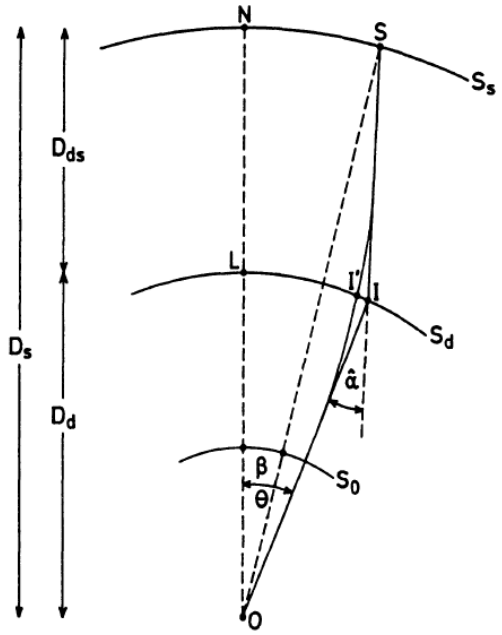

Figure 3.7: The geometry of a gravitational lens system. This is the general case where the source (S), the center of the lens (L) and observer (O) are not taken to be collinear. The distances are as seen in the figure, while S_S and S_d are spheres centered at O on which S and L lie. The line through O and L is the optical axis. The undisturbed angular position of the source with respect to the optical axis is denoted by $\boldsymbol{\beta}$. A light ray emitted by S crosses S_d at I', while I is where the tangent to the geodesic of the ray at S crosses S_d. Due to the smallness of the angles involved they can be taken to coincide as a very accurate approximation. Due to the same reasoning one can think of the spheres S_d, S_S in terms of their tangent planes. The presence of L causes the ray to be deflected by $\hat{\boldsymbol{\alpha}}$, so that an image of the source is observed at position $\boldsymbol{\theta}$. Finally, N is the point where the optical axis intersects the sphere S_S and S_0 is a sphere representing the apparent sky of the observer. Note that the position of the source (S) and the observer (O) could be interchanged with the appropriate modifications in the relevant equations. The figure is adopted from [64]

Let us now direct our attention to the geometry of the problem. In our notation, as seen in Figure 3.7, S is the source, L the mass distribution acting as a lens, O the observer

and D_S, D_d, D_{ds} the distances observer-source, observer-lens and lens-source. The angles are defined as seen in the figure, whereas in the caption a more detailed explanation of it is provided. In the case where scenarios of cosmological nature are investigated, these distances should be replaced with the corresponding redshifts.

As described in the caption of Figure 3.7, the deflection angles are rather small and we can think of the spheres as their tangent planes. They will be called the source plane and lens plane respectively. The separation of the light ray from the optical axis in the lens plane will be described by a two-dimensional vector $\boldsymbol{\xi}$.

In order to relate the observed angular position $\boldsymbol{\theta}$ with the real angular position $\boldsymbol{\beta}$ we take a look at the geometry of the problem, assuming that we are in the asymptotic region so we can think in terms of Euclidean geometry. Then, in order for the ray to reach the observer it should hold that

$$\sin(\boldsymbol{\theta} - \boldsymbol{\beta}) D_S = \hat{\boldsymbol{\alpha}}(\boldsymbol{\xi}) D_{ds}, \tag{3.29}$$

which is also called the lens equation. All the observed deflection angles are really small and so this can also be written as

$$\boldsymbol{\beta} D_S + \hat{\boldsymbol{\alpha}}(\boldsymbol{\xi}) D_{ds} = \boldsymbol{\theta} D_S. \tag{3.30}$$

The apparent usefulness of Eq. (3.29) is that given the observed position and the mass distribution one has access to both $\boldsymbol{\theta}$ and $\hat{\boldsymbol{\alpha}}(\boldsymbol{\xi})$. Thus, the real position of the source $\boldsymbol{\xi}$ comes as the solution to Eq. (3.29). Note that usually the problem is for a given image to find the mass distribution that caused the distortion.

Note that the $\hat{\boldsymbol{\alpha}}(\boldsymbol{\xi})$ present here is the one defined in Eq. (3.17), only here we have switched our notation to match the corresponding literature. Furthermore, keep in mind that due to the symmetry of the spacetime the orbit from a very large distance up to the point of closest approach to the lens is going to be the same as from that point all to way to some large distance. Thus, one can also write

$$\hat{\boldsymbol{\alpha}}(x_{min}) = 2|\phi(x_{min}) - \phi(\infty)| - \pi. \tag{3.31}$$

Another important property of gravitational lenses is that, as per all objects described as lenses, they also magnify the source. The magnification factor μ is the ratio of the flux we receive from the source with lensing, over the flux we would receive in the absence of the lens. Keeping in mind that gravitational light deflection is not connected to absorption or emission and that it introduces no additional frequency shift, the surface brightness of the source is the same as if there was no gravitational lens. Since the flux is the product of the surface brightness with the solid angle that the source spans on the sky, we get that the magnification factor is the ratio of the solid angle $\Delta\omega$ that the source subtends on the sky after its been lensed, over the solid angle $(\Delta\omega)_0$ it normally subtends. Thus it reads

$$\mu = \frac{\Delta\omega}{(\Delta\omega)_0}, \tag{3.32}$$

where if we denote the area that the source spans without lensing as A_S and after lensing as A_I, we can write the solid angles as

$$(\Delta\omega)_0 = \frac{A_S}{D_S^2} \quad \text{and} \quad \Delta\omega = \frac{A_I}{D_d^2}, \tag{3.33}$$

which in general are not equal to each other.

Note that we have used the geometrical setup for the not collinear case. If one were to place the source on the optical axis, then a rather interesting phenomenon emerges. We have $\boldsymbol{\xi} = 0$ and plugging it back into Eq. (3.29) we get

$$\boldsymbol{\theta} = \frac{D_{ds}}{D_S}\hat{\boldsymbol{\alpha}}(\boldsymbol{\xi}). \tag{3.34}$$

If now the gravitational lens was axisymmetric, with the axis of symmetry coinciding with the optical axis, $\boldsymbol{\theta}$ would be the same all around the optical axis. Thus, the source would be imaged as a ring around the optical lens. Those rings are called Einstein rings. In the case where the lens did not admit such a symmetry, but the system of observer-lens-source was collinear, we would still obtain some geometrical shape, which would not be a ring though.

The mathematical formalism of the problem is such that it allows for an infinite number of Einstein rings in the collinear case. The one discussed usually in the literature is the most prominent one and it corresponds to the case where light emitted at a specific angle from the source is slightly deflected by the gravitational lens, as much as needed to reach the observer. This is the first Einstein ring. One however could imagine the case where the light from the source circles the source once and then reaches the observer. This would be the third Einstein ring. Of course, circling the source more than once leads to the fifth, seventh and so on Einstein rings.

At the same time, if we have another alignment where the source and the observer lie on the same side of the source, we can again have Einstein rings. In this case, the light from the source has to make a U-turn near the photon sphere of the lens. This is the second Einstein rings and if light ends up circling the lens more times we get the fourth, sixth and so on Einstein rings. Of course, in this alignment, one has also the direct image of the source from light emitted from the source which moved through space unaffected and reached the observer. This could also be denoted as the zeroth Einstein ring.

Note that the numbering of the rings corresponds to the order in which we meet them as we move closer and closer to the gravitational field. So, the first ring lies on the outside of the second, which in turn is larger than the third and so on. The use of the word "infinite" when describing how many Einstein rings correspond to each source is quite strong and we should highlight that at some point the assumptions of the model break and so we have a finite number of rings. Furthermore, since higher order rings have smaller angular diameters, they are more difficult to observe. There are however cases in which such rings have been observed. We should note though that current belief is that higher order rings can be produced if the gravitational lens is a black hole, but not from a galaxy or any other gravitational field which is bound to be weaker.

3.3.2 Numerical results

We wish to examine how a Schwarzschild and a Skyrme black hole can be distinguished through gravitational lensing phenomena. This is not something trivial as from a point outwards black holes with the same ADM mass will have identical spacetimes. So, we should see up to which distances the difference in the spacetimes is something that affects gravitational lensing. At some points we might refer to D_d as x_{obs} and to D_{ds} as x_s, which is our dimensionless notation.

We start by examining Einstein rings. In order to do this we take the observer at some fixed position from the black hole and compute the angular radius of the Einstein ring θ_E of a source placed behind the black hole and obviously on the optical axis. In Figure 3.8 this is done for some possible positions of the observer x_{obs}, for each one of which we examine a wide range of positions for the source x_s. The positions of the observer that we have considered here are really close to the black hole, the smallest one being on the innermost circular orbit of the Schwarzschild black hole. Though these positions are not useful from an observational point of view, they help us put some solid ground behind the importance of this study. We should also highlight that for such small distances the lens equation is not a good ally, as it does not hold. So, we solved the full geodesics problem to produce Figure 3.8.

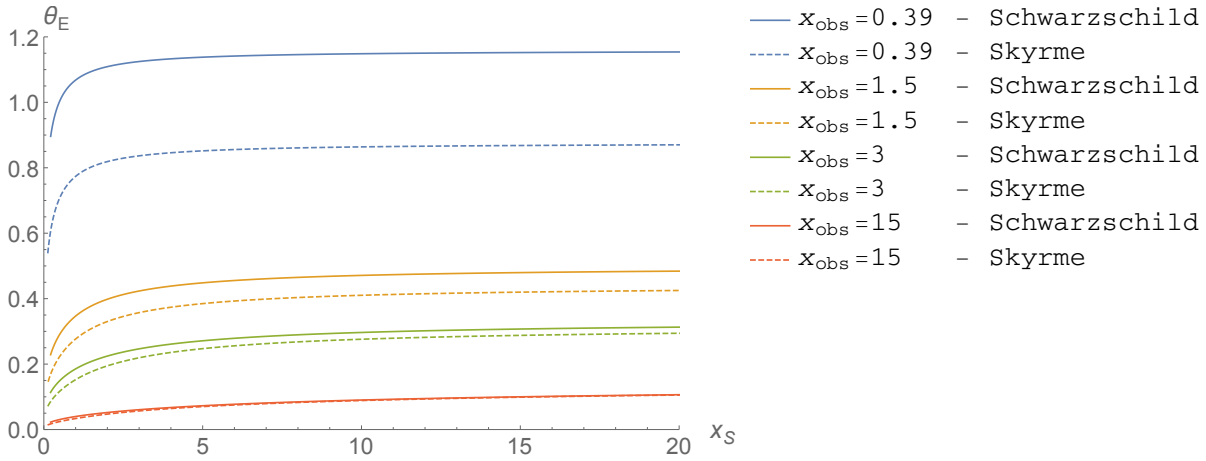

Figure 3.8: Einstein angular radii θ_E vs lens-source distance x_s for 4 different observer-lens distances x_{obs}. Those have been produced for two black hole models characterized by $(\alpha, \beta, x_h) = (0, 0, 0.13)$ and $(\alpha, \beta, x_h) = (0.005, 0, 0.077)$. They are denoted as Schwarzschild and Skyrme respectively and both have mass $m_{ADM} = 0.065$.

It is evident through the figure that the angular radii of the Einstein rings formed due to the presence of each black hole are different. One can understand this by thinking that in the case of the Skyrme black hole the photons pass by the black hole at a distance which is close enough to resolve that the spacetime is different than the corresponding Schwarzschild one. As the source is moved towards larger distances the Einstein angular radius approaches a value for each black hole model and observer position. The difference in this limiting value changes as we move the observer further away from the black hole.

Figure 3.8 raises two issues. First of all, it is evident that a disambiguity in either the mass of the black hole or the distance from the black hole to the observer could lead us to the wrong conclusions. We could interpret the observed θ_E through some analysis which involves a Schwarzschild black hole and obtain results that are incorrect. Secondly, up to which distances are such differences in θ_E present in Einstein rings data. If we found out that the distances D_d up to which such differences are present in the spectrum are smaller than any reasonable distances that we encounter in real life, then we should not be worried about them and disregard gravitational lensing as one of the tools that could help us resolve the question of whether a static and spherically symmetric black hole is

Skyrme or not.

In order to answer the second issue raised here, we adopt the following reasoning. Since the differences in θ_E come through the fact that photons approach the black hole enough to feel the hair, we set a limiting radius outside of which the spacetimes of the models under consideration here are identical. That we take to be $x_{lr} = 10$, supported by our numerical analysis and Figures 3.1 - 3.2. We then examine where would a photon coming practically from infinity converge, if its closest approach to the black hole was equal to that limiting radius, namely $x_{min} = x_{lr}$.

Since we are unaware of the distance x_{obs} that will emerge out of this analysis, even though one could make an estimate, we again solve the full geodesics problem. We find that the distance for which the closest approach a photon makes to the black hole is equal to x_{lr} is $x_{obs} = 6157\ m_{ADM}$. Solving the geodesics for both black holes with the same initial conditions verifies that the photon moves in exactly the same way for both models.

Thus, we can state that for the models considered up to this point in this study, distances of the order $5 \times 10^3\ m_{ADM}$ are the limit up to which gravitational lensing can be used to distinguish between a Schwarzschild and a Skyrme black hole. Such distances are really small in astronomical terms and thus the collinear case of gravitational lensing cannot be considered as a prominent mean of studying black hole hair in our case.

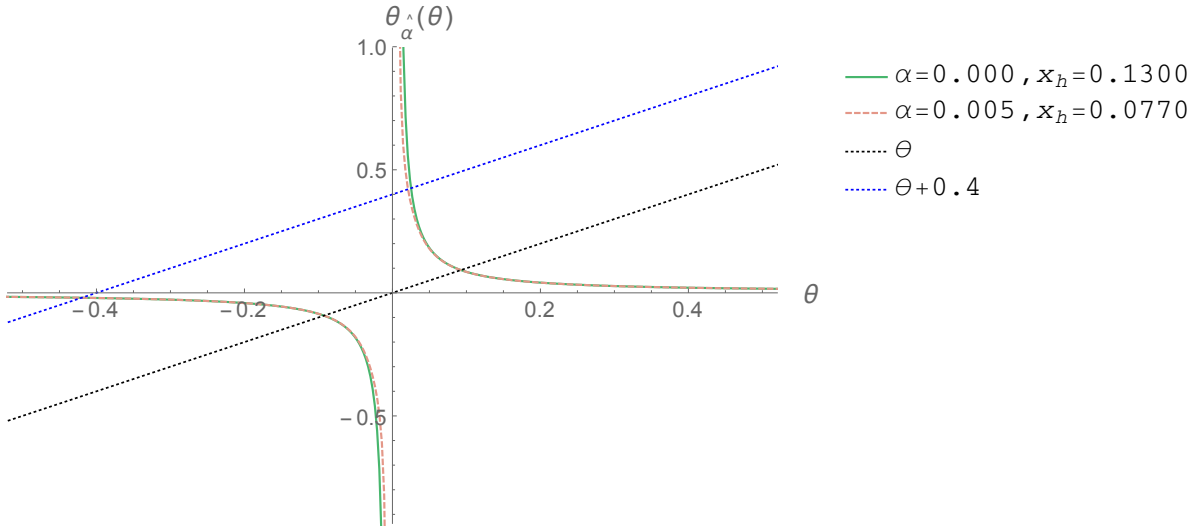

Figure 3.9: $\theta_{\hat{\boldsymbol{\alpha}}}(\boldsymbol{\theta}), -\theta_{\hat{\boldsymbol{\alpha}}}(\boldsymbol{\theta})$ vs $\boldsymbol{\theta}$ diagram for the 2 models under consideration. The parameters here are taken as $D_{ds} = 10^{10}\ m_{ADM}$ and $D_d = 5 \times 10^2\ m_{ADM}$. We have also plotted the function $\boldsymbol{\theta}$ and $\boldsymbol{\theta} + 0.4$. The points where those functions intersect $\theta_{\hat{\boldsymbol{\alpha}}}(\boldsymbol{\theta})$ and $-\theta_{\hat{\boldsymbol{\alpha}}}(\boldsymbol{\theta})$ are the solutions to the lens equation. Angles are in rad.

However, keep in mind that up to now we have considered the collinear case. One should also investigate the case where the source does not lie on the optical axis. The reason for that is that if one drops the collinearity condition the following picture emerges. The light rays moving on the one side of the lens follow different paths than those on the other side of the lens. So, even though on the side towards which the source is displaced the rays might move far enough from the black hole to be able to feel the difference in the spacetime originating from the hair, the ones moving from the other side might actually

feel the hair simply because they have to come closer to the black hole in order to be converged on the observer.

This reasoning is presented in Figure 3.9. There the lens equation approach is adopted. Specifically, if we take a look at Eq. (3.29) we can define

$$\theta_{\hat{\boldsymbol{\alpha}}}(\boldsymbol{\theta}) = \sin^{-1}\left(\frac{D_{ds}}{D_S}\sin\left(\hat{\boldsymbol{\alpha}}(x_{min})\right)\right) \tag{3.35}$$

where the dependence on θ comes through the impact parameter as

$$\sin\boldsymbol{\theta} = \frac{b}{D_d}, \tag{3.36}$$

where for $e = 1$ one has

$$b = x_{min}\sqrt{\frac{1}{N^2(x_{min})h(x_{min})}}, \tag{3.37}$$

as proven e.g. in [55].

The lens equation takes now the form

$$\boldsymbol{\theta} - \boldsymbol{\beta} = \theta_{\hat{\boldsymbol{\alpha}}}, \tag{3.38}$$

which has to be solved numerically. In Figure 3.9 we present $\theta_{\hat{\boldsymbol{\alpha}}}(\boldsymbol{\theta})$ as well as $\boldsymbol{\theta}$ for the configurations and distances stated in the caption, so that one can have a better, graphical understanding of this. A nice paper which applies this concept on a case with analytical metric functions is [69].

Table 3.3: Angular separations for the images produced by both models and geometrical parameters $D_{ds} = 10^{10}\ m_{ADM}$, $D_d = 6157\ m_{ADM}$ for the collinear and a non-collinear case.

Model (α, β, x_h)	Same side as source $\boldsymbol{\theta}$(arcsecs)	$\boldsymbol{\beta}$(arcsecs)	Opposite side than source $\boldsymbol{\theta}$(arcsecs)
$(0, 0, 0.13)$	5310.49	0	5310.49
$(0, 0, 0.13)$	5340.3	60	5280.86
$(0.005, 0, 0.077)$	5310.49	0	5310.49
$(0.005, 0, 0.077)$	5340.3	60	5280.86

Our point about the non-collinear case becomes evident if one looks at the $\boldsymbol{\theta} + 0.4$ line and the points at which it intersects $\theta_{\hat{\boldsymbol{\alpha}}}(\boldsymbol{\theta})$ and $-\theta_{\hat{\boldsymbol{\alpha}}}(\boldsymbol{\theta})$. One automatically sees that for $\boldsymbol{\beta} = -0.4$ the angular separations at which the 2 images of the source can be found on the sky are not the same. For the rays which travel on the same side of the optical axis as the displacement of the source the lens equation solution is identical for both black holes. For those travelling on the other side we can see that they are not. Keep in mind that $\boldsymbol{\beta} = -0.4$ is terribly large for an angular separation, but we picked it only for the difference to be obvious in this scale. In general large displacements are not prominent

for observation as they are not favoured by the geometry of the system. The intensity of those rays would significantly drop as not that many photons would undergo such a "trip". This is something that could also be checked numerically.

Having discussed how $\boldsymbol{\beta} \neq 0$ could perhaps help in observing the effects of the hair through a gravitational lensing phenomenon, we turn our attention to our case. We wish to see if physical values for $\boldsymbol{\beta}$ can make any difference in the case where $x_{obs} = 6157\ m_{ADM}$, where the $\boldsymbol{\beta} = 0$ geometry is unable to help us resolve the hair. If taking $\boldsymbol{\beta} \neq 0$ proves helpful then one should investigate up to which distances it continues to be so. If not, then the case of gravitational lensing for static and spherically symmetric Skyrmion black holes is closed.

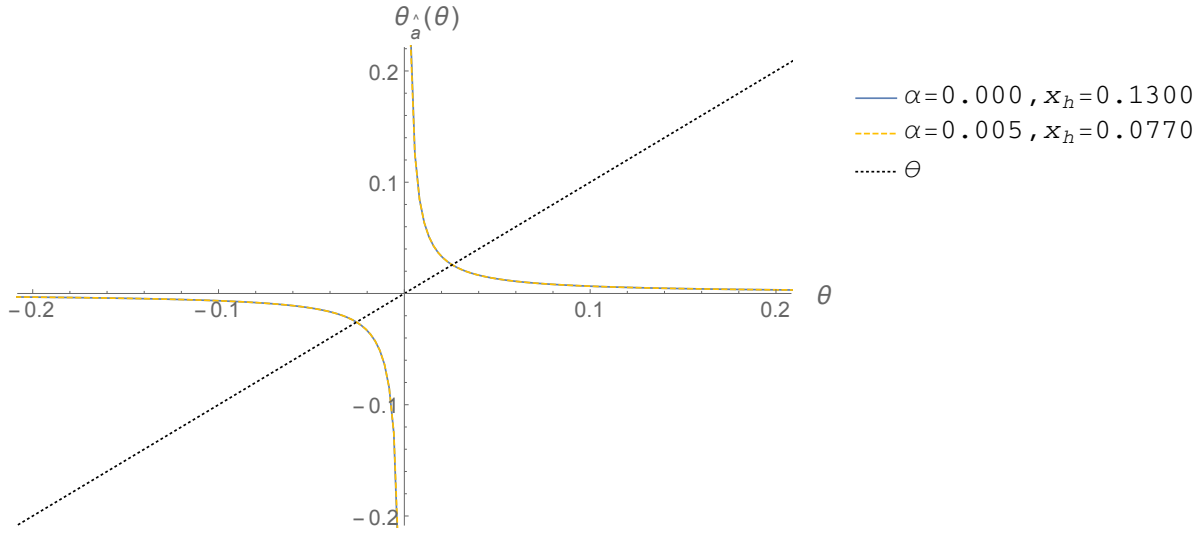

Figure 3.10: $\theta_{\hat{\boldsymbol{\alpha}}}(\boldsymbol{\theta}), -\theta_{\hat{\boldsymbol{\alpha}}}(\boldsymbol{\theta})$ vs $\boldsymbol{\theta}$ diagram for the 2 models under consideration. The parameters here are taken as $D_{ds} = 10^{10}\ m_{ADM}$ and $D_d = 6157\ m_{ADM}$. We have also plotted the function $\boldsymbol{\theta}$. The points where this function intersects $\theta_{\hat{\boldsymbol{\alpha}}}(\boldsymbol{\theta})$ and $-\theta_{\hat{\boldsymbol{\alpha}}}(\boldsymbol{\theta})$ are the solutions to the lens equation. Angles are in rad.

The solution to the lens equation for $D_{ds} = 10^{10}\ m_{ADM}$ and $D_d = 6157\ m_{ADM}$ can be found in Table 3.3. There we examine two cases. The case $\boldsymbol{\beta} = 0$ and the case $\boldsymbol{\beta} = 60''$. The choice of $\boldsymbol{\beta} = 60$ was made in the following sense. The angular separations observed are in general very small and specifically $< 30''$. But this number refers to the observer and the source lying at large distances from the source and in general with $D_{ds} \approx D_d$. In our case, D_{ds} is rather physical but $D_d << D_{ds}$. So, we should double those angular separations observed. As an upper limit, which however is logical, one can take $\boldsymbol{\beta} = 60''$.

As it can be seen in the table, indeed for this distance of the observer from the lens, the results obtained verify our previous conclusion. Namely, the Einstein rings for both black hole models turn out to be the same. If one then examines how those angular separations are altered by taking $\boldsymbol{\beta} = 60''$, he finds that the differences obtained are practically non-existent, as up to the point of our resolution abilities the angles are identical. As the non-collinear case does not improve our observational chances, even for this distance, we can disregard the possibility that it will provide us with observable differences in larger distances.

In Figure 3.10 one can see the graphical solution to the lens equation for $\boldsymbol{\beta} = 0$. For both black hole models, $\theta_{\hat{\boldsymbol{\alpha}}}(\boldsymbol{\theta})$ is shown. The scale is not optimal in order to pinpoint the solutions, but by comparing to Figure 3.9 one can see that even for very large values of $\boldsymbol{\beta}$, there are not very significant differences in $\theta_{\hat{\boldsymbol{\alpha}}}(\boldsymbol{\theta})$ between the models.

Based on our considerations, one can conclude, that in the case of favoured geometries, gravitational lensing phenomena are not helpful in identifying the presence of hair. As a gravitational lens, for the vast majority of physical scenarios, a static and spherically symmetric black hole will behave exactly as a Schwarzschild black hole of the same mass.

Finally let us note that the analysis of this chapter indicates that an observation of the shadow of a Skyrmion black hole is much more prominent to help us make out the presence of the hair than some gravitational lensing phenomena, where for realistic geometries Skyrmion black holes would appear as Schwarzschild ones.

Chapter 4

Scalar field scattering and absorption

In the previous chapter we focused on photons as a probe. However, one can have other probes as well. The behaviour of the black hole with respect to all of them builds its observational profile and enables us to infer its characteristics and properties. Typical probes are the scalar field, the electromagnetic field and gravitational waves. Essentially, fields of different spin. In this chapter we focus on the scalar field and we investigate how massless scalar fields are scattered and absorbed by Skyrmion black holes. We then extend both the scattering, as well as the absorption results to the massive case. A quite general and complete read on the topic is [70].

4.1 Probe field

In the following sections we develop the theory of scalar field scattering by black holes. Initially, we produce the differential equation describing the propagation of the scalar field. We then discuss the basics of scattering theory. Afterwards, we describe how to solve the differential equation. Finally, we present and discuss our results for both the massless and the massive case.

4.1.1 Lagrangian and DE

We wish to study classical cross sections of a scalar field Φ by a Skyrmion black hole and compare them to those produced by a Schwarzschild black hole of the same ADM mass. We focus on a minimally coupled scalar field. That is we take the standard real massive scalar field lagrangian and we make all contractions with respect to the metric $g_{\mu\nu}$. No direct interaction of non-gravitational nature between the scalar field and the hair is considered, even though such a study would be rather interesting.

The propagation of the probe field Φ is described by the wave equation in the curved background

$$\left(\Box_g + \frac{m_\phi^2}{\hbar^2}\right)\Phi = 0, \tag{4.1}$$

where $\Box_g$ is the d'Alambertian with respect to the metric $g_{\mu\nu}$ and m_ϕ the mass of the probe field. Based on the fact that $m_\phi << m_{ADM}$, we take no backreaction from the scalar field to the spacetime into account.

The standard way to solve such equations is the separation method, implemented by plugging in an expansion of the form

$$\Phi = \frac{A(r)}{r} Y_{lm}(\theta, \phi) e^{-iWt}. \tag{4.2}$$

Here $A(r)$ is simply a function with radial dependence, W the frequency of the scalar field and $Y_{lm}(\theta, \phi)$ the spherical harmonics having their roots in the spherical symmetry of the problem. Again, due to the spherical symmetry of the problem we cannot have any azimuthal dependence and so $m = 0$. Note that for each value of l we obtain a different solution for $A(r)$.

If we perform the necessary algebra[1], we can obtain the radial part of the differential equation. It reads

$$\partial^2_{x\star} A(x) + \left(w^2 - V_{eff}(x)\right) A(x) = 0, \tag{4.3}$$

where

$$\partial_{x\star} = N(x)h(x)\partial_x, \tag{4.4}$$

$$V_{eff}(x) = h(x)\left[N^2(x)\frac{l(l+1)}{x^2} + \frac{N(x)}{x}\partial_x\Big(N(x)h(x)\Big) + N^2(x)\beta^2_\phi\right] \tag{4.5}$$

and

$$\beta_\phi = \frac{m_\phi}{\hbar e F_\pi} \tag{4.6}$$

a dimensionless parameter directly related to the mass of the probe field. Note furthermore that $w = W(eF_\pi)^{-1}$ is the dimensionless frequency.

In order to get a better insight of the differential equation, we have to cast it into its standard form, namely account for the dispersion relation and write the equation down with respect to the field's velocity. It then reads

$$-\partial^2_{x\star} A(x) + V^\star_{eff}(x) A(x) = w^2 \upsilon^2 A(x), \tag{4.7}$$

where now the effective potential $V^\star_{eff}(x)$ reads

$$V^\star_{eff}(x) = h(x)\left[N^2(x)\frac{l(l+1)}{x^2} + \frac{N(x)}{x}\partial_x\Big(N(x)h(x)\Big)\right] + \left(h(x)N^2(x) - 1\right)\beta^2_\phi, \tag{4.8}$$

while on the right hand side we have employed the dispersion relation

$$\upsilon = \sqrt{1 - \frac{\beta^2_\phi}{w^2}}, \tag{4.9}$$

υ being the velocity of the massive field.

[1]Note that the d'Alambert operator is given by $\Box_g = g^{\mu\nu}\nabla_\mu\nabla_\nu$, where ∇_μ is the covariant derivative. Thus, one should be careful as Φ may be a scalar, but $\nabla_\mu\Phi$ is a vector. As a result

$$\Box_g\Phi = g^{\mu\nu}\nabla_\mu\nabla_\nu\Phi = g^{\mu\nu}\nabla_\mu\partial_\nu\Phi = g^{\mu\nu}\left(\partial_\mu\partial_\nu\Phi - \Gamma^\alpha{}_{\nu\mu}(\partial_\alpha\Phi)\right),$$

where $\Gamma^\alpha{}_{\nu\mu}$ are the Christoffel symbols.

In our new notation, the equation now appears to be Schrödinger-like, so the problem can be seen as a standard scattering problem of quantum mechanics. Namely, standard means of scattering theory as applied in quantum mechanics can be adopted here as well. Here, $V^{\star}_{eff}(x)$ plays the role of the quantum mechanical potential, while $w^2\upsilon^2$ that of the energy eigenvalue.

We should highlight that precisely because the problem is formulated as a quantum mechanics problem, one can look at $V^{\star}_{eff}(x)$ for the effective potential that the probe field feels. Thus all results can be cross checked with the corresponding effective potential. This can be rather helpful in understanding the effect of mass in the problem.

4.1.2 Scattering theory

Let us now direct our attention to scattering amplitudes and absorption cross sections. In order to obtain them we perform a partial wave analysis as per most cases in quantum mechanical problems. The method described here is presented in depth in [71].

Looking at the potential V_{eff} in Eq. (4.5) we notice that

$$V_{eff} \to \beta_{\phi}^2 \quad \text{as} \quad x^{\star} \to \infty, \tag{4.10}$$

$$V_{eff} \to 0 \quad \text{as} \quad x^{\star} \to -\infty \ \ (x \to x_h). \tag{4.11}$$

We can thus write down the asymptotic solutions of Eq. (4.3) as

$$A(x^{\star}) = \begin{cases} A^{(1)}_{wl} e^{-iw\upsilon x^{\star}} + A^{(2)}_{wl} e^{iw\upsilon x^{\star}} & , x^{\star} \to \infty \\ A^{(3)}_{wl} e^{-iwx^{\star}} & , x^{\star} \to -\infty \end{cases}, \tag{4.12}$$

which represents a purely ingoing mode at the horizon. The conservation of flux here implies that $|A^{(1)}_{wl}|^2 = |A^{(2)}_{wl}|^2 + \frac{1}{\upsilon}|A^{(3)}_{wl}|^2$.

In order to obtain the scattering amplitudes and the absorption cross section we impose an asymptotic scattering boundary condition. We wish for the total field at spatial infinity to be the sum of a plane wave plus an outgoing scattered wave. In other words, it should hold

$$\Phi(t, x, \theta, \phi) \sim e^{-iwt}\Phi_{\text{plane}}(x, \theta) + \frac{e^{-iwt}}{x} f(\theta) e^{iw\upsilon x^{\star}}. \tag{4.13}$$

At this point we should substitute the expansion for the plane wave. However, in a curved spacetime this is not the same as in Minkowski spacetime. Essentially, when we have a long range scattering field, plane waves are altered even at infinity. In our case, we indeed have such a field, the gravitational field. It has been shown that the long range character of the gravitational field can be accounted by a logarithmic phase modification of the exponentials [72, 73]. In practice, one has only to substitute $x \to x^{\star}$ in all the exponentials and the rest of the expressions remain the same as in Minkowski spacetime. Thus, if we take the plane wave to propagate along the z-axis it reads

$$\Phi_{\text{plane}}(x, \theta) = e^{iw\upsilon x^{\star}\cos\theta} = \sum_{l=0}^{\infty} (2l+1) i^l j_l(w\upsilon x^{\star}), \tag{4.14}$$

where j_l is the spherical Bessel function and $P_l(\cos\theta) = Y_{l0}(\theta)$ the Legendre polynomial of order l.

If one now takes the asymptotic behaviour of the Bessel function into account and plugs it into Eq. (4.14) he obtains

$$\Phi_{\text{plane}}(x,\theta) = -\frac{1}{2iwvx}\sum_{l=0}^{\infty}(2l+1)i^l\left(e^{-i(wvx^\star-l\pi/2)} - e^{i(wvx^\star-l\pi/2)}\right)P_l(\cos\theta). \tag{4.15}$$

Since the flux is conserved, scattering can only change the solution by a phase. Thus, the physical solution at infinity should look like

$$\begin{aligned}\Phi(t,x,\theta,\phi) &= -\frac{e^{-iwt}}{2iwvx}\sum_{l=0}^{\infty}(2l+1)i^l\left(e^{-i(wvx^\star-l\pi/2)} - e^{2i\delta_l(w)}e^{i(wvx^\star-l\pi/2)}\right)P_l(\cos\theta)\\ &= \frac{e^{-iwt}}{wvx}\sum_{l=0}^{\infty}(2l+1)i^l\sin\Big(wvx - l\pi/2 + \delta_l(w)\Big)e^{i\delta_l(w)}P_l(\cos\theta)\end{aligned} \tag{4.16}$$

If one now compares equations (4.13) with (4.16), taking (4.15) into account, he can extract the explicit expression for $f(\theta)$. It reads

$$f(\theta) = \frac{1}{2iwv}\sum_{l=0}^{\infty}(2l+1)\left(e^{2i\delta_l(w)} - 1\right)P_l(\cos\theta). \tag{4.17}$$

The phase shifts $e^{2i\delta_l(w)}$ can be expressed in our terminology if one checks how the solution at infinity is written in our language. This requires substituting the solution for $x^\star \to \infty$ found in (4.12) into the general solution, which is a weighted summation over l of Eq. (4.2). A direct comparison with Eq. (4.16) then leads to

$$e^{2i\delta_l(w)} = (-1)^{l+1}\frac{A^{(2)}_{wl}}{A^{(1)}_{wl}}, \tag{4.18}$$

which is how the phase shifts can be computed in our case.

Now, as in the quantum mechanical scattering, the differential scattering cross section can be obtained as

$$\frac{d\sigma}{d\Omega} = |f(\theta)|^2, \tag{4.19}$$

while partial absorption cross sections are computed as

$$\sigma_l = \frac{\pi(2l+1)}{w^2v^2}\left(1 - \left|\frac{A^{(2)}_{wl}}{A^{(1)}_{wl}}\right|^2\right). \tag{4.20}$$

The total absorption then follows as

$$\sigma = \sum_{l=0}^{\infty}\sigma_l. \tag{4.21}$$

Finally, let us make the following observation. The differential scattering cross section is divergent at $\theta = 0$, as $P_l(\cos(0)) = P_l(1) = 1$ and it enters an infinite sum. In order to get around this problem, one can use the method of reduced series which was first

introduced in [74]. This method states that one needs only to take into account the summation up to some l_{max} and not ∞. This l_{max} can be found through trial and error, by examining how the behaviour changes when one takes more l's into account, up to the point where the differential cross section remains unaltered by the addition of larger l's. Then, one can make $f(\theta)$ less singular around $\theta = 0$ by multiplying it by a function that vanishes at $\theta = 0$. If the new function is then expanded in a series of Legendre polynomials, one can compute the new coefficients for the summation. Let us illustrate this by writing Eq. (4.17) as

$$2iwvf(\theta) = \sum_{l=0}^{\infty} a_l P_l(\cos\theta). \tag{4.22}$$

The m^{th} reduced series is then defined as

$$(1-\cos\theta)^m 2iwvf(\theta) = \sum_{l=0}^{\infty} a_l^{(m)} P_l(\cos\theta), \tag{4.23}$$

where the $a_l^{(m)}$'s can be computed through the recurrence relations for Legendre polynomials and turn out to be

$$a_l^{(i+1)} = a_l^{(i)} - \frac{l+1}{2l+3} a_{l+1}^{(i)} - \frac{l}{2l-1} a_{l-1}^{(i)}. \tag{4.24}$$

By performing a few iterations[2] the new coefficients $a_l^{(m)}$ are computed and they can be used to compute the differential scattering cross section, avoiding running into singularities[3].

4.1.3 Numerical approach

4.1.3.1 Way 1

In order to obtain the data needed to compute scattering differential cross sections and absorption cross sections one needs to solve Eq. (4.3). The standard way to do this is to use Eq. (4.12) at $x^\star \to -\infty$ ($x \to x_h$) as an initial condition in order to integrate the differential equation up to a very large distance. Since two initial conditions are required one matches both the asymptotic expansion, as well as its derivative at $x^\star \to -\infty$. Since solutions can be multiplied by an arbitrary factor, one can set $A_{wl}^{(3)} = 1$ or any other value he wishes. However, keep in mind that by doing so, the flux condition changes. For example, for $A_{wl}^{(3)} = 1$ it reads $|A_{wl}^{(1)}|^2 = |A_{wl}^{(2)}|^2 + \frac{1}{v}$.

Having integrated the solution up to a large distance from the black hole[4], the numerical solution should be matched to the asymptotic solution at $x^\star \to \infty$. The coefficients

[2] Usually $m = 2$ or $m = 3$ suffices.

[3] Keep in mind that after each iteration we are left with one less a_l because of the presence of the $a_{l+1}^{(i)}$ term in the recurrence relation. Furthermore, the careful reader might have noticed that for $l = 0$ one is faced with the problem of which is the value of $a_{-1}^{(i)}$ to be plugged into Eq. (4.24). This is dealt with by noticing that one could think of the summation as running over all integers and having $a_l = 0$ for $l < 0$.

[4] A more precise explanation of what "large distance" means is the following. One can substitute the asymptotic solution into (4.3). Then on the left hand side a function of $x^\star$ appears, while on the right hand side we have that it equals 0. By trying values of $x^\star$ one can find out at which distances the deviation of the left hand side from 0 becomes as small as one wishes. This is a measure of the accuracy of the asymptotic solution.

$A^{(1)}_{wl}$, $A^{(2)}_{wl} = 1$ are determined through this matching. Plugging them into Eq. (4.18) and (4.20) , the corresponding phase shifts and partial absorption cross sections are obtained. This process should be carried out for each l up to some l_{max} as described in the previous section.

A measure of the accuracy of the solution is the condition referring to the flux $|A^{(1)}_{wl}|^2 = |A^{(2)}_{wl}|^2 + \frac{1}{v}|A^{(3)}_{wl}|^2$. Having obtained all the coefficients one can plug them into the expressions and check whether it is satisfied. This is a check that the solution should be able to pass. Actually, one can take this a step further by noticing that the differential equation (4.3) is of the form

$$\frac{d^2A(x)}{dx^2} + U(x)A(x) = 0, \tag{4.25}$$

namely there are no first order derivatives. Such differential equations have a constant wronskian $W(A_1, A_2)$, where $A_1(x)$ and $A_2(x)$ are solutions of the differential equation. This is rather easy to derive as

$$\begin{aligned}\Big(W(A_1,A_2)\Big)' &= \Big(A_1(x)A_2'(x) - A_2(x)A_1'(x)\Big)' \\ &= A_1(x)A_2''(x) + A_1'(x)A_2'(x) - A_2'(x)A_1'(x) - A_2(x)A_1''(x) \\ &= -U(x)A_1(x)A_2(x) + U(x)A_1(x)A_2(x) \\ &= 0,\end{aligned} \tag{4.26}$$

where $' = \frac{d}{dx}$ and in the penultimate line we made use of (4.25).

This result can be used to derive the flux condition by plugging in the wronskian the asymptotic solutions at $x^\star \to -\infty$ and $x^\star \to \infty$, alongside with their complex conjugates. Specifically

$$\begin{aligned}W\left(A^{(1)}_{wl}e^{-iwvx^\star} + A^{(2)}_{wl}e^{iwvx^\star}, \left(A^{(1)}_{wl}\right)^\star e^{iwvx^\star} + \left(A^{(2)}_{wl}\right)^\star e^{-iwvx^\star}\right) &= 2iwv\left(\left|A^{(1)}_{wl}\right|^2 - \left|A^{(2)}_{wl}\right|^2\right), \\ W\left(A^{(3)}_{wl}e^{-iwx^\star}, \left(A^{(3)}_{wl}\right)^\star e^{iwx^\star}\right) &= 2iw\left|A^{(3)}_{wl}\right|^2,\end{aligned} \tag{4.27}$$

which, when equated, lead to $|A^{(1)}_{wl}|^2 = |A^{(2)}_{wl}|^2 + \frac{1}{v}|A^{(3)}_{wl}|^2$. The standard way to derive this condition is by using the current corresponding to Φ.

An even stronger condition is that the wronskian has to remain constant $\forall x^\star \in (-\infty, \infty)$. This can be used to check the accuracy of the numerical solution at every point. Namely, though this check one can verify that the numerical integration went well or perhaps locate the point at which it exhibited an unexpected behaviour. These results can be applied to any method which involves numerically integrating a differential equation of this form.

The drawback of this method is that the solution to the differential equation is oscillating. Furthermore, as l increases, the amplitude of the oscillation increases as well. From the numerical point of view, this is not a preferable behaviour as numerical errors can easily be picked along the way. As a result one has to be cautious.

4.1.3.2 Way 2

A different way to tackle the problem, and the one we implemented, is described in [75]. There they redirect the solution of the problem from the study of the numerical solution to a direct study of the phases. The advantage of this approach is that even though the solution to the differential equation admits oscillatory behaviour, the phases do not.

The basis of their approach is a modified version of the simple Prüfer transformation [76, 77]. The differential equation we wish to solve is (4.3), while we have already examined the asymptotic behaviour of the potential. The asymptotic solutions can be written as (4.12) or equivalently as

$$A(x^\star) = \begin{cases} B\sin\left(w\upsilon x^\star + \zeta\right) & , x^\star \to \infty \\ e^{-iwx^\star} & , x^\star \to -\infty \end{cases}, \tag{4.28}$$

where B and ζ are complex constants.

A direct comparison of the asymptotic expansion at $x^\star \to \infty$ with (4.16) leads to the definition of the phase shifts in this language. We identify the phase shifts as

$$\delta_l(w) = \zeta + \frac{l\pi}{2}. \tag{4.29}$$

So, determining ζ is all we need to compute scattering differential cross sections and absorption cross sections.

We now introduce $P(x^\star)$ as the logarithmic derivative of $A(x^\star)$,

$$P(x^\star) = \frac{dA(x^\star)/dx^\star}{A(x^\star)}, \tag{4.30}$$

which at $x^\star \to -\infty$ obeys the boundary condition $P(x^\star) = -iw$.

In terms of P the exact solution to (4.3) reads

$$A(x^\star) = e^{\int P(x^\star)\, dx^\star}. \tag{4.31}$$

At the same time, $A(x^\star)$ and its derivative can be expressed through a Prüfer transformation as

$$A(x^\star) = B(x^\star)\sin\left(w\upsilon x^\star + \tilde{P}(x^\star)\right), \tag{4.32}$$

$$\frac{dA(x^\star)}{dx^\star} = B(x^\star)w\upsilon\cos\left(w\upsilon x^\star + \tilde{P}(x^\star)\right), \tag{4.33}$$

where $\tilde{P}(x^\star)$ is a Prüfer phase function for which it holds that $\tilde{P}(x^\star)\Big|_{x^\star\to\infty} = \zeta$.

Substituting (4.32) and (4.33) into (4.30) a relation between the two phase functions, P and $\tilde{P}$, can be found. The connection reads

$$\tilde{P}(x^\star) = -w\upsilon x^\star + \frac{1}{2i}\ln\left(\frac{iP(x^\star) - w\upsilon}{iP(x^\star) + w\upsilon}\right). \tag{4.34}$$

If one plugs (4.31) and then (4.32) into (4.3) he derives

$$\frac{dP(x^\star)}{dx^\star} + P^2(x^\star) + w^2 - V_{eff}(x^\star) = 0, \tag{4.35}$$

$$\frac{d\tilde{P}(x^\star)}{dx^\star} + \left[w\upsilon - \frac{w^2 - V_{eff}(x^\star)}{w\upsilon}\right]\sin^2\left(w\upsilon x^\star + \tilde{P}(x^\star)\right) = 0, \tag{4.36}$$

as the differential equations for determining $P(x^\star)$ and $\tilde{P}(x^\star)$ respectively.

Numerically solving any of those two equations will provide us with the phase shifts $\delta_l(w)$. There is however another issue that needs to be accounted. In problems of the form (4.3), small exponentials can be switched on along the solution of the differential equation. This is called the Stokes phenomenon. In order to deal with this behaviour, we numerically integrate (4.35) up to some point using $P(-\infty) = -iw$ as an initial condition and then we switch to the study of (4.36). We obtain an initial condition in order to kick off the integration through (4.34) and we numerically integrate up to some very large distance. We can then read off the value of ζ. The point at which the switch is made is crucial. Ideally, it should be done somewhere around the maximum of the black hole potential barrier, as this secures that we do not run into trouble. Essentially, we wish to avoid studying the same phase function throughout the entire potential barrier.

4.1.3.3 Glory scattering

The aforementioned methods can be used to study differential cross sections for scattering and absorption cross sections. The generality with which the potential is treated makes them rather powerful tools for every problem with the same setup. There is however an approximation that can be used for obtaining differential scattering cross sections in the case of the massless scalar field. It can only reproduce a limited number of peaks for a specific range of frequencies and at the same time it does not offer any kind of information about absorption. Its validity however has been checked in the case of a Skyrmion black hole [50] and it is a relatively easy and fast way to obtain partial answers to the scattering problem.

Let us begin by examining a high frequency plane wave. High frequency in this context means that the wavelength λ of the wave is small compared to the radius of curvature of the background geometry. Essentially, if the geometry varies over a characteristic distance L, then $\lambda << L$. Then as shown in [70, 78], one can approximate massless plane waves as moving along null geodesics. At the same time, there exist orbits where the incoming particle is scattered back into the incoming direction. This happens when the particle circles the black hole once or more times as seen e.g. in Figure 3.4a and is discussed in standard texts [27].

For these scattering angles, namely $\theta = \kappa\pi$ where $\kappa \in \mathbb{Z}$, we have a classical scattering phenomenon, known as glory scattering, which allows one to compute scattering cross sections. The same phenomenon appears in the black hole scattering case as well [79, 80, 81, 82]. Depending on whether the line of propagation remains the same or is inverted it is called a forward or backwards glory. Essentially it is a diffraction effect.

Combining these facts one can compute the scattering cross section for massless scalar waves with $w >> 1$ and for scattering angles $\theta \approx \pi$ by looking at null geodesics orbiting the black hole once and being deflected back at the initial direction from where they came from through the simple formula

$$\left(\frac{d\sigma}{d\Omega}\right)_{\theta\approx\pi} \approx 2\pi w b_g^2 \left|\frac{db}{d\theta}\right|_{\theta=\pi} J_0^2(w b_g \sin\theta), \tag{4.37}$$

where b_g is the dimensionless impact parameter of a geodesic moving once around the black hole and scattered back to the incoming direction and J_0 a Bessel function of the first kind.

This formula was initially proposed in [83] for the case of scalar waves and was then extended to arbitrary spins [84]. Cases where glory scattering is investigated and verified are [50, 75, 85]. In [85] one can also find an approximate relation for b as a function of θ, which in turn he can use to compute $db/d\theta$ as well. The results are quite accurate using this formula, but in our case we will be obtaining those numbers by directly solving the geodesics problem.

4.2 Numerical results

We will be applying the methodology of Section 4.1.3.2 in order to obtain differential scattering cross sections and absorption cross sections for the case of the massless scalar field. Our results on scattering cross sections are in agreement with those in [50], which we also extend to account for absorption as well. Then, the results obtained for the massless scalar field are extended to the case of the massive scalar field as well. Up to our knowledge, this has not been investigated for a Skyrmion black hole up to now.

4.2.1 Massless case

We wish to compare differential scattering cross sections and absorption cross sections of Schwarzschild and Skyrmion black holes for massless scalar field. In order to do this, we consider a Schwarzschild black hole $(\alpha, \beta, x_h) = (0, 0, 0.2166)$ and to Skyrmion black holes of the same ADM mass. We will name the two Skyrmion black holes CASE I $(\alpha, \beta, x_h) = (0.01, 0, 0.119)$ and CASE II $(\alpha, \beta, x_h) = (0.01, 0.5, 0.116)$. These three configurations allow us to find out the impact of both α as well as β in the final outcome.

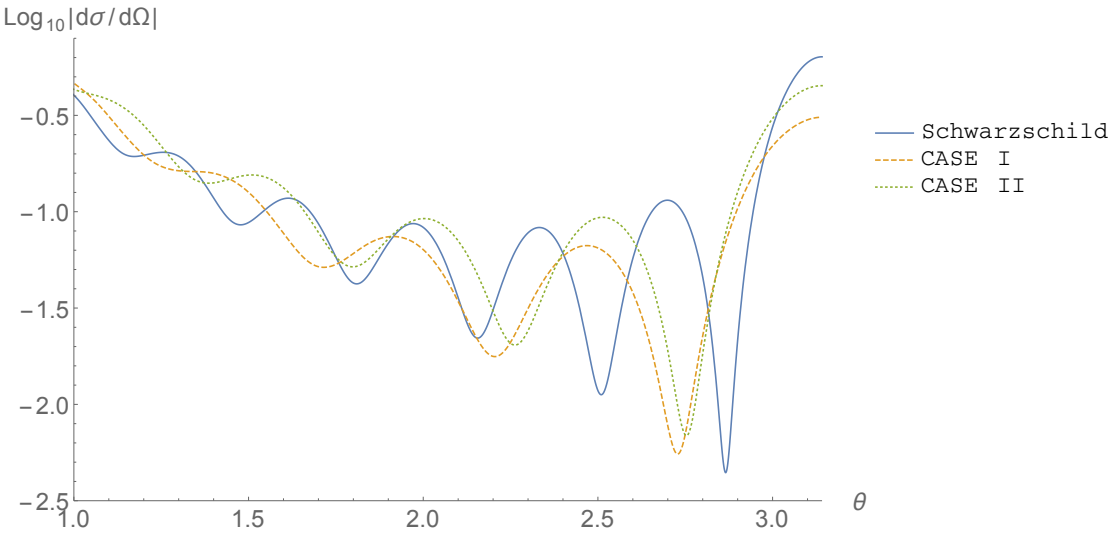

Figure 4.1: Differential scattering cross section of a scalar field with frequency $w = 15$. The scatterers are a Schwarzschild $(\alpha, \beta, x_h) = (0, 0, 0.2166)$ and two Skyrmion black holes named CASE I $(\alpha, \beta, x_h) = (0.01, 0, 0.119)$ and CASE II $(\alpha, \beta, x_h) = (0.01, 0.5, 0.116)$. All have $m_{ADM} = 0.1083$.

We plot the differential scattering cross sections obtained for all three models in Figure 4.1 for a scalar field of frequency $w = 15$. The following observations can be made. The scattering peaks in the case of the Skyrmion black holes are moved towards smaller scattering angles. This can be understood in the sense that in the Skyrmion black holes case, the central black hole is smaller compared to the Schwarzschild one under examination here. But for two Schwarzschild black holes of masses $M_1 < M_2$, the peaks for M_1 appear at smaller angles as it can be seen in Figure 4.2, where two Schwarzschild black holes with masses $m_{ADM,1} = 0.1083$ and $m_{ADM,2} = 0.0783$ are compared under the same scattering experiment.

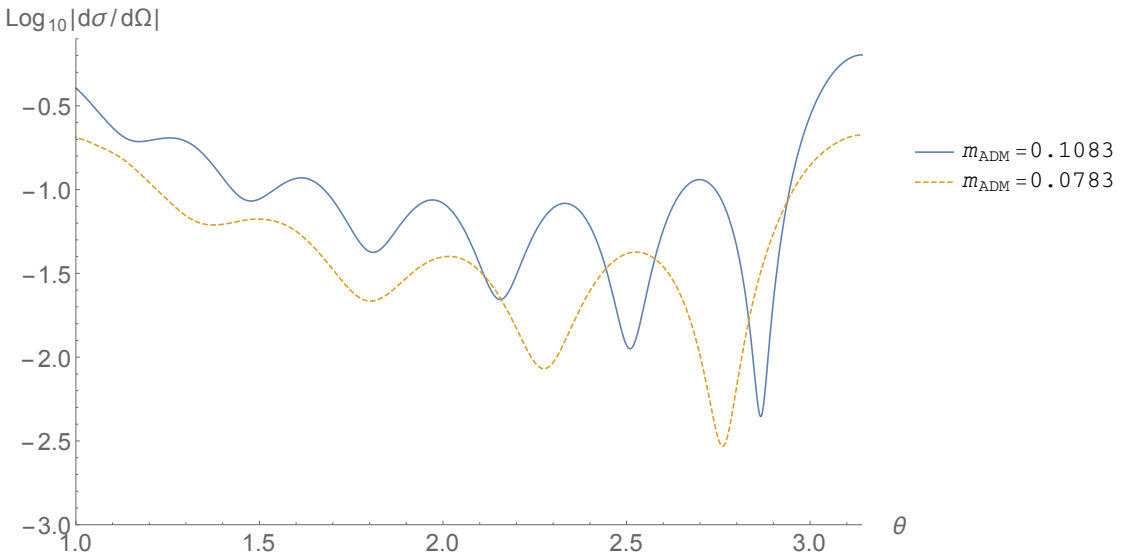

Figure 4.2: Differential scattering cross section of a scalar field with frequency $w = 15$. The scatterers are two Schwarzschild black holes of masses $m_{ADM,1} = 0.1083$ and $m_{ADM,2} = 0.0783$. The peaks for the smaller Schwarzschild black holes are moved towards smaller angles.

This result is not universal. Namely, simply the size of the central black hole cannot determine the order at which the characteristic peaks will appear. If one makes a comparison between CASE I and CASE II, he will find out that even though CASE II has a smaller black hole lying at the centre, its peaks are met at larger angles. The crucial difference between those two models is that CASE I has a massless pion ($\beta = 0$), while this does not hold for CASE II ($\beta \neq 0$). One thus sees that the effect of the mass of the pion is quite strong in the spectrum of scattering experiments with scalar fields as probes. Specifically, they shift the scattering peaks towards larger values of the scattering angle. Its effect is so strong, that up to some point it can counteract differences in the size of the black hole surrounded by the skyrmion.

The aforementioned results hold for all the frequencies of the scalar field that were tested and which satisfied the condition that w is of the order of $1/x_h$. The case $w = 8$ can be found in Figure 4.3 as further proof. For these values of w one can view the scattering as some diffraction phenomenon, which would fade as w becomes smaller and smaller. The peaks in this picture can be interpreted as the angles at which the diffraction

maxima occur.

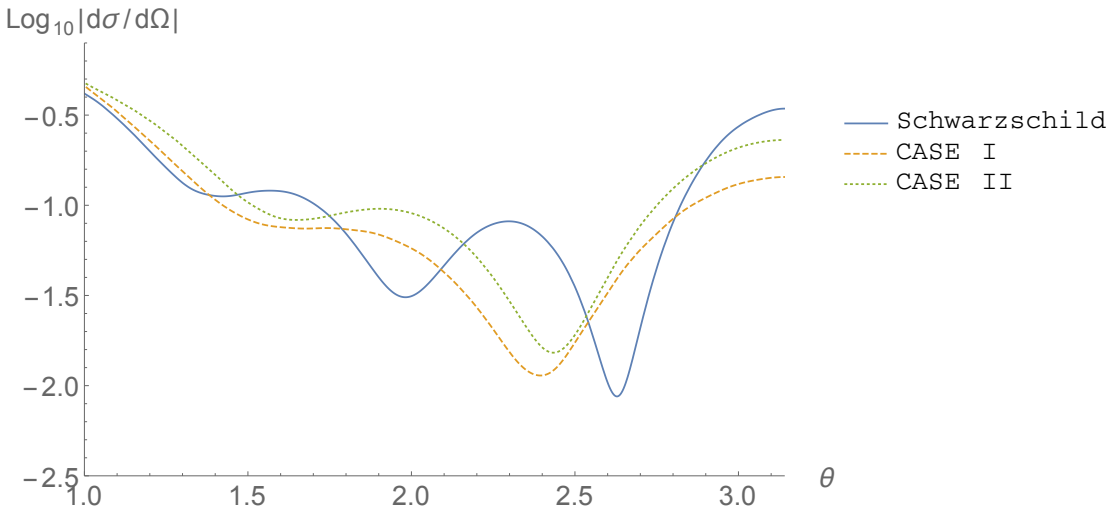

Figure 4.3: Differential scattering cross section of a scalar field with frequency $w = 8$. The scatterers are a Schwarzschild $(\alpha, \beta, x_h) = (0, 0, 0.2166)$ and two Skyrmion black holes named CASE I $(\alpha, \beta, x_h) = (0.01, 0, 0.119)$ and CASE II $(\alpha, \beta, x_h) = (0.01, 0.5, 0.116)$. All have $m_{ADM} = 0.1083$.

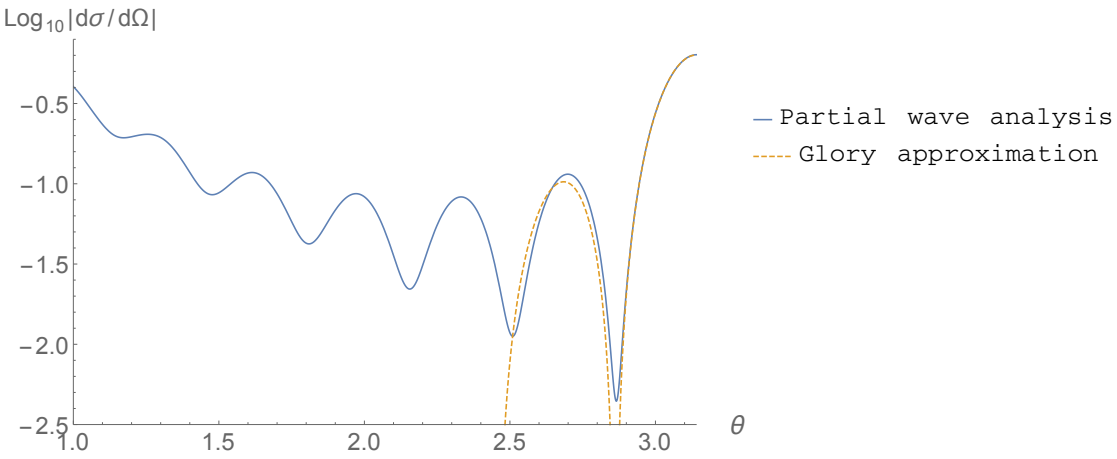

Figure 4.4: Differential scattering cross section of a scalar field with frequency $w = 15$ as obtained through a full partial wave analysis and the glory approximation. Clearly, the peaks near $\theta \approx \pi$ are in good agreement. The scatterer is a Schwarzschild black hole $(\alpha, \beta, x_h) = (0, 0, 0.2166)$.

Furthermore, let us also make a comment on the glory approximation presented in Section 4.1.3.3. What the glory approximation promises, is to reproduce the peaks appearing at scattering angles which are multipoles of π. In Figure 4.4 we present the differential cross section for a probe field of frequency $w = 15$ scattered by the Schwarzschild black hole with $(\alpha, \beta, x_h) = (0, 0, 0.2166)$. There the cross sections as obtained through the

full partial wave analysis and the glory approximation are presented. Indeed, there is a good agreement between the two methods for those peaks. This result holds also for the Skyrmion black holes.

At this point let us pause for a moment and try to understand the reason for which the differential scattering cross sections look as they do. Namely, why we get this pattern of maxima and minima at different angles. Let us temporarily think of the scalar field as a continuum of particles travelling in the plane and being scattered by the black hole. Then, at each scattering angle we have that the main contribution comes from two rays with different impact parameters, as seen in Figure 4.5. Those two rays follow different orbits and thus have a phase difference. Thus, at some scattering angles they will interfere constructively and in some others destructively. The values of the angle at which we have constructive interference are the maxima of the differential scattering cross section, while the minima correspond to the angles where destructive interference occurs. Since the two main orbits contributing to the scattering at a scattering angle $\theta = \pi$ follow symmetric trajectories due to the symmetry of the spacetime, we are bound to observe constructive interference at that angle, as we indeed do. This result does not hold for spacetimes which are not spherically symmetric, for example the Kerr black hole.

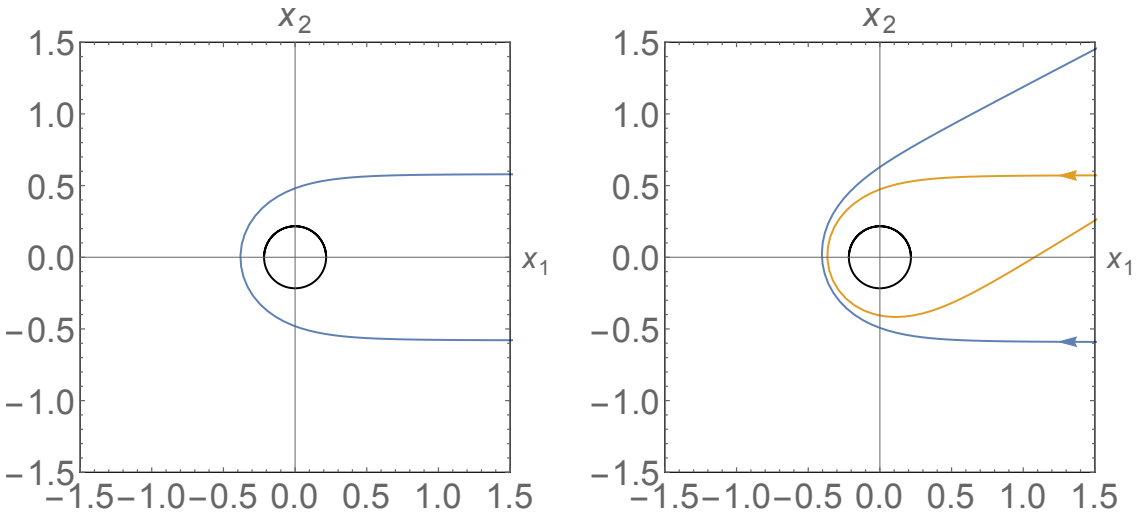

Figure 4.5: Null geodesics in the black hole spacetime. The black hole is denoted by the black circle. On the left, we have the symmetric case of rays being backscattered at the initial direction they came from. Due to the symmetry of the spacetime the two trajectories are symmetric. On the right, we show two rays with different impact parameters being scattered at the same direction. All rays are coming from infinity and we use arrows to indicate the direction along which they initially move.

We now turn our attention towards absorption cross sections. Initially, we wish to break down absorption to partial absorptions, so that we get a better understanding of the phenomenon. We then move on to perform a comparison between the three models as before.

In Figure 4.6, the partial absorption cross sections for the Schwarzschild black hole are

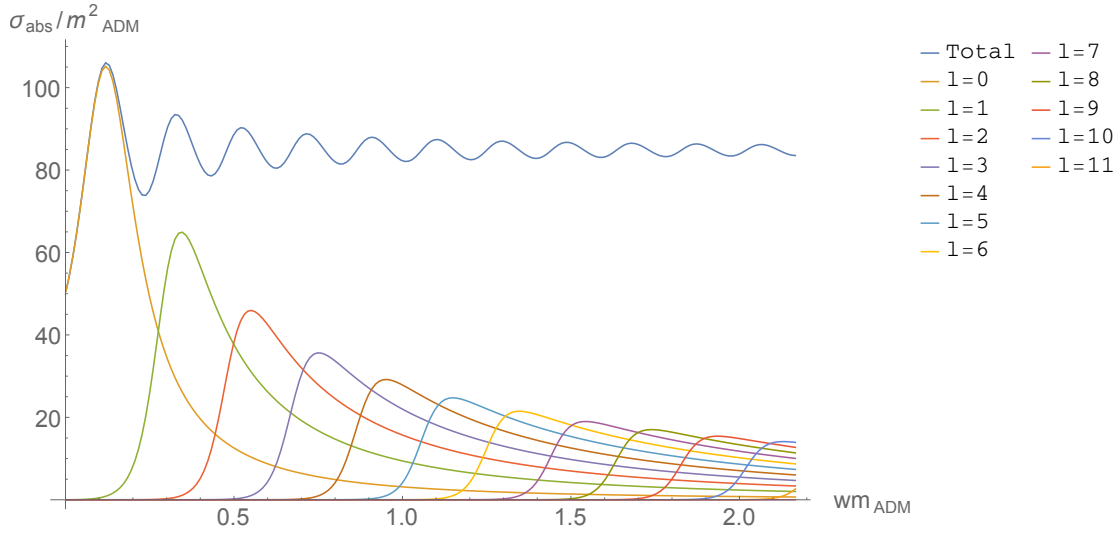

Figure 4.6: Partial and total absorption cross section of a scalar field with respect to its frequency. The absorber is a Schwarzschild $(\alpha, \beta, x_h) = (0, 0, 0.2166)$ black hole of $m_{ADM} = 0.1083$.

presented, alongside the total absorption cross section. The effective potential for each value of l is an efficient absorber around different values of the frequency of the scalar field w. Peaks appear each time one of those l's is switched on. However, we see that the amplitude of the peaks decreases as w becomes larger and larger. This can be understood in the sense that as w increases, the wavelength of the probe field decreases. When it becomes rather small compared to the radius of the black hole absorption essentially becomes constant, as they decouple. At the other end, for very small values of w, the wavelength of the scalar field becomes much larger than the radius of the black hole and thus absorption is very limited.

In the case of the Schwarzschild black hole one can actually quantify the above considerations. At the high energy limit the value of the absorption cross section approaches the geometrical optics value of $\sigma_{abs} = \pi b_c^2 = 27\pi m_{ADM}^2$. Thus, in our diagram it should approach the value $\sigma_{abs}/m_{ADM}^2 = 27\pi$ as w becomes rather large. This indeed happens. At the same time, the corresponding low energy limit is $\sigma_{abs} = 16\pi m_{ADM}^2$. Again, for small values of w we see that $\sigma_{abs}/m_{ADM}^2 = 16\pi$. The high energy result holds for probe fields of other spins as well. The same cannot be said for the low energy limit.

As a reminder keep in mind that for the Schwarzschild black hole $m_{AMD} = m_{BH}$, which is not true for the Skyrmion black holes. If one were to redraw the diagram with m_{BH} in the place of m_{AMD} in the y-axis, the low energy absorption limit is recovered for Skyrmion black holes as well. The high energy limit on the other side is not, as fields with small wavelength are better able to resolve the differences in the spacetime geometry.

Partial and total absorption cross sections are also presented for the CASE II Skyrmion black hole in 4.7. We observe that the same reasoning as before can be applied to understand the behaviour of the curve for the range of values w under investigation. A direct comparison of the partial absorptions with the Schwarzschild case reveals that for the

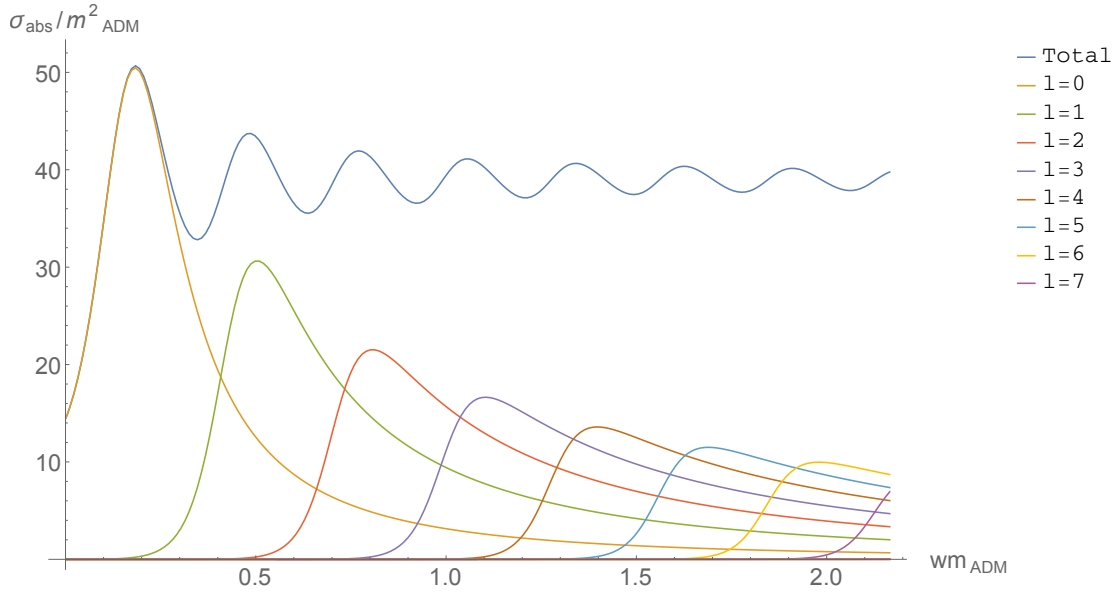

Figure 4.7: Partial and total absorption cross section of a scalar field with respect to its frequency. The absorber is the CASE II $(\alpha, \beta, x_h) = (0.01, 0.5, 0.116)$ Skyrmion black hole with $m_{ADM} = 0.1083$.

same values of w less values of l for the effective potential are stimulated.

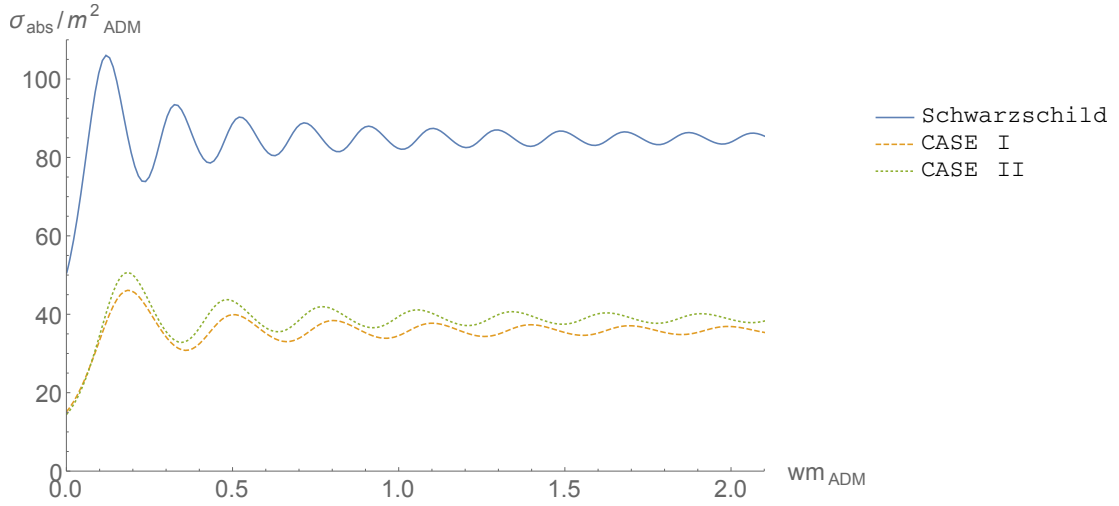

Figure 4.8: Total absorption cross section of a scalar field with respect to its frequency. The absorbers are a Schwarzschild $(\alpha, \beta, x_h) = (0, 0, 0.2166)$ and two Skyrmion black holes named CASE I $(\alpha, \beta, x_h) = (0.01, 0, 0.119)$ and CASE II $(\alpha, \beta, x_h) = (0.01, 0.5, 0.116)$. All have $m_{ADM} = 0.1083$.

The total absorption of the Schwarzschild black hole is compared with those of CASE I and CASE II in Figure 4.8 for a broad range of w. First of all, we notice that the

Schwarzschild black hole absorbs more than the corresponding Skyrmion black holes of the same ADM mass. Again, this can be put to perspective by thinking that a larger black hole is bound to absorb more on a mean scale. Furthermore, we see that absorption peaks in the case of the Skyrmion black holes are moved towards larger values of w. Once more, this is behaviour admitted by smaller Schwarzschild black holes. Finally, the peaks are more wide in the case of the Skyrmion black holes.

Note that once again, simply looking at the size of the actual black hole in each one of the configurations under investigation does not suffice to predict the results, not even at the qualitative level. The effect of the pion mass β can reverse the case and account for small differences in the radii of the black holes. Indeed, as in the scattering case, the absorption peaks for CASE II can be found at smaller values of w and absorption is higher as well.

4.2.2 Effect of mass

Having considered the massless scalar field as a probe, we wish to extend those results in the case of the massive scalar field as well. We will be changing the order in this case and we will study absorption first and then scattering. The motivation for that is that in order to understand our scattering results, we will need a better picture of the absorption.

Initially let us focus on the Schwarzschild black hole. Before we present our results on absorption cross sections let us examine the effect of β_ϕ on the effective potential V_{eff}. This can be seen in Figure 4.9, where the effective potential is drawn for different values of l and β_ϕ. We see that the effect of the mass of the probe field is that it lowers the height of the peak, when compared to the level of classically allowed motion. There, we plot the first three l's for $\beta_\phi = 0$ and $\beta_\phi = \beta_{\phi,crit,1} = 1.778$. The terminology $\beta_{\phi,crit,l}$ was introduced in [86] and refers to the value of β_ϕ for which the peak of V_{eff} for the respective l cannot play the value of a barrier any more. Increasing the value of β_ϕ decreases the height of the peaks of the effective potential with respect to the level of classically allowed motion, thus it should lead to higher absorption.

A better grasp of absorption comes through Figure 4.10. There the real part of the phase shifts $\mathrm{Re}(e^{2i\delta_l})$, alongside their imaginary part $\mathrm{Im}(e^{2i\delta_l})$ and their modulus are plotted against l. There we see that for small l's, δ_l has a positive imaginary part and thus $e^{2i\delta_l}$ is essentially zero. This indicates absorption from the black hole. As the value of l increases, δ_l becomes almost real and $e^{2i\delta_l}$ is oscillating. This figure can be read in parallel with Figure 4.6. One sees that the l's for which absorption is significant are those that have been switched on for a frequency $w = 15$.

Indeed, absorption behaves as we expected from the study of V_{eff}. This can be verified by looking at Figure 4.11, where absorption cross sections are presented for the Schwarzschild black hole and different values of the probe field mass β_ϕ. In general absorption is increased, while the characteristic peaks are moved towards higher frequencies as the value of β_ϕ is increased. Specifically for small values of the frequency the difference in the absorption is significant, since the effect of β_ϕ on the peaks of the effective potential for each l is more significant for small values of l. As we move towards higher frequencies on the other side, the higher l modes contribute to the absorption as well, and they are not affected significantly by the presence of the β_ϕ term, so at the limit of large frequencies absorption tend to coincide. Furthermore, notice that as predicted for $\beta_\phi = \beta_{\phi,crit,1}$, the

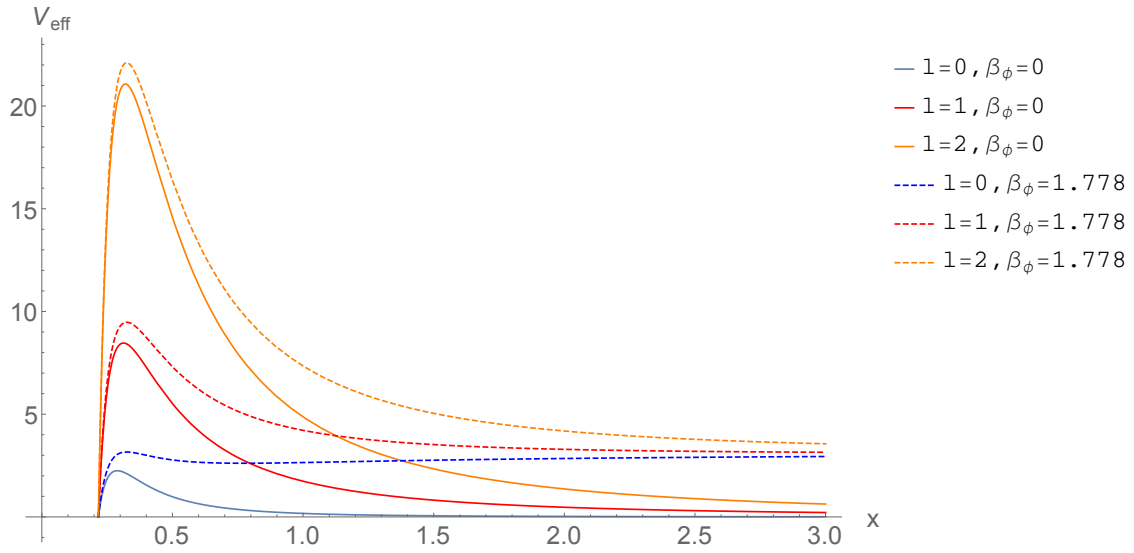

Figure 4.9: Effective potential for the Schwarzschild black hole $(\alpha, \beta, x_h) = (0, 0, 0.2166)$. The first three values of l are drawn for $\beta_\phi = 0$ and $\beta_\phi = \beta_{\phi,crit,1}$.

$l = 1$ peak of the potential cannot act as a barrier any more and indeed we lose the peak in the absorption cross section which was more closely related to that. Note that our results are in agreement with those in [86].

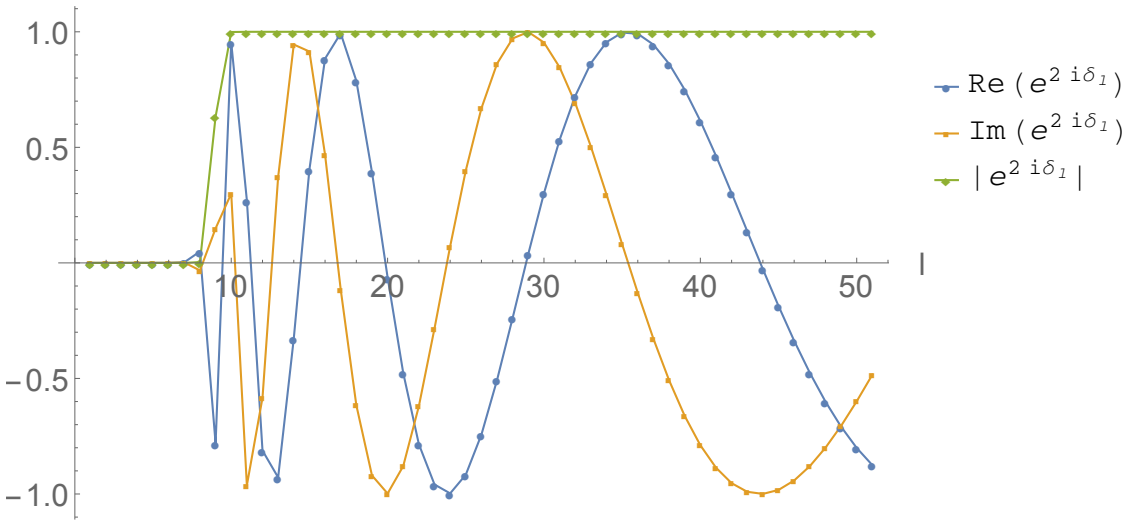

Figure 4.10: $\mathrm{Re}(e^{2i\delta_l})$, $\mathrm{Im}(e^{2i\delta_l})$ and $|e^{2i\delta_l}|$ vs l diagram for the Schwarzschild black hole. The first l's are absorbed, while for larger l, S_l admits oscillatory behaviour. Here we have chosen $w = 15$ and $\beta_\phi = 0$.

Our considerations up to now allow us to draw the following conclusion when it comes to the study of absorption cross sections for the massive scalar field. They are directly related to the study of V_{eff}. Thus, the study of the effective potential for each black hole

under consideration can provide us with relatively accurate answers as to the absorption cross section of the black hole.

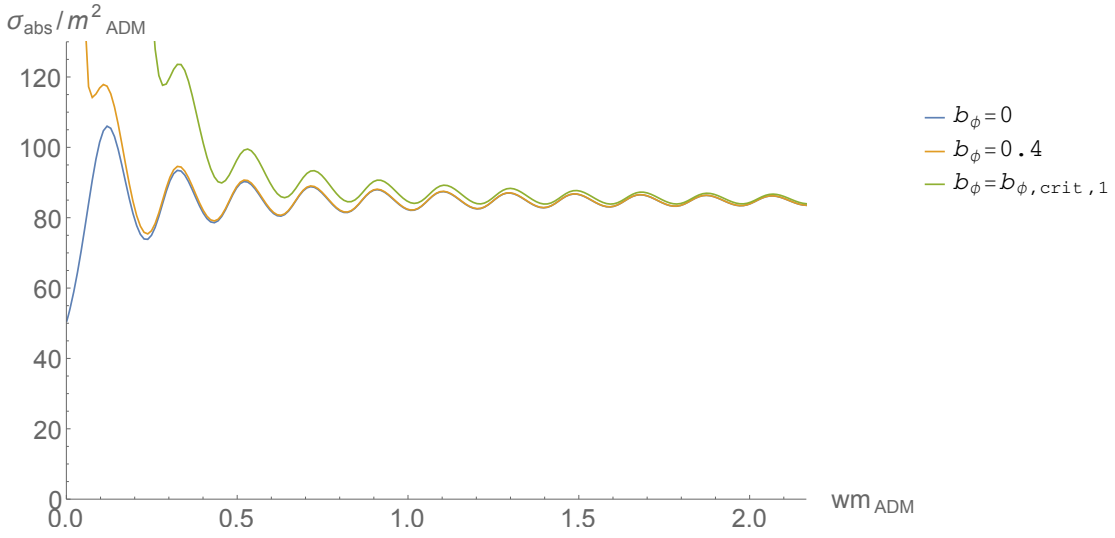

Figure 4.11: Total absorption cross sections for the Schwarzschild black hole $(\alpha, \beta, x_h) = (0, 0, 0.2166)$ for three different values of the mass of the scalar field. They are taken to be $\beta_\phi = 0$, $\beta_\phi = 0.4$ and $\beta_\phi = \beta_{\phi,crit,1} = 1.778$.

In the case of the Skyrmion black hole, the black hole lying at the centre of the configuration is smaller than the corresponding Schwarzschild black hole of the same mass. However, smaller black holes have higher peaks in the effective potential for the each l. This automatically means that the critical values for β_ϕ for each l, namely $\beta_{\phi,crit,l}$, of the Skyrmion black holes denoted as CASE I and CASE II are greater than the corresponding critical values referring to the Schwarzschild black hole. As a result, for the same value of β_ϕ, we expect that the Skyrmion black holes will still absorb less compared to the Schwarzschild one. This can indeed be seen in Figure 4.12, where our results regarding the amount of absorption and the characteristic peaks of the absorption cross section remain qualitatively the same. At the same time, the value of β_ϕ required to wipe out the first characteristic peak is smaller for the Schwarzschild black hole than the Skyrmion black holes as argued. Same goes for the other characteristic peaks as well.

Note also that the larger the black hole, the more efficient absorber it is. That is after all why we normalize the absorption cross sections with respect to the square of the mass of the configuration. In the case of the Skyrmion black holes $m_{ADM} \neq m_{BH}$, thus $\sigma/m^2_{ADM} \neq \sigma/m^2_{BH}$. Even though the extra mass lying around the Skyrmion black holes helps them absorb more with respect to a Schwarzschild black hole of the same size, this extra mass cannot absorb the scalar field by itself. That is something only that black hole itself is able to do. That is after all why the absorption cross sections do not coincide for all three black holes under consideration here. Even if the absorptions do coincide in some neighbourhood of w [5], they will not coincide globally, as for greater values of w

[5] This happens for each value of the probe field mass β_ϕ, if we look at the neighbourhood where $w \approx \beta_\phi$.

absorption will be dominated by larger values of l which are less affected by the value of β_ϕ.

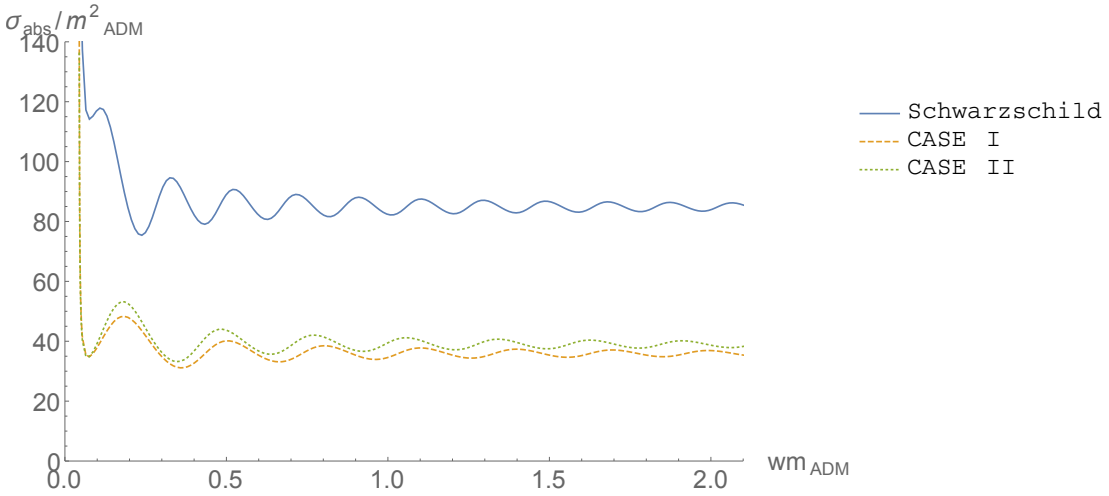

Figure 4.12: Total absorption cross section of a scalar field with mass $\beta_\phi = 0.4$ with respect to its frequency. The absorbers are a Schwarzschild $(\alpha, \beta, x_h) = (0, 0, 0.2166)$ and two Skyrmion black holes named CASE I $(\alpha, \beta, x_h) = (0.01, 0, 0.119)$ and CASE II $(\alpha, \beta, x_h) = (0.01, 0.5, 0.116)$. All have $m_{ADM} = 0.1083$.

We now move on to examine the effect of the mass of the probe field on the scattering cross sections. In Figure 4.13, we present the differential scattering cross section of a scalar field with frequency $w = 15$ for different values of its mass. We observe that as its mass is increased from zero, the peaks are starting to move towards smaller scattering angles. Then, for some value of the mass of the scalar field this motion is reversed and the peaks start moving towards their initial positions again. In the case of the Schwarzschild black hole this back and forth motion is of the order of ~ 0.1 rad.

One way to interpret this would be to think of each l mode in terms of particle trajectories. It has been shown that each l mode can be viewed as a trajectory with a specific impact parameter. In the case of the massless scalar field this is given by [70, 71]

$$b_l w \approx E_l^{1/2} = \sqrt{l(l+1)}, \tag{4.38}$$

where E_l are the angular eigenvalues as obtained from the solution of (4.1) through the separation ansatz (4.2). So, for a fixed w, the larger l is, the further away from the black hole the corresponding trajectory lies. As β_ϕ is increased, smaller l's get absorbed and so only larger l's and correspondingly large b_l's survive. But the scattering angles for those impact parameters are smaller, so the peaks of the scattering cross section move towards smaller scattering angles. From a point onwards, absorption is rather high for small l's, while β_ϕ^2 is insignificant with respect to the the $l(l+1)$ term in V_{eff} for the surviving values of l. So, the scattering peaks start moving towards those of the massless case.

Specifically we have that σ/m_{BH}^2 coincides in a small such neighbourhood for all three black holes under consideration here. Of course, keep in mind that $w > \beta_\phi$ as it can be seen e.g. through (4.9).

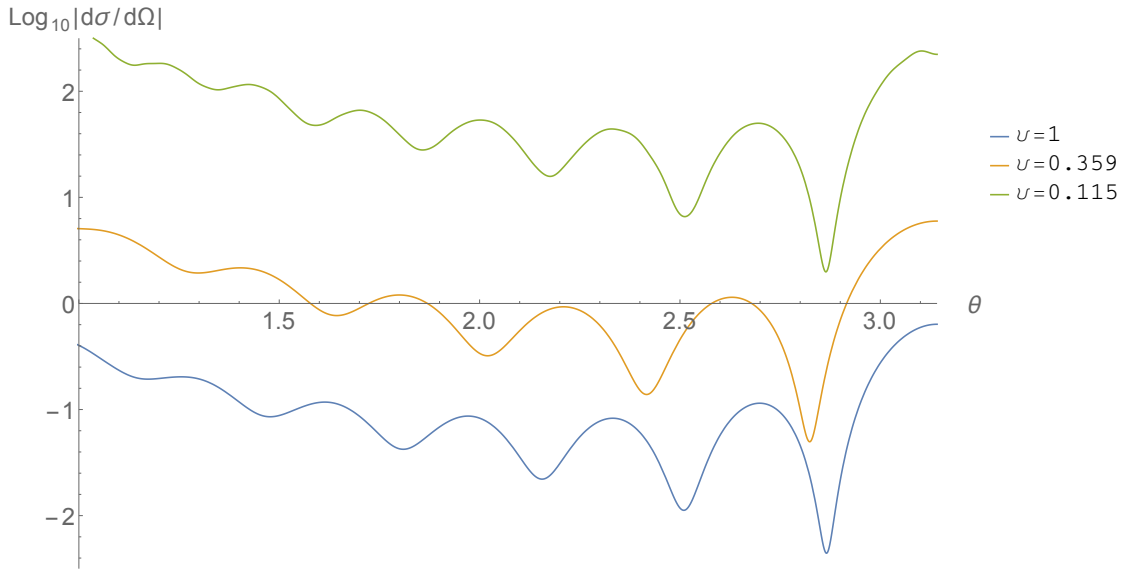

Figure 4.13: Differential scattering cross section of a scalar field with frequency $w = 15$. The scatterer is a Schwarzschild black hole $(\alpha, \beta, x_h) = (0, 0, 0.2166)$. Three different masses for the scalar are considered and they are labelled by their respective velocities.

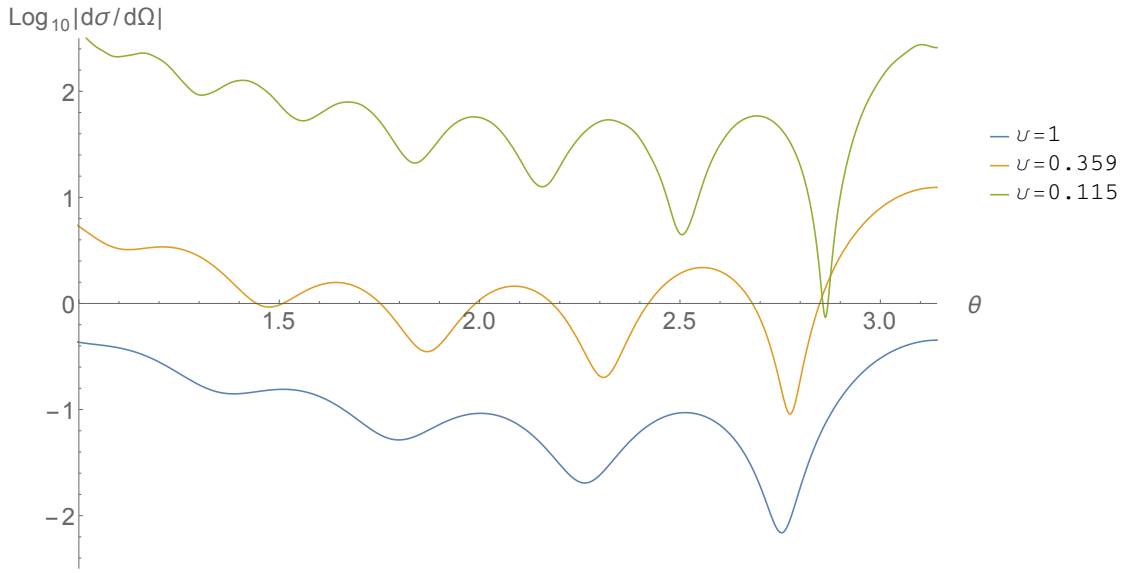

Figure 4.14: Differential scattering cross section of a scalar field with frequency $w = 15$. The scatterer is the CASE II Skyrmion black hole $(\alpha, \beta, x_h) = (0.01, 0.5, 0.116)$. Three different masses for the scalar are considered and they are labelled by their respective velocities.

The case of the Skyrmion black hole is similar. Again we notice that the peaks are initially moved towards smaller scattering angles and then the motion is inverted. The

main difference in this case is that this happens rather fast, leading to the backward motion of the peaks to be one order of magnitude less than in the case of the Schwarzschild black hole. One should keep in mind that in the case of the Skyrmion black hole there is extra mass due to the presence of hair. If we follow our line of thought for the Schwarzschild black hole, relating l modes to trajectories, we notice the following crucial difference. As the mass of the probe field is increased, then only larger l's and correspondingly b_l''s survive. However, in the case of the skyrmion black hole there extra mass lying around the black hole. Thus, those b_l's are able to "feel" that mass and are effectively scattered by a more massive body. This effect tries to shift scattering peaks towards larger scattering angles, while typically larger b_l's would lead to smaller scattering angles. Out of those two opposing effects, the first one quickly manages to overpower the latter and so scattering peaks are moved towards higher scattering angles almost immediately as β_ϕ is increased. Namely, the motion is inverted much faster. This can be seen in Figure 4.14, where the peaks for the probe field with velocity $v = 0.359$ are already located at a greater angle than where they were for the $v = 1$ probe field. This is not the case for the Schwarzschild black hole.

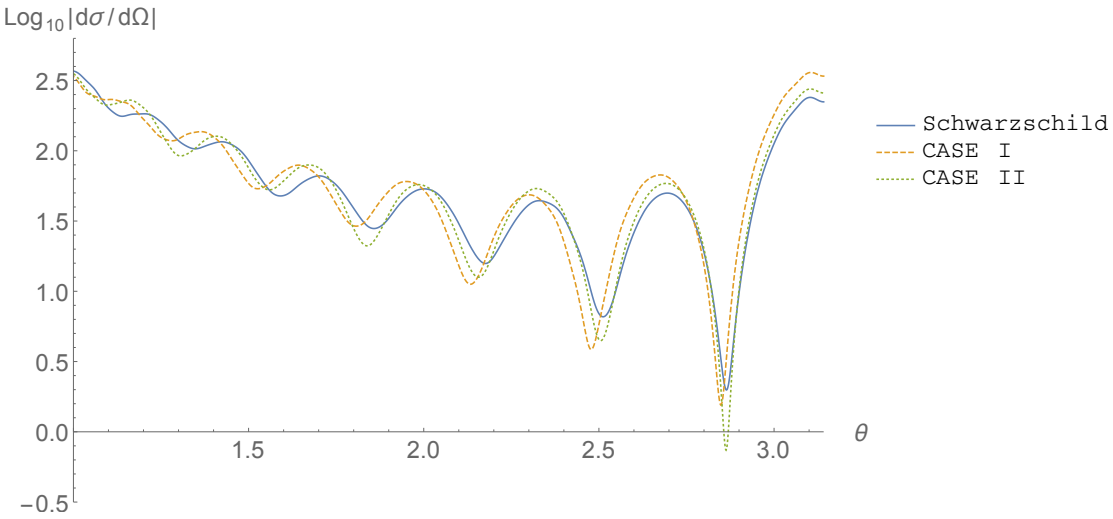

Figure 4.15: Differential scattering cross section of a massive scalar field with frequency $w = 15$ and velocity $v = 0.115$. The scatterers are a Schwarzschild $(\alpha, \beta, x_h) = (0, 0, 0.2166)$ and two Skyrmion black holes named CASE I $(\alpha, \beta, x_h) = (0.01, 0, 0.119)$ and CASE II $(\alpha, \beta, x_h) = (0.01, 0.5, 0.116)$. All have $m_{ADM} = 0.1083$.

Taking the aforementioned behaviour into account, one can make the following observation. As the peaks are affected by the mass of the scalar field, one might well get the case where some of those peaks actually end up coinciding for a Schwarzschild and a Skyrmion black hole of the same ADM mass. Namely, as the peaks move back and forth, but in a different range of values for the angle, the peaks of the Skyrmion black hole might catch up with those of the Schwarzschild black hole, provided they were relatively close to each other from the very start. So, there might exist values of the mass of the probe field for which it is not an effective mechanism of distinguishing between the two black holes.

Note that one such limit always exists, as at the large mass limit of the probe field, it is only able to resolve the far horizon geometry and thus the two black holes appear to be rather similar. Essentially, since in the *"l modes $\leftrightarrow$ trajectories"* image that we have introduced earlier only large b_l survive for large values of the mass β_ϕ, the two black holes appear the same as their spacetimes at large radial distances are identical. This is exhibited in Figure 4.15, where one clearly sees that a rather massive scalar field is unable to produce different scattering peaks at certain angles, thus unable to resolve the presence of hair.

Based on the above, a general remark would be that a scalar field is able to differentiate between Schwarzschild and Skyrmion black holes of the same mass. However, when the scalar field is taken to be massive, this ability is distorted as not all the peaks can be told apart for all values of the mass of the scalar field. One such characteristic case would be a rather massive scalar field with respect to its frequency.

Chapter 5

Conclusions

Our work has been an investigation of Skyrmion black holes, focusing on how they could be distinguished from a Schwarzschild black hole. One could also interpret it as using different probes to extract the values of the parameters of the Skyrme model through experiments performed on Skyrmion black holes. Our main results are summarized as following:

- We reproduced the main results on Skyrmion black holes. Namely, we tracked them down numerically as solutions of the Einstein-Skyrme model and we obtained solutions expected from the solution space of the model.

- Photons were used as probes in order to distinguish between Schwarzschild black holes and Skyrmion ones. Initially, the effect of hair on the photonspheres was used to trace differences in the near horizon geometry of the black holes sitting at the center of the Skyrmion. The corresponding impact parameters were found as well and were used to conclude that the effect of the black hole is significantly larger than that of the hair.

  The above motivated the study of gravitational lensing phenomena. The basics of gravitational lensing were introduced and the distance up to which such phenomena can be used to track down differences in the spacetimes produced by Schwarzschild and Skyrmion black holes of the same ADM mass was found.

- Scalar fields was the next probe we used. Results were obtained both for massless scalar fields as well as for massive scalar fields. In both cases we investigated both scattering, as well as absorption cross sections. In the massless case we found out that, both for scattering as well as absorption phenomena, the characteristic peaks of Skyrmion black holes, when compared to the same mass Schwarzschild ones, are moved towards were you would expect to find the peaks of a smaller Schwarzschild black hole. This does not depend monotonically on the mass of the central black hole, as the mass of the pion strongly affects this result. Large values of the pion mass β can counteract this behaviour and even reverse it for small differences in the mass of the central black hole. The expected behaviour at the high and low energy limits was reproduced.

  In the massive case, we found that absorption is increased and that it can be predicted qualitatively by looking directly at the effective potential. Absorption cross

sections present the same qualitative characteristics as in the massless case, the main difference from the quantitative point of view being that for frequencies close to the mass of the probe field absorption is significantly increased. As the frequency becomes even larger this behaviour becomes weaker. Regarding scattering experiments we found that the mass of the probe field is not an ally when it comes to identifying a Schwarzschild/Skyrmion black hole, as the peaks are influenced in the same way qualitatively as the mass of the probe field is increased, but from the quantitative point of view the situation is not clear. At the small velocity limit for the probe field, scattering peaks seem to align for all models of the same ADM mass and thus a rather massive scalar field, with respect to its frequency, is a clumsy and not accurate way to resolve the question of whether our spherically symmetric black hole has hair. At the same time, depending on the models under consideration there might exist other discrete values for the mass of the scalar field for which Skyrmion black holes can admit the same scattering peaks as a Schwarzschild black hole of the same ADM mass. This depends on the models.

Let us note that our results are quantitative in the Skyrmion black hole case, but qualitatively they hold for all such configurations, even in the context of other theories admitting solitonic solutions of a topological nature coupled to pure General Relativity. Evidence supporting this claim can be found in [87].

There are of course possible extensions to this work. First of all, throughout our work we have not taken into account any direct interaction term between the probes and the Skyrme hair. Such a study would be rather interesting, in order to see up to which extent our results could be altered. Furthermore, our absorption results can be extended and related to Hawking radiation. The thermodynamical properties of the black hole could then be accessed as well. In their current form, they are directly related to what goes around in the literature as the greybody factor. Finally, let us highlight that many more probes can be employed. Specifically, fields of different spin value. "Experiments" using them as their basis is a rather interesting question to pose and a potential future direction.

Appendix A

Circular orbits in Skyrme black hole spacetime

In the main text we have claimed that photon orbits around a Skyrme black hole change quantitatively, but not qualitatively. What we meant is that we expect to find a circular orbit at some radius from the Skyrmion black hole. However, the position of this orbit is not the same as it is in a Schwarzschild spacetime. Of course to this circular orbit we can then associate a constant impact parameter. The fate of incoming/outcoming photons can then be determined by comparing their impact parameter with the one corresponding to the innermost circular photon orbit. Here we investigate the claim that such a circular orbit exists even further and provide proof that it holds.

We begin by looking at Eq. (3.11), which for photons reads

$$\left(\frac{dr}{d\lambda}\right)^2 = \frac{e^2}{N^2(r)} - H(r)\frac{l^2}{r^2}. \tag{A.1}$$

If one is looking for circular orbits, then $r = r_* =$ constant and we have that the condition $dr/d\lambda = 0|_{r=r_*}$ holds. As a result, Eq. (A.1) becomes

$$\frac{e^2}{l^2} = \frac{H(r_*)N^2(r_*)}{r_*^2}. \tag{A.2}$$

One should locate the value r_* for which this equation is satisfied. Once he finds this value he can plug it back in the right hand side of Eq. (A.2) and compute the corresponding value for the impact parameter by looking at the left hand side. So, we have a problem of the form

$$f(x_0) = a, \tag{A.3}$$

namely for some function f we are looking for the value(s) of x at which it crosses the $a-$level. In the case of the Schwarzschild black hole the identification of the problem as the motion of a particle in a central potential offers a nice physical picture for the problem. We know that the point r_* at which this happens is also an extremum of the potential. So, we can differentiate Eq. (A.2) and look for the solution to the new equation.

In the general case one has to think that he is looking for circular orbits. So he needs to require that the particle not only moves on a circular orbit, but it also stays on the circular orbit. So, on top of $dr/d\lambda = 0|_{r=r_*}$, we also have $d^2r/d\lambda^2 = 0|_{r=r_*}$. Thus, we

differentiate Eq. (A.1) with respect to λ. We then obtain Eq. (3.12) for photons. Here we will avoid substituting the explicit expression for the function $H(r)$. Our equation then reads

$$\frac{d^2r}{d\lambda^2} = -\frac{e^2}{N^3(r)}\frac{dN(r)}{dr} - \frac{l^2}{2r^2}\frac{dH(r)}{dr} + H(r)\frac{l^2}{r^3}. \tag{A.4}$$

We now use Eq. (A.1) to get rid of e^2 in the first term. The new form of the equation is

$$\frac{d^2r}{d\lambda^2} = -\frac{1}{N(r)}\frac{dN(r)}{dr}\left[\left(\frac{dr}{d\lambda}\right)^2 + H(r)\frac{l^2}{r^2}\right] - \frac{l^2}{2r^2}\frac{dH(r)}{dr} + \frac{H(r)l^2}{r^3}. \tag{A.5}$$

At this point we recall that we are looking for circular orbits. So, we set $r = r_*$ and get rid of the derivative terms appearing in our expression. At the same time, the factor l^2/r^2 appears in each summand and can be omitted. We then investigate whether this equation admits solutions. The final version of the equation is

$$\frac{H(r_*)}{N(r_*)}\frac{dN(r)}{dr}\bigg|_{r=r_*} + \frac{1}{2}\frac{dH(r)}{dr}\bigg|_{r=r_*} - \frac{H(r_*)}{r_*} = 0. \tag{A.6}$$

This is a much better equation to check whether it admits solutions, as neither e nor l appear. Let us set a new function

$$G(r) = \frac{H(r)}{N(r)}\frac{dN(r)}{dr} + \frac{1}{2}\frac{dH(r)}{dr} - \frac{H(r)}{r}, \tag{A.7}$$

which is continuous in the interval $[r_h, \infty)$, where r_h is the event horizon.

Our newly set function admits the following behaviour

- At $r = r_h$ we have
$$G(r_h) = \frac{1}{2}\frac{dH(r)}{dr}\bigg|_{r=r_h} > 0, \tag{A.8}$$
as $H(r_h) = 0$ and $H(r) > 0\ \forall r > r_h$ in order for our manifold to have the right signature. So the derivative of $H(r)$ has to be positive.

- Take some r_l which lies in the asymptotic region in which $H(r) = 1 = N^2(r)$. This can always be found as we can take r_l as large as needed. Then
$$G(r_l) = -\frac{1}{r_l} < 0. \tag{A.9}$$

Combining those facts, we can conclude through Bolzano's theorem that there indeed exists at least one value $r_* \in (r_h, r_l)$ such that

$$G(r_*) = 0 \Leftrightarrow \frac{H(r_*)}{N(r_*)}\frac{dN(r)}{dr}\bigg|_{r=r_*} + \frac{1}{2}\frac{dH(r)}{dr}\bigg|_{r=r_*} - \frac{H(r_*)}{r} = 0. \tag{A.10}$$

As a result, for $r = r_*$ we have a circular orbit in any spacetime described by the metric (2.27). If there exist more than one zeros, the photonsphere is taken to be the smallest one.

If we apply the aforementioned procedure to the Schwarzschild black hole, where $H_{Sch}(r) = 1 - 2GM_{Sch}/r$ and $N^2(r) = 1$, we get

$$G_{Sch}(r) = \frac{3GM_{Sch} - r}{r^2}, \tag{A.11}$$

which admits a single finite solution at $r_{*,Sch} = 3GM_{Sch}$ as expected.

Note that r_* defines a corresponding impact parameter through Eq. (A.2). Our analysis leads us also to the following conclusion. We can define an effective potential as

$$V_{eff}(r) = \frac{H(r)N^2(r)l^2}{r^2}. \tag{A.12}$$

Then we notice that

$$\frac{dV_{eff}(r)}{dr} = \frac{2l^2N^2(r)}{r^2}G(r), \tag{A.13}$$

so, since $N^2(r) \neq 0$, the zeros of $dV_{eff}(r)/dr$ coincide with those of $G(r)$. As a result, $V_{eff}(r)$ is the extension of $\tilde{V}(r)$ from the main text in the generic case.

For a numerical study of the system, one has to track down the zeros of $G(r)$. Afterwards, determining whether they are maxima or minima can be done either by inspecting the corresponding graph or, as per usual, by examining $d^2V_{eff}(r)/dr^2$ and checking its sign at each one of the zeros.

Note that usually people (e.g. [56, 88]) define another "goto" quantity in these cases, which is

$$V_r(r) = \left(\frac{dr}{d\lambda}\right)^2 \Leftrightarrow V_r(r) = \frac{e^2}{N^2(r)} - H(r)\left(\frac{l^2}{r^2} + \kappa\right), \tag{A.14}$$

which in turn can also be studied for the same reason as $V_{eff}(r)$ since

$$\frac{dV_r(r)}{dr} = -\frac{2l^2}{r^2}G(r), \tag{A.15}$$

where we have made the substitutions $\kappa \to 0$ and $e^2/l^2 \to H(r)N^2(r)/r^2$, which hold for circular photon orbits.

Both quantities can be studied for the same reason. In general, V_r constitutes the standard approach. Nevertheless, we wished to motivate and introduce the idea of an effective potential in this case as well, as well as prove that there exist circular photon orbits.

In terms of V_r and the corresponding approach, circular orbits are characterized by $V_r(r_*) = 0$ and $dV_r/dr|_{r=r_*} = 0$. For timelike geodesics this system leads to the following expressions for the energy per unit mass and the angular momentum per

unit mass

$$e^2 = \left.\frac{2H^2(r)N^4(r)}{2H(r)N^2(r) - r\left(N^2(r)\frac{dH(r)}{dr} + 2H(r)N(r)\frac{dN(r)}{dr}\right)}\right|_{r=r_*},$$
$$l^2 = \left.\frac{r^3\left(N^2(r)\frac{dH(r)}{dr} + 2H(r)N(r)\frac{dN(r)}{dr}\right)}{2H(r)N^2(r) - r\left(N^2(r)\frac{dH(r)}{dr} + 2H(r)N(r)\frac{dN(r)}{dr}\right)}\right|_{r=r_*}, \tag{A.16}$$

where the denominator should be strictly positive as the energy should be positive.

For circular null geodesics, those conditions lead to the denominator being equal to zero, namely

$$\begin{aligned} 2H(r)N^2(r) - r\left(N^2(r)\frac{dH(r)}{dr} + 2H(r)N(r)\frac{dN(r)}{dr}\right)\Big|_{r=r_*} &= 0 \Rightarrow \\ -2r_*N^2(r_*)G(r_*) &= 0, \end{aligned} \tag{A.17}$$

which again is the condition we found earlier.

One can furthermore put a constraint on the radii at which a circular photon orbit can be found. If we substitute the expression for $H(r)$ into Eq. (A.7) we obtain

$$G(r) = \frac{-N^2(r)\left(r - 3GM(r) + Gr\frac{dM(r)}{r}\right) + rN(r)\frac{dN(r)}{dr}\left(r - 2GM(r)\right)}{r^2N^2(r)}. \tag{A.18}$$

By examining Eq. (2.38), which is one of the differential equations of the Skyrme model[1], it is evident that

$$N(r)\frac{dN(r)}{dr} \geq 0. \tag{A.19}$$

As a result, in order for $G(r)$ to be equal to zero, the first summand of the numerator should be negative. This leads to the condition

$$r - 3GM(r) + Gr\frac{dM(r)}{r} \geq 0, \tag{A.20}$$

which defines the spacetime region in which a circular orbit can exist[2].

[1] Namely this result is model specific and does not hold for any metric of the given form.

[2] Note that the mass is also given by

$$GM(r) = \frac{r_h}{2} + \int_{r_h}^{r} 4\pi r'^2\rho(r')dr', \tag{A.21}$$

in terms of the energy density ρ.

Condition (A.20) can then be written as

$$r - 3GM(r) + 4\pi r^3\rho(r) \geq 0. \tag{A.22}$$

If one studied Einstein's equations instead of $G(r)$, he would be able to infer an even stricter condition

Note that if we apply the inequality (A.20) to the case of the Schwarzschild black hole[3] it becomes

$$r - 3GM_{Sch} \geq 0, \tag{A.25}$$

as we expected.

which would read

$$r - 3GM(r) - 4\pi r^3 p(r) \geq 0, \tag{A.23}$$

where p is the pressure as defined through the energy-momentum tensor. The fact that the latter is a stricter condition follows from the weak energy condition (WEC)

$$\rho + p \leq 0. \tag{A.24}$$

[3]This can be done as (A.19) holds in the case of the Schwarzschild spacetime, where the inequality is actually saturated.

Bibliography

[1] G. Dvali and A. Gußmann, "Aharonov–Bohm protection of black hole's baryon/skyrmion hair," *Phys. Lett.*, vol. B768, pp. 274–279, 2017.

[2] G. Dvali and C. Gomez, "Black Hole's 1/N Hair," *Phys. Lett.*, vol. B719, pp. 419–423, 2013.

[3] T. H. R. Skyrme, "A Non-Linear Field Theory," *Proceedings of the Royal Society of London. Series A, Mathematical and Physical Sciences*, vol. 260, no. 1300, pp. 127–138, 1961.

[4] T. H. R. Skyrme, "A unified field theory of mesons and baryons," *Nuclear Physics*, vol. 31, pp. 556–569, Mar. 1962.

[5] I. Zahed and G. E. Brown, "The Skyrme model," *Physics Reports*, vol. 142, pp. 1–102, Sept. 1986.

[6] Y.-L. Ma and M. Harada, "Lecture notes on the Skyrme model," *arXiv:1604.04850 [hep-ph]*, Apr. 2016. arXiv: 1604.04850.

[7] N. Shiiki and N. Sawado, "Black Holes with Skyrme Hair," *ArXiv General Relativity and Quantum Cosmology e-prints*, Jan. 2005.

[8] G. H. Derrick, "Comments on nonlinear wave equations as models for elementary particles," *Journal of Mathematical Physics*, vol. 5, no. 9, pp. 1252–1254, 1964.

[9] G. S. Adkins, C. R. Nappi, and E. Witten, "Static properties of nucleons in the skyrme model," *Nuclear Physics B*, vol. 228, no. 3, pp. 552 – 566, 1983.

[10] P. Bizon and T. Chmaj, "Gravitating skyrmions," *Physics Letters B*, vol. 297, pp. 55–62, Dec. 1992.

[11] M. Heusler, N. Straumann, and Z. Zhou, "Selfgravitating solutions of the Skyrme model and their stability.," *Helvetica Physica Acta*, vol. 66, pp. 614–632, Sept. 1993.

[12] R. Bartnik and J. McKinnon, "Particlelike Solutions of the Einstein-Yang-Mills Equations," *Phys. Rev. Lett.*, vol. 61, pp. 141–144, July 1988.

[13] M. E. Ortiz, "Curved-space magnetic monopoles," *Phys. Rev. D*, vol. 45, pp. R2586–R2589, Apr. 1992.

[14] P. Breitenlohner, P. Forgács, and D. Maison, "Gravitating monopole solutions," *Nuclear Physics B*, vol. 383, pp. 357–376, Sept. 1992.

[15] P. Breitenlohner, P. Forgács, and D. Maison, "Gravitating monopole solutions II," *Nuclear Physics B*, vol. 442, pp. 126–156, May 1995.

[16] D. Maison, "Solitons of the Einstein-Yang-Mills Theory," in *Gravitation and Cosmology* (S. Dhurandhar and T. Padmanabhan, eds.), vol. 211 of *Astrophysics and Space Science Library*, p. 245, 1997.

[17] H. Luckock and I. Moss, "Black holes have skyrmion hair," *Physics Letters B*, vol. 176, pp. 341–345, Aug. 1986.

[18] S. Droz, M. Heusler, and N. Straumann, "New black hole solutions with hair," *Physics Letters B*, vol. 268, pp. 371–376, Oct. 1991.

[19] M. S. Volkov and D. V. Galtsov, "NonAbelian Einstein Yang-Mills black holes," *JETP Lett.*, vol. 50, pp. 346–350, 1989. [Pisma Zh. Eksp. Teor. Fiz.50,312(1989)].

[20] H. P. Künzle and A. K. M. Masood-ul Alam, "Spherically symmetric static SU(2) Einstein–Yang–Mills fields," *Journal of Mathematical Physics*, vol. 31, pp. 928–935, Apr. 1990.

[21] P. Bizon, "Colored black holes," *Phys. Rev. Lett.*, vol. 64, pp. 2844–2847, June 1990.

[22] K. Lee, V. P. Nair, and E. J. Weinberg, "Black holes in magnetic monopoles," *Phys. Rev. D*, vol. 45, pp. 2751–2761, Apr. 1992.

[23] P. C. Aichelburg and P. Bizon, "Magnetically charged black holes and their stability," *Phys. Rev. D*, vol. 48, pp. 607–615, July 1993.

[24] M. D. Johnson, S. S. Doeleman, and Event Horizon Telescope Collaboration, "The Event Horizon Telescope: New Developments and Results," *IAU General Assembly*, vol. 22, p. 2257792, Aug. 2015.

[25] S. Hawking and W. Israel, eds., *300 Years of Gravitation*. Cambridge University Press, 1987.

[26] M. Heusler, "No hair theorems and black holes with hair," *Helv. Phys. Acta*, vol. 69, no. 4, pp. 501–528, 1996.

[27] C. W. Misner, K. S. Thorne, and J. A. Wheeler, *Gravitation*. W.H. Freeman and Co., 1973.

[28] P. T. Chruściel, J. L. Costa, and M. Heusler, "Stationary black holes: Uniqueness and beyond," *Living Reviews in Relativity*, vol. 15, p. 7, May 2012.

[29] R. Ruffini and J. A. Wheeler, "Introducing the black hole," *Physics Today*, vol. 24, p. 30, 1971.

[30] M. Heusler, *Black hole uniqueness theorems*. Cambridge University Press, 1996.

[31] S. W. Hawking, "Black holes in general relativity," *Communications in Mathematical Physics*, vol. 25, pp. 152–166, June 1972.

[32] S. W. Hawking and G. F. R. Ellis, *The large-scale structure of space-time.* Cambridge University Press, 1973.

[33] W. Israel, "Event horizons in static vacuum space-times," *Phys. Rev.*, vol. 164, pp. 1776–1779, Dec 1967.

[34] W. Israel, "Event horizons in static electrovac space-times," *Comm. Math. Phys.*, vol. 8, no. 3, pp. 245–260, 1968.

[35] G. L. Bunting and A. K. M. Masood-ul Alam, "Nonexistence of multiple black holes in asymptotically euclidean static vacuum space-time," *General Relativity and Gravitation*, vol. 19, pp. 147–154, Feb 1987.

[36] F. J. Ernst, "New formulation of the axially symmetric gravitational field problem," *Phys. Rev.*, vol. 167, pp. 1175–1178, Mar 1968.

[37] B. Carter, "Axisymmetric black hole has only two degrees of freedom," *Phys. Rev. Lett.*, vol. 26, pp. 331–333, Feb 1971.

[38] B. Carter, "Rigidity of a Black Hole," *Nature Physical Science*, vol. 238, pp. 71–72, July 1972.

[39] D. C. Robinson, "Uniqueness of the kerr black hole," *Phys. Rev. Lett.*, vol. 34, pp. 905–906, Apr 1975.

[40] P. O. Mazur, "Proof of uniqueness of the Kerr-Newman black hole solution," *Journal of Physics A Mathematical General*, vol. 15, pp. 3173–3180, Oct. 1982.

[41] P. O. Mazur, "Black hole uniqueness from a hidden symmetry of Einstein's gravity," *General Relativity and Gravitation*, vol. 16, pp. 211–215, Mar. 1984.

[42] G. L. Bunting, *Proof of the Uniqueness Conjecture for Black Holes.* PhD thesis, Univ. of New England, Armidale, N.S.W, 1983.

[43] J. D. Bekenstein, "Transcendence of the law of baryon-number conservation in black-hole physics," *Phys. Rev. Lett.*, vol. 28, pp. 452–455, Feb 1972.

[44] J. D. Bekenstein, "Nonexistence of baryon number for static black holes," *Phys. Rev. D*, vol. 5, pp. 1239–1246, Mar 1972.

[45] J. D. Bekenstein, "Nonexistence of baryon number for black holes. ii," *Phys. Rev. D*, vol. 5, pp. 2403–2412, May 1972.

[46] C. Teitelboim, "Nonmeasurability of the baryon number of a black-hole," *Lettere al Nuovo Cimento (1971-1985)*, vol. 3, pp. 326–328, Feb 1972.

[47] C. Teitelboim, "Nonmeasurability of the lepton number of a black hole," *Lettere al Nuovo Cimento (1971-1985)*, vol. 3, pp. 397–400, Mar 1972.

[48] J. B. Hartle, "Long-range neutrino forces exerted by kerr black holes," *Phys. Rev. D*, vol. 3, pp. 2938–2940, Jun 1971.

[49] M. Heusler, S. Droz, and N. Straumann, "Linear stability of Einstein-Skyrme black holes," *Physics Letters B*, vol. 285, pp. 21–26, July 1992.

[50] G. Dvali and A. Gußmann, "Skyrmion black hole hair: Conservation of baryon number by black holes and observable manifestations," *Nuclear Physics B*, vol. 913, pp. 1001–1036, Dec. 2016.

[51] E. Witten, "Baryons in the 1n expansion," *Nuclear Physics B*, vol. 160, no. 1, pp. 57 – 115, 1979.

[52] G. S. Adkins and C. R. Nappi, "The skyrme model with pion masses," *Nuclear Physics B*, vol. 233, no. 1, pp. 109 – 115, 1984.

[53] D. Núñez, H. Quevedo, and D. Sudarsky, "Black holes have no short hair," *Phys. Rev. Lett.*, vol. 76, pp. 571–574, Jan 1996.

[54] S. Hod, "Hairy Black Holes and Null Circular Geodesics," *Phys. Rev.*, vol. D84, p. 124030, 2011.

[55] S. Weinberg, *Gravitation and Cosmology: Principles and Applications of the General Theory of Relativity*. New York, NY: Wiley, 1972.

[56] S. Chandrasekhar, *The Mathematical Theory of Black Holes*. International series of monographs on physics, Oxford, 1983.

[57] C. A. R. Herdeiro and E. Radu, "Kerr black holes with scalar hair," *Phys. Rev. Lett.*, vol. 112, p. 221101, 2014.

[58] C. A. R. Herdeiro and E. Radu, "A new spin on black hole hair," *Int. J. Mod. Phys.*, vol. D23, no. 12, p. 1442014, 2014.

[59] C. Herdeiro and E. Radu, "Construction and physical properties of Kerr black holes with scalar hair," *Class. Quant. Grav.*, vol. 32, no. 14, p. 144001, 2015.

[60] P. V. P. Cunha, C. A. R. Herdeiro, E. Radu, and H. F. Runarsson, "Shadows of Kerr black holes with scalar hair," *Phys. Rev. Lett.*, vol. 115, no. 21, p. 211102, 2015.

[61] C. A. R. Herdeiro, E. Radu, and H. Rúnarsson, "Kerr black holes with self-interacting scalar hair: hairier but not heavier," *Phys. Rev.*, vol. D92, no. 8, p. 084059, 2015.

[62] C. Herdeiro, E. Radu, and H. Runarsson, "Kerr black holes with Proca hair," *Class. Quant. Grav.*, vol. 33, no. 15, p. 154001, 2016.

[63] P. V. P. Cunha, C. A. R. Herdeiro, E. Radu, and H. F. Runarsson, "Shadows of Kerr black holes with and without scalar hair," *Int. J. Mod. Phys.*, vol. D25, no. 09, p. 1641021, 2016.

[64] P. Schneider, J. Ehlers, and E. E. Falco, *Gravitational Lenses*. 1992.

[65] J. Wambsganss, "Gravitational Lensing in Astronomy," *Living Reviews in Relativity*, vol. 1, p. 12, Nov. 1998.

[66] L. Ryder, *Introduction to General Relativity*. Cambridge University Press, 2009.

[67] N. Andersson and B. P. Jensen, "Scattering by black holes. Chapter 0.1," pp. 1607–1626, 2000.

[68] R. J. Nemiroff, "Visual distortions near a neutron star and black hole," *Am. J. Phys.*, vol. 61, p. 619, 1993.

[69] K. S. Virbhadra, D. Narasimha, and S. M. Chitre, "Role of the scalar field in gravitational lensing," *Astron. Astrophys.*, vol. 337, pp. 1–8, 1998.

[70] J. A. H. Futterman, F. A. Handler, and R. A. Matzner, *Scattering from Black Holes*. Cambridge Monographs on Mathematical Physics, Cambridge University Press, 1988.

[71] R. Newton, *Scattering Theory of Waves and Particles*. Dover Books on Physics, Dover Publications, 1982.

[72] R. A. Matzner, "Scattering of massless scalar waves by a schwarzschild "singularity"," *Journal of Mathematical Physics*, vol. 9, no. 1, pp. 163–170, 1968.

[73] P. L. Chrzanowski, R. A. Matzner, V. D. Sandberg, and M. P. Ryan, "Zero-mass plane waves in nonzero gravitational backgrounds," *Phys. Rev. D*, vol. 14, pp. 317–326, Jul 1976.

[74] D. R. Yennie, D. G. Ravenhall, and R. N. Wilson, "Phase-shift calculation of high-energy electron scattering," *Phys. Rev.*, vol. 95, pp. 500–512, Jul 1954.

[75] K. Glampedakis and N. Andersson, "Scattering of scalar waves by rotating black holes," *Class. Quant. Grav.*, vol. 18, pp. 1939–1966, 2001.

[76] J. Pryce, *Numerical Solution of Sturm-Liouville Problems*. Monographs on numerical analysis, Clarendon Press, 1993.

[77] D. Zwillinger, *Handbook of Differential Equations*. Academic Press, 1997.

[78] R. A. Isaacson, "Gravitational radiation in the limit of high frequency. i. the linear approximation and geometrical optics," *Phys. Rev.*, vol. 166, pp. 1263–1271, Feb 1968.

[79] F. A. Handler and R. A. Matzner, "Gravitational wave scattering," *Phys. Rev. D*, vol. 22, pp. 2331–2348, Nov 1980.

[80] R. A. Matzner, C. DeWitte-Morette, B. Nelson, and T.-R. Zhang, "Glory scattering by black holes," *Phys. Rev. D*, vol. 31, pp. 1869–1878, Apr 1985.

[81] N. Sánchez, "Elastic scattering of waves by a black hole," *Phys. Rev. D*, vol. 18, pp. 1798–1804, Sep 1978.

[82] P. Anninos, C. DeWitt-Morette, R. A. Matzner, P. Yioutas, and T. R. Zhang, "Orbiting cross sections: Application to black hole scattering," *Phys. Rev. D*, vol. 46, pp. 4477–4494, Nov 1992.

[83] K. W. Ford and J. A. Wheeler, "Semiclassical description of scattering," *Annals of Physics*, vol. 7, no. 3, pp. 259 – 286, 1959.

[84] T.-R. Zhang and C. DeWitt-Morette, "Wkb cross section for polarized glories of massless waves in curved space-times," *Phys. Rev. Lett.*, vol. 52, pp. 2313–2316, Jun 1984.

[85] S. Dolan, C. Doran, and A. Lasenby, "Fermion scattering by a Schwarzschild black hole," *Phys. Rev.*, vol. D74, p. 064005, 2006.

[86] E. Jung and D. K. Park, "Effect of scalar mass in the absorption and emission spectra of Schwarzschild black hole," *Class. Quant. Grav.*, vol. 21, pp. 3717–3732, 2004.

[87] A. Gußmann, "Scattering of massless scalar waves by magnetically charged black holes in Einstein–Yang–Mills–Higgs theory," *Class. Quant. Grav.*, vol. 34, no. 6, p. 065007, 2017.

[88] V. Cardoso, A. S. Miranda, E. Berti, H. Witek, and V. T. Zanchin, "Geodesic stability, lyapunov exponents, and quasinormal modes," *Phys. Rev. D*, vol. 79, p. 064016, Mar 2009.

Statement of authorship

I hereby declare that I am the sole author of this master thesis and that I have not used any sources other than those listed in the bibliography and identified as references.

Munich, May 18, 2018 .....